INTEGRATED AERODYNAMIC-STRUCTURAL-CONTROL WING DESIGN

by

Masoud Rais-Rohani

Dissertation submitted to the Faculty of the

Virginia Polytechnic Institute and State University

in partial fulfillment of the requirements for the degree of

DOCTOR OF PHILOSOPHY

in

Aerospace Engineering

APPROVED:

Dr. R. T. Haftka, Chairman

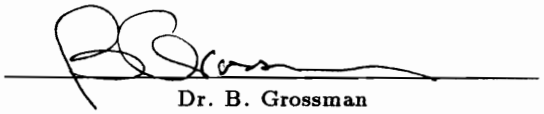

Dr. B. Grossman

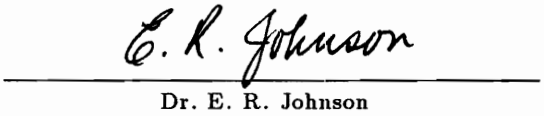

Dr. E. R. Johnson

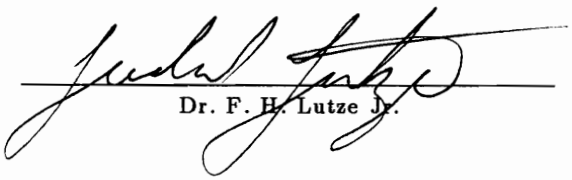

Dr. F. H. Lutze Jr.

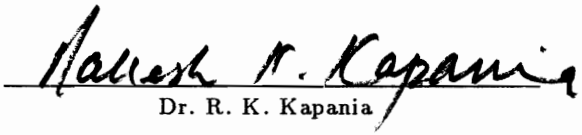

Dr. R. K. Kapania

August, 1991

Blacksburg, Virginia

INTEGRATED AERODYNAMIC-STRUCTURAL-CONTROL WING DESIGN

by

Masoud Rais-Rohani

Committee Chairman: Dr. Raphael T. Haftka

Aerospace Engineering

(ABSTRACT)

The aerodynamic-structural-control design of a simplified wing and a forward-swept composite wing are studied. In the first example, the wing is modeled as a beam with a control surface near the wing tip. The torsional stiffness is the only physical property varying along the span. The aerodynamic model is based on strip theory, and the control model is based on output feed-back control. With the structural-control interaction being the main focus, two different approaches are taken for the simplified wing design: (1) a sequential approach, (2) an integrated approach. In each approach the wing is designed for minimum weight subject to divergence and control deflection constraints. The results of this study indicated that while the integrated approach produced a better design than the sequential approach, the difference was minimal.

In the second example, a forward-swept composite wing is designed for a high subsonic transport aircraft. The structural analysis is based on finite-element method. The aerodynamic calculations are based on vortex-lattice method, and the control calculations are based on output feed-back control. The wing is designed for minimum weight subject to structural, aerodynamic/performance and control constraints. Efficient methods are used to calculate the control deflection

and efficiency sensitivities which appear as second order derivatives in the control constraint equations. To suppress the aeroelastic divergence of the forward-swept wing, and to reduce the gross weight of the design aircraft, two separate cases are studied: (1) combined application of aeroelastic tailoring and active controls, (2) aeroelastic tailoring alone. The results of this study indicated that, for this particular example, aeroelastic tailoring is sufficient for suppressing the aeroelastic divergence, and the use of active controls was not necessary.

ACKNOWLEDGEMENTS

Praise be to Allah, most gracious most merciful, who gave me enough faith, patience and perseverance to meet this challenge and succeed.

I would like to humbly appreciate the guidance of my advisor Prof. Raphael T. Haftka who taught me invaluable lessons in optimization and engineering thinking. I would like to thank Prof. Bernard Grossman for his most helpful suggestions and comments during the course of this study. Furthermore, I am grateful to my other committee members, Profs. Eric R. Johnson, Rakesh K. Kapania and Frederick H. Lutze for serving on my committee and reading my dissertation. Special thanks go to Mr. Eric R. Unger and Dr. Pi-Jen Kao for their contributions in the areas of aerodynamic and structures, and to Dr. William H. Mason for his helpful suggestions in induced drag calculations.

My greatest appreciation and admiration are due to my parents, Mohammad and Ehteram, whose unyielding determination and unselfish sacrifices made it possible for me to come to the U.S., and pursue higher eduction. I dedicate this dissertation to them. To my sister, Maryam, and brother, Mohsen, and their families who supported me greatly through out this endeavor I am utterly thankful.

To my wife, Grace, who along side me endured the setbacks patiently and rejoiced the happy moments cheerfully, I give my sincerest love and gratitude.

Furthermore, I would like to thank my friends at Virginia Tech and elsewhere, who are too many to name, for always being supportive and kind. I will never forget them.

This research was funded partially by the National Science Foundation under grant DMC-8615336 and by the NASA Langley Research Center under grant NAG-1-224.

TABLE OF CONTENTS

ABSTRACT ii

ACKNOWLEDGEMENTS iv

LIST OF TABLES viii

LIST OF FIGURES ix

1. INTRODUCTION 1

1.1 Historical Note 1

1.2 Forward-Swept Wing Analysis and Testing 4

1.3 Forward-Swept Wing Applications 9

1.4 Integrated Design and Analysis Approach 10

1.5 Previous Work at VPI&SU 12

1.6 Current Effort 13

2. SIMPLIFIED-WING PROBLEM 15

2.1 Aeroservoelastic Formulation 17

2.2 Solution of the Aeroservoelastic Equation 20

2.3 Divergence Calculation 23

2.4 Control Deflection Calculation 24

3. SIMPLIFIED-WING DESIGN OPTIMIZATION 25

3.1 Sensitivity Analysis 26

3.2 Sequential Optimization 29

3.2.1 Analytical Structural Optimization 29

3.2.2 Numerical Structural Optimization 31

3.2.3 Structural-Control Optimization 34

3.3 Integrated Optimization 36

3.3.1 Solution and Discussion of Results 37

4. FORWARD-SWEPT WING PROBLEM **43**

4.1 Design Problem 43

4.2 Design Variables 45

4.3 Design Constraints 48

4.3.1 Structural Constraints 48

4.3.2 Performance Constraints 50

4.3.3 Control Constraints 55

5. MULTIDISCIPLINARY ANALYSIS TOOLS **56**

5.1 Structural Model 56

5.2 Aerodynamic Model 60

5.3 Aerodynamic-Structural Interface 63

5.4 Control Model 65

6. AEROSERVOELASTIC ANALYSES AND SENSITIVITIES **68**

6.1 Aeroelastic Analysis at Maneuver 70

6.2 Gust-Induced Control Deflection Calculation 72

6.3 Control Efficiency Calculation 73

6.4 Divergence Calculation 74

6.5 Aeroelastic Sensitivity Analysis at Maneuver 75

6.6 Control Deflection Sensitivity Analysis 76

6.6.1 $\partial(\partial\beta/\partial\Delta\alpha_g)/\partial P$ *Calculation* 76

6.6.2 $\partial\Delta\alpha_g/\partial P$ *Calculation* 81

6.7 Control Efficiency Sensitivity Analysis 82

6.7.1 $\partial(\partial M_b/\partial\beta)/\partial P$ *Calculation for Flexible Wing* 82

6.7.2 $\partial(\partial M_b/\partial\beta)/\partial P$ *Calculation for Rigid Wing* 84

6.8 Divergence Sensitivity Analysis 84

7. APPROXIMATE OPTIMIZATION PROCEDURE AND RESULTS **87**

7.1 Solution Procedure 91

7.2 Optimization Results 97

8. CONCLUDING REMARKS **115**

REFERENCES **117**

VITA **126**

LIST OF TABLES

3.1 Simplified Wing Parameters 34

3.2 Comparison of Uniform and Structurally Optimum Wing Designs 35

3.3 Comparison of Uniform and Two Optimum Wing Designs 37

3.4 Initial and Optimum Wing Designs 40

3.5 Comparison of $\mathbf{F}$ and $T\mathbf{\Lambda}$ 40

3.6 Final Normalized Wing Weight for Various Stiffness Polynomials 40

3.7 Initial and Final Wing Designs With Two Control Gains 41

3.8 Initial and Final Wing Designs With Seven Control Gains 42

4.1 Reference Aircraft Characteristics 45

4.2 List of Design Variables 46

4.3 List of Design Constraints 49

4.4 Wing-Structure Strain and Stress Allowables 49

5.1 Finite-Element Model Break Down 57

5.2 Minimum Gage Value for Each Structural Member 58

5.3 Wing-Structure Material Properties 59

7.1 Initial and Final Wing Design Characteristics 113

7.2 Initial and Final Aerodynamic Design Variables 113

7.3 Initial and Final Performance and Control Design Variables 113

7.4 Initial and Final Structural Design Variables 114

LIST OF FIGURES

1.1 Comparison of Critical Speeds for Swept Wings 2

1.2 Bending-Torsion Coupling in Swept Wings 3

1.3 Executive Jet Wing-Skin Weight Vs Sweep Angle 4

2.1 Wing Twist Angle Vs Airspeed 16

2.2 Beam-Rod Representation of the Simplified Wing 17

2.3 Feed-Back Control System Diagram 21

3.1 Sequential Optimization Flow Chart 36

3.2 Integrated Optimization Flow Chart 39

4.1 Wing-Shape Design Variables 47

4.2 Ply Orientation Design Variables 48

4.3 SC(3)-0712(B) Airfoil Geometry 53

5.1 Finite-Element Model of the Wing 57

5.2 Close-Up View of a Single Wing-Box Cell 58

5.3 Ply Orientation in Each Panel 59

5.4 Vortex-Lattice Model 61

5.5 Load-Set Nodes 64

5.6 Control Surface and Sensor Locations 66

7.1 Design Procedure Flow Chart 92

7.2 Rigid-Wing Analysis and Sensitivity Calculations Flow Chart 93

7.3 Maneuver Aeroelastic and Sensitivity Calculations Flow Chart 95

7.4 Gust and Divergence Analyses and Sensitivity Calculations Flow Chart . 96

7.5 Control Efficiency and Sensitivity Calculations Flow Chart 97

7.6 Gross Weight Convergence History 102

7.7 Wing Weight Convergence History 102

7.8 Usable Fuel Weight Vs Cycle Number 103

7.9 Total Wing Area Vs Cycle Number 103

7.10 Wing Chord Vs Cycle Number 104

7.11 Wing-Section Span Vs Cycle Number 104

7.12 Total Wing Span Vs Cycle Number 105

7.13 Aspect Ratio Vs Cycle Number 105

7.14 Wing Twist Vs Cycle Number 106

7.15 Sweep Angle Vs Cycle Number 106

7.16 Control Gain Vs Cycle Number 107

7.17 Control Deflection Vs Cycle Number 107

7.18 Control Efficiency Vs Cycle Number 108

7.19 Dynamic Pressure Vs Cycle Number 108

7.20 Drag Vs Cycle Number 109

7.21 Range Vs Cycle Number 109

7.22 Gross Weight Vs Range 110

7.23 Initial and Final Wing Design Configurations 110

7.24 Comparison of Gross Weight Convergence History for the Case With and Without Active Control 111

7.25 Comparison of Wing Weight Convergence History for the Case With and Without Active Control 111

7.26 Final Wing Designs Comparison 112

1. INTRODUCTION

In the complicated and challenging task of aircraft design, the interactions among various disciplines such as aerodynamics, structures, and control demand a careful consideration. The aeroelastic coupling which involves the interaction of aerodynamic and structural disciplines plays a very important role in wing design in general. In some instances this coupling produces favorable effects and in some instances unfavorable effects. This particular interaction becomes very significant in the design of forward-swept-wing aircraft. The inherent aeroelastic instability associated with this configuration requires the manipulation of wing structural deformations in such a way which permits the use of a forward-swept wing in the aircraft design.

1.1 Historical Note

The first successful forward-swept wing aircraft design was the JU-287, a German bomber first flown in 1944, with a leading-edge forward sweep angle of approximately 25°.[1] The forward sweep configuration was primarily used for low speed lateral stability. Following World War II, there were numerous efforts focused on the design, wind-tunnel and prototype flight testings of aircraft with forward-swept wings; the outcome of such efforts were the Convair B-53[2] and North American F-51 in the late 1940's and early 1950's and Hansa-320 business jet in 1960's. Although these aircraft could fly faster than their predecessors, they could only reach speeds in the low subsonic range with moderate forward sweep angle, and hence did not suffer from any noticeable aeroelastic instabilities. In 1948 Diederich and Budiansky described in their classic paper[3] the rapid reduction of the divergence

speed in metallic wings with the increase in forward sweep angle. Bisplinghoff et al.[4] presented the effect of sweep on various wing aeroelastic instabilities. In Figure 1.1, they described divergence as the critical mode of instability for wings with

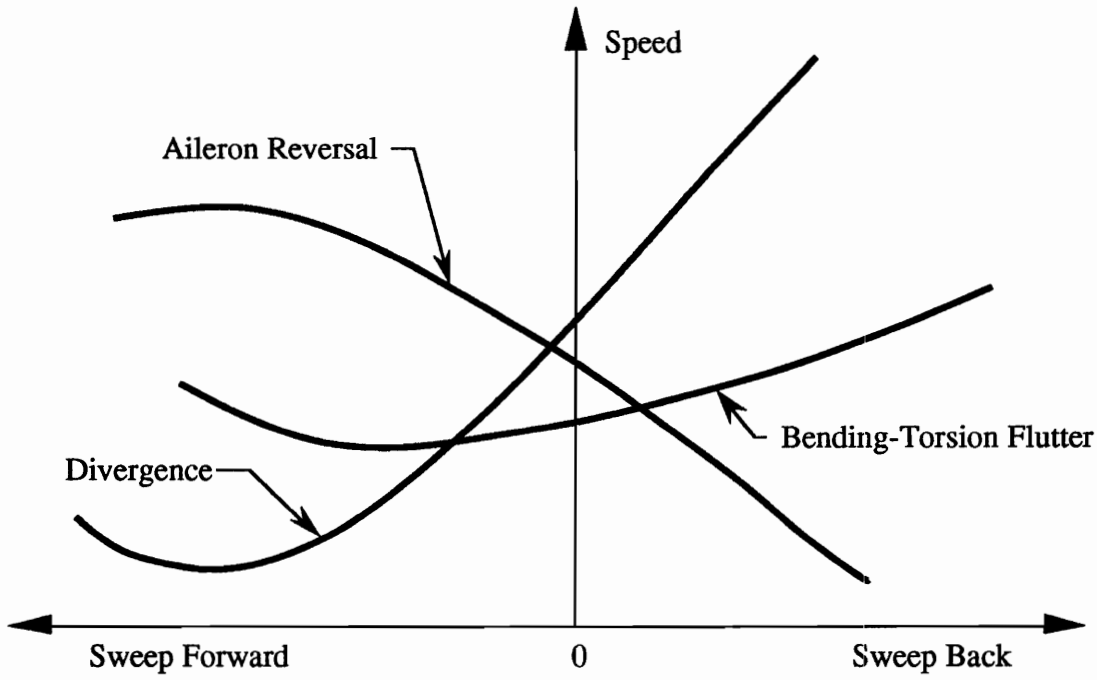

Figure 1.1 Comparison of Critical Speeds for Swept Wings (Ref. 4)

moderate to high sweep angles. The phenomenon responsible for reducing divergence speed in forward-swept wings is an adverse bending-torsion coupling. This coupling, under the influence of positive lift, causes an increase in the local angle of attack as the forward-swept wing bends upward. This phenomenon is referred to as *wash-in* , and is depicted in Figure 1.2. Also shown is a favorable coupling called *wash-out* , for aft-swept wings which eliminates the divergence instability. The findings by Diederich and Budiansky discouraged further attempts in utilizing forward sweep configuration in aircraft wing design especially since the weight penalty associated with stiffening metallic wing structure for avoiding such instability was enormous.

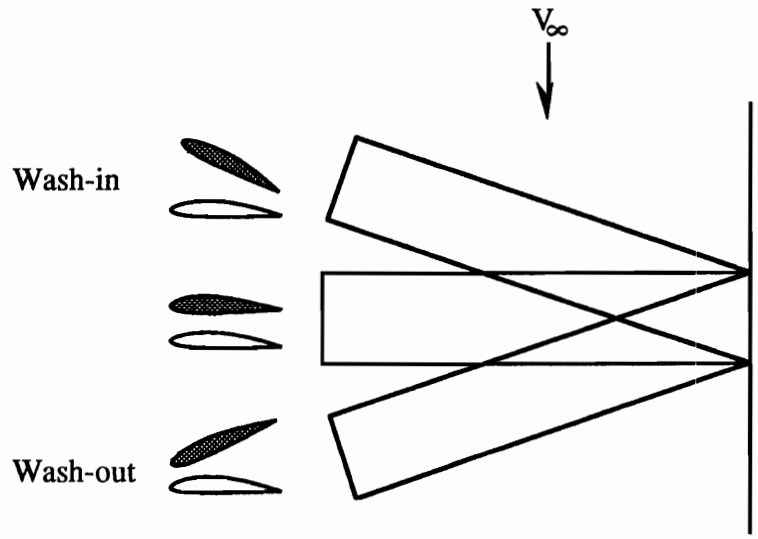

Figure 1.2 Bending-Torsion Coupling in Swept Wings

The divergence problem was a barrier that, unless overcome, would prevent the consideration of forward sweep in any future aircraft wing design; this in spite of the fact that a forward-swept wing has better overall performance characteristics than its aft-swept counterpart in subsonic and transonic flight regimes.[5] The forward-swept wing design was not considered seriously again until 1975. Then, Krone[6] first described the feasibility of forward-swept wing designs using advanced composite materials. The advantages of using advanced composites lied in the fact that they could offer much higher stiffness to density ratio than the metals (e.g., Aluminum alloys) commonly used in the aircraft structures; this meant the huge weight penalty associated with the metallic forward-swept wings could be eliminated by the proper use of composite materials as shown in Figure 1.3, for example. Also their directional stiffness properties could be used to orient the fibers in the most suitable way to prevent the wash-in problem depicted in Figure 1.2 which leads to divergence.

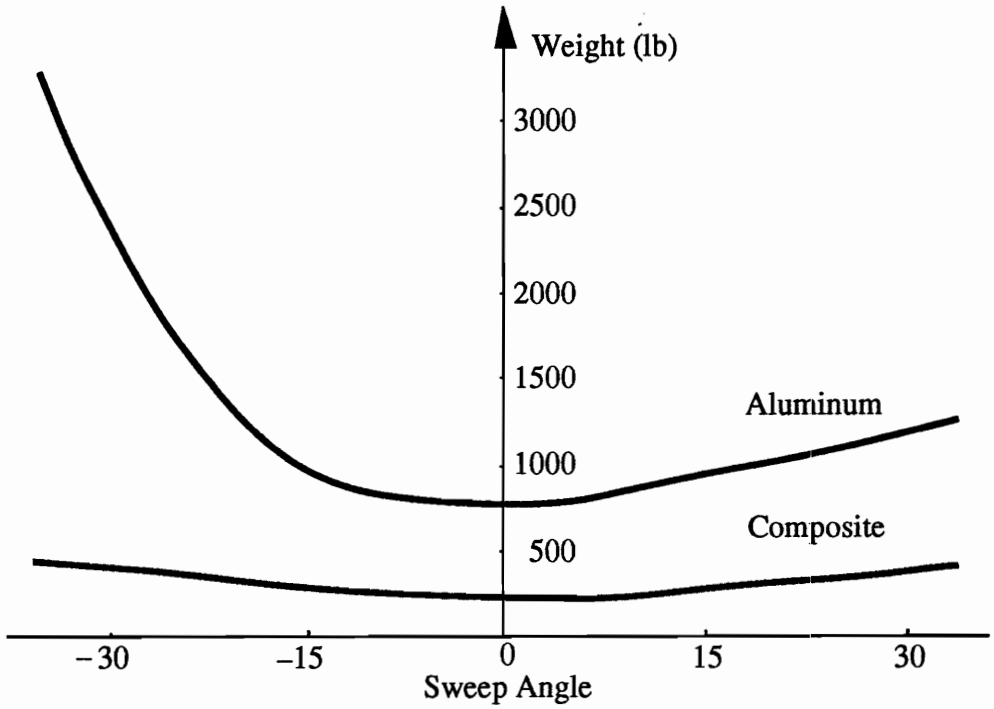

Figure 1.3 Executive Jet Wing-Skin Weight Vs Sweep Angle (Ref. 6)

The latter feature is usually referred to as aeroelastic tailoring of composites, and it was the main driving force behind the revival of forward-swept wing designs.[7,8] The latest example of this technology, the Grumman's X-29 A aircraft will be discussed in section 1.3.

1.2 Forward-Swept Wing Analysis and Testing

In 1978 Weisshaar[9] presented a simple theory for the prediction of divergence characteristics of high-aspect-ratio, laminated composite, swept wings. Later Weisshaar[10] showed that the elastic bending-torsion coupling can be manipulated through composite tailoring to preclude divergence for reasonably large forward sweep angles. The torsional coupling parameter was shown to play an important role in forward-swept wing design. The introduction of wing taper affected the formulation, but was shown to have little influence in the design of a divergence-free wing.

The structural feasibility of using aeroelastic tailoring of laminated composite material for a forward-swept wing on a high performance fighter aircraft was evaluated analytically by Triplett[11]. He also made a comparison between a forward-swept wing design obtained through an optimization process and several equivalent aft-swept wing designs. The forward-swept wing compared favorably with the aft-swept ones in terms of flutter and aircraft roll rate for aileron deflection. Triplett[12] later applied aeroelastic tailoring to fighter aircraft (F-15 type) aft-swept wing design, and showed both drag reduction and increased roll effectiveness, with no weight penalty. Aeroelastic tailoring was also shown to be an effective tool in a minimum weight tail design. Similarly, Weisshaar[13] described the effects of composites on flexible wing divergence, lift effectiveness, and spanwise center-of-pressure location based on an idealized wing model. The composite tailoring was shown to be effective in both increasing divergence (out to high aspect ratio wings) and enhancing the lateral control effectiveness.

Sherrer et al.[14] conducted a series of wind-tunnel tests to verify the composite tailoring effect on increasing the divergence speed of forward-swept wings. In most cases the analytical predictions had good correlation with the wind-tunnel results.

Ricketts and Doggett[15] performed a series of wind-tunnel studies at NASA Langley Research Center on the aeroelastic behavior of isotropic forward swept wings of various configurations. The effects of aspect ratio, sweep angle and airfoil shapes on divergence and flutter were studied. Linear aerodynamic theory was shown to accurately predict the aeroelastic behavior of thin forward-swept wings. Based on the fact that different divergence results were obtained for the forward-swept wings with different airfoil shapes, but otherwise similar characteristics, Bland[16] performed a study in which he incorporated the effect of the airfoil shape in the

potential equations used for aerodynamic calculations. He then compared the minimum divergence dynamic pressure of a supercritical wing and a conventional wing. In this comparison he observed a 17% difference between the two results, with the conventional wing having higher divergence dynamic pressure.

Landsberger and Dugundji[17] performed an analytical and experimental investigations of aeroelastic deflection, divergence, and flutter behavior of both straight and forward swept graphite/epoxy cantilevered wings.

Cole[18] conducted a wind-tunnel study to determine the divergence characteristics of a high-aspect-ratio, forward-swept wing. These characteristics were checked against analytical predictions for various sweep angles. The effects of sweep angle and wing tip shape on divergence were also studied. No composite tailoring was applied in any of the models. The wing tip shape showed significant influence on divergence, with the wing tip parallel to the flow showing favorable effects on divergence compared to the rectangular wing tip. Analytical predictions were mostly conservative.

Norton[19] conducted a complete design, fabrication and wind-tunnel testing of a composite wing model. The structural modeling technique was shown to be inadequate in predicting the divergence mode of instability; however, some useful wind-tunnel data were obtained.

The free-free analyses of forward-swept wing aircraft performed by Miller et al.[20] revealed the potential for interaction between rigid-body pitch and plunge and the flexible modes for Rockwell's proposed demonstrator aircraft. This coupling was shown to produce a dynamic instability at a speed lower than the cantilevered-wing divergence speed. This instability is referred to as body-freedom flutter, and later Weisshaar et al.[21] encountered similar phenomenon on a wind-tunnel model.

In 1983, Weisshaar and Zeiler[22] studied two separate modes of instability associated with a flexible forward-swept wing aircraft. Either the body-freedom flutter or aeroelastic divergence was shown to occur depending upon the planform geometry and mass distribution of the freely flying aircraft. Several examples were investigated. In the wing/body-tail combination example, it was shown that when the wing root is positioned far aft of the C.G., body-freedom flutter is the critical instability mode; it appears at an airspeed less than that for cantilever divergence mode. Moving the wing forward increases the flutter speed and decreases the aircraft divergence speed. Depending upon the tail size and position, either body-freedom or divergence is the mode of instability. It is concluded that the presence of a large tail or tail volume may provide the aircraft with enough aerodynamic pitch stiffness that body-freedom flutter can be precluded.

Chen and Dugundji[23] also studied the aeroelastic behavior of the forward-swept wing with rigid body pitch and plunge freedoms present. Their results reveal that forward-swept wings develop body-freedom flutter rather than divergence when rigid body modes are present, and it occurs at a lower speed than divergence; however, for cantilevered wings (when both pitch and plunge modes are restrained), divergence was shown to be the critical mode of instability.

Lottati[24] points out that composite tailoring involves a compromise on the value of the bending-torsion stiffness coupling. An attempt to reduce or eliminate the divergence of a forward-swept wing by bending-torsion stiffness coupling might greatly reduce the flutter speed of the wing.

Other studies on the aeroelastic behavior of forward-swept wings include the work by Niblett[25] in which he considers a simple aircraft model with a trim surface for divergence calculations. Librescu and coworkers [26,27] developed a simple algorithm to obtain a closed form solution for the divergence of cantilevered swept

wings. They also studied the effect of including the warping restraint, ply orientation, stacking sequence and wing geometry on the divergence results.

Shirk et al.[28] conducted a survey of the activities surrounding the application of composites for aeroelastic tailoring. While describing the advantages of aeroelastic tailoring such as maneuver drag reduction and load relief, divergence prevention, lift and control effectiveness and flutter prevention, they postulated the advantages of integrating aeroelastic tailoring and active controls in enhancing the wing design.

Besides the passive technique of composite tailoring for eliminating divergence instability, active control techniques have also been pursued for this purpose. Active control systems traditionally have been used in the design of both aft and forward-swept wings for gust-load alleviation. Using an active control system in conjunction with composite materials allows further reduction in weight of a forward-swept wing design. This is because an appropriate control deflection can alter the lift distribution on the wing so as to reduce the wash-in tendency which to a certain degree removes the stiffness requirement on the wing structure, and hence a more flexible (and lighter) structure can be used.

Griffin and Eastep[29] used simple active control laws as means of suppressing aeroelastic divergence and flutter of forward-swept wings. The selected wing models in this study were made in a manner so that the divergence and flutter speeds are relatively close together. Without the inclusion of composite tailoring, their results indicate that it is possible to avoid aeroelastic divergence by a leading-edge flap and elastic displacement sensing. Furthermore, trailing-edge flap and elastic acceleration sensing was found most suitable for flutter suppression. In both cases the increase in the speed of the controlled instability was accompanied with some reduction of speed in the other instability as pointed out by Lottati[24].

Chipman et al.[30] applied optimal control theory in an attempt to delay the cantilevered wing divergence and body-freedom flutter instabilities associated with forward-swept wing aircraft. Unlike the previous work, a trailing-edge flap was used for both instabilities. Displacement feedback was required to prevent or delay divergence. In several analyses with rigid-body modes removed, it was shown that the essential ingredient in the forward-swept wing instability is the destiffening of the wing first bending mode; furthermore, the frequency of the true dynamic instability was low enough that reasonably accurate predictions were obtained treating the problem as if it were purely static divergence.

Noll et al.[31,32] developed control laws to suppress simultaneously both cantilevered wing divergence and a higher bending-torsion flutter mode, and to suppress the rigid body pitch/wing bending instability and flutter associated with the wing free in pitch. For divergence suppression a combination of leading-edge flap and displacement sensors were used, while for flutter suppression a trailing-edge flap along with acceleration sensors were applied. The active control system proved to be effective without the use of composite tailoring.

Other techniques besides composite tailoring or active controls have also been studied. Löbert[33] used an aircraft model characterized by the combination of an aft tail and a forward swept wing with a free-floating wing tip/elevator assembly. He showed that it is possible to increase divergence speed or totally suppress divergence instability through this mechanism. This technique was also shown to be effective in gust, maneuver load and ride quality control.

1.3 Forward-Swept Wing Applications

Forward-swept wing technology has been considered for many different applications. For example, Dastin et al.[34] and Raha[35] elaborated on the application of forward-swept wing for an advanced fighter to be known as Grumman's X-29A. They discussed the improved performance, reduced acquisition costs and increased life and durability as some of the reasons for such configuration.

Schweiger et al.[36] carried out a theoretical investigation of a fighter aircraft with a forward-swept carbon fiber composite wing for superior maneuver performance at high subsonic speeds.

Roskam[37] applied the concept of forward-swept wing to a commuter airplane. The main reason for such configuration was to enhance both ride comfort and performance.

Howe[38] studied the application of forward-swept wing technology to V/STOL aircraft. He found with respect to layout advantages, such configuration to be more suitable for this application over that of an equivalent aft-swept wing.

Cook and Abla[39] did a weight comparison of divergence-free tailored metal and composite forward-swept wings for an executive aircraft. The forward-swept configuration was shown to be attractive for such application because the wing carry through is aft of the passenger cabin. This permits more efficient design of the fuselage as a pressure vessel. The results show the advantage of using advanced composites for aeroelastic tailoring and weight savings.

Redeker and Wichmann,[40] in finding forward sweep a favorable concept for a laminar flow wing, mentioned that because of three-dimensional displacement effects, the effective sweep of forward-swept wings will decrease compared to the geometrical sweep which is opposite to that for aft-swept wings. This sweep reduction, they concluded, leads to a more stable laminar boundary layer against attachment line transition and crossflow instability.

1.4 Integrated Design and Analysis Approach

An approach that has been gaining recognition in the past decade or so is the integrated approach. In this approach, the effect of changes in one discipline on the others is determined through sensitivity analysis. For example, by proper derivative calculations, the effect of changing the wing aspect ratio on the gross weight, or the effect of changing the wing sweep angle on the aeroelastic characteristics of the wing can be determined. This information can then be used in a parametric study or in an optimization process to determine the best feasible design.

Sobieski[41,42] developed an efficient method for calculating sensitivity derivatives in problems which involve interactions among various disciplines. Barthelemy and Bergen[43] discussed a method for the analytical calculations of the sensitivity derivatives of wing static aeroelastic characteristics (e.g., lift distribution, divergence dynamic pressure, etc.) with respect to wing shape parameters (e.g., wing area, aspect ratio, etc.).

Sobieski and Haftka[44] surveyed multidisciplinary optimization applications, and elaborated on the use of multilevel optimization for integrating the design process.

The benefits of integrated approach for longitudinal stability augmentation and aeroelastic stabilization was addressed by Gilbert et al.[45]. Zeiler[46] performed a combined structural-control design for aeroelastic characteristics. He studied the behavioral characteristics of an idealized three degree-of-freedom airfoil and a four degree-of-freedom aircraft. Aeroservoelastic tailoring problem was modeled as a multidisciplinary optimization problem.

Dracopoulos[47] presented a method for aeroelastic control of composite lifting surfaces. The method employed the integration and simultaneous application of aeroelastic tailoring and optimum control design. A composite wing was idealized

by a straight, rectangular, symmetric laminated plate, while the control system was represented by discrete forces acting perpendicular to the plate's surface.

Livne et al.[48–51] performed studies on the application of active control in an integrated wing design. They used a general equivalent plate analysis for the structure, Kernel function method for the unsteady aerodynamic load calculations, and linear time invariant control system.

Guruswamy[52] studied the aerodynamic-structural coupling in transonic flow. He also considered the nonlinearities associated with the control deflection and the presence of shocks in unsteady transonic flow in the aeroelastic performance of a simple rectangular wing.

Morris and Kroo[53] formulated the aircraft handling qualities and other performance characteristics as an optimization problem defined by a composite objective function which consists of various performance variables. Isogai[54] developed a direct search method for aeroelastic tailoring of composite wings with multiple constraints.

Oyibo[55] used an analytical approach to study the aeroelastic characteristics of composite forward-swept wing aircraft in terms of three generic stiffness variables and fiber orientation angle. The aeroelastic equations formulation is similar to that used by Weisshaar[13]. This method permits the study of the effect of using various composite materials in the wing structure.

Sensburg et al.[56] used the integrated approach in the design of a supersonic aircraft wing structure. The shape of the control surface and the corresponding hinge moment values were determined in a parametric study to maximize the roll rates with minimum structural weight and installed hydraulic power.

1.5 Previous Work at VPI&SU

An investigation of the techniques and advantages of integrated aircraft design was conducted by Grossman et al.[57]. The interaction of aerodynamics and structural design for a sailplane wing was studied. Analysis tools used were lifting-line theory for aerodynamics and beam theory for structures. Design variables included the wing geometry and structural sizing variables (e.g., skin thickness).

Haftka et al.[58] continued this work by incorporating efficient methods for optimization of integrated aerodynamic-structural designs. Since the major problem associated with the multidisciplinary design optimization process is the enormous computational cost, efficient methods for cross-sensitivity calculation were developed along with the use of approximate structural optimization procedures.

After the sailplane wing design, attention shifted to the integrated aerodynamic-structural design of a subsonic forward-swept transport wing which was previously studied by Shuart et al.[59] where the wing structure was optimized for a fixed aerodynamic design. Because of the complexity of the problem, more sophisticated analysis techniques had to be implemented. A vortex-lattice method was used for the aerodynamic calculations and the finite-element method was used for the structural analysis. Due to the complexity of the analyses and the size of the aerodynamic and structural influence coefficient matrices, more efficient sensitivity calculation schemes had to be followed. For that, the recently developed modular sensitivity analysis (also known as the GSE technique) by Sobieski[41,42] was used. The problem of integrated aerodynamic-structural design of the transport wing for minimum weight and subject to a required range was then formulated and solved.[60]

In the work that followed, it was noticed that the induced drag calculation based on the model implemented by Polen[61] was too low with span efficiency greater than 1. This problem was solved by calculating the induced drag from the far-field. Also

additional performance constraints were introduced in the problem to improve the design. The effort involved in this study is discussed further by Unger et al.[62].

1.6 Current Effort

The current effort described in this dissertation expands on the previous work[62,63] by incorporating the control discipline in the multidisciplinary design of the forward-swept transport wing. First in chapters 2 and 3 a simplified-wing model is used to study mainly the structural-control interaction and the effect of each on suppressing the cantilever divergence problem. In the chapters that follow, the effort is concentrated on the integrated aerodynamic-structural-control design of a high subsonic forward-swept transport wing. The only aeroelastic instability considered in the design is the wing divergence. A trailing-edge flap along with displacement feed-back are used in the control system. Both aeroelastic tailoring and active controls are used to suppress divergence. For aeroelastic tailoring, ply orientation and thickness are used as design variables.

In chapter 4, the design problem along with the corresponding variables and constraints are discussed. In this study, eight ply orientation design variables are used (instead of only one previously[63]) to allow greater tailoring flexibility in the design.

In chapter 5, the analysis used for each discipline is discussed. In chapter 6, the aeroservoelastic analyses and sensitivity formulations are discussed in detail. In chapter 7, the approximate optimization procedure used in the design is explained along with the results of the optimization for two different cases: (1) both aeroelastic tailoring and active control are used for divergence suppression, (2) only aeroelastic tailoring is used for divergence suppression. In chapter 8, concluding remarks are given along with some suggestions for future work.

2. SIMPLIFIED-WING PROBLEM

The multidisciplinary analysis and design of a wing for today's aircraft is a formidable task–especially since the theoretical model is usually very sophisticated from the standpoint of structural, aerodynamic and control modeling. However, for studying certain structural, aerodynamic and control interactions, a much simpler wing model may be used. Furthermore, the simplicity of the wing model also permits the use of less elaborate methods of analysis.

In this and the next chapter, the focus is on the analysis and design of a simple rectangular wing with emphasis on the structural-control interaction. To keep the problem simple, the wing is isolated from the rest of the aircraft; this implies that the effect of the fuselage, tail, etc. in the analysis and design of the wing is ignored. The structure and aerodynamic models used in this study are based on beam theory and rudimentary strip theory, respectively, while the control model is based on feedback control theory.

In this study the rigid-body mode is not included; hence, the aeroelastic phenomenon of interest is the cantilevered-wing divergence. At an equilibrium flight, the aerodynamic twisting moment about any axis on the wing (e.g., the elastic axis) is equal and opposite to the elastic restoring moment. While the aerodynamic moment is a function of the airspeed, the elastic moment is not. Thus, as the airspeed is increased to a value called the 'divergence speed', the aerodynamic moment exceeds the elastic restoring moment and the wing twists without bound and structural failure occurs. This phenomenon is depicted qualitatively in Figure 2.1.

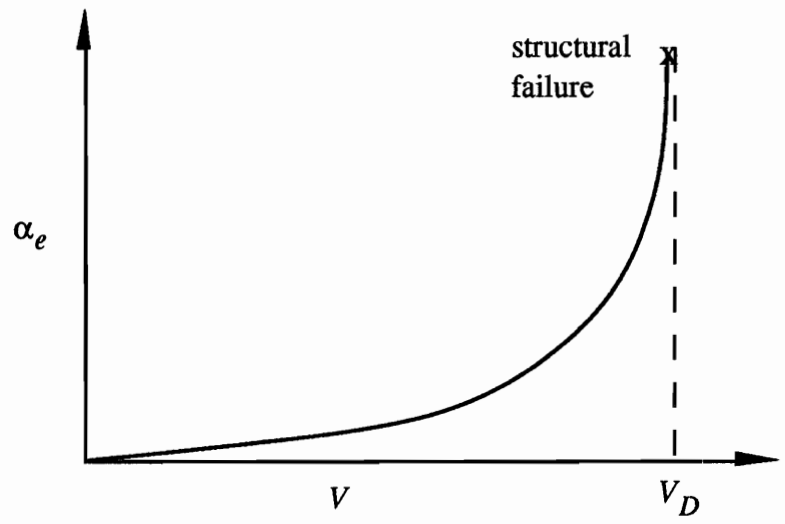

Figure 2.1 Wing Twist Angle Vs Airspeed

Generally, in unswept metallic wing designs, the divergence speed may be increased mainly by stiffening the wing structure. This, of course, means additional weight which is undesirable. In wing designs using composites, the divergence problem can also be avoided through aeroelastic tailoring with a little or no weight increase. For both types of materials it is also possible to increase the divergence speed or to maintain it at a desired level (without the structural weight penalty) by changing the lift distribution over the wing using an active control system.

The FAA regulations require the divergence speed to be at least 20% higher than the design dive speed. Here, since the comparative rather than absolute results are sought, the divergence speed of a uniform unswept wing is used instead of the dive speed whose value depends on the weight and the total drag coefficient of the whole aircraft. To meet the FAA requirement on divergence, the wing structure and the control system both must contribute. This means that part of the 20% margin must be fulfilled by the structural stiffness, while the control system is responsible for the rest. The amount of contribution from each of these disciplines will be determined during the design optimization.

The objective of this study is to find a minimum-weight wing design which meets the divergence condition without exceeding the limit placed on the control system. In this chapter the aeroservoelastic equations necessary for divergence and control surface deflection calculations are derived. These equations will then be used in the calculation of constraints in the wing design optimization discussed in the following chapter.

2.1 Aeroservoelastic Formulation

The simplified wing model as shown in Figure 2.2 is a straight and rectangular cantilevered flat plate of large aspect ratio (i.e., $l >> c$) with a control surface at trailing edge near the wing tip. A beam-rod representation is used for the wing which requires the chordwise sections to be rigid. The wing is thus one dimensional

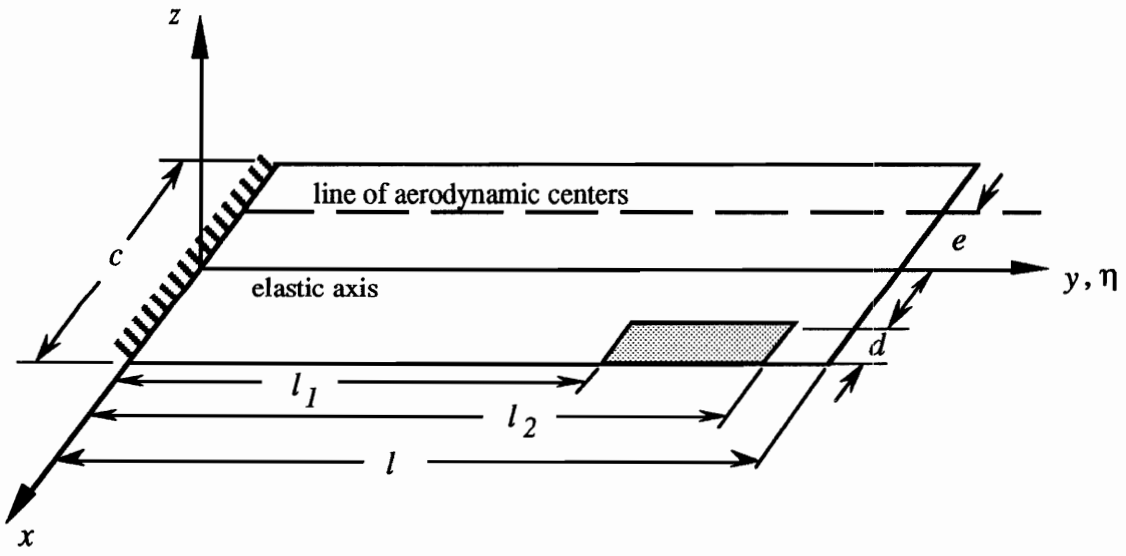

Figure 2.2 Beam-Rod Representation of the Simplified Wing

with variations only in the spanwise direction. The only wing property which is allowed to vary along the span is the torsional rigidity. Using the beam-rod representation described by Dowell et al.[64], the governing equation for the wing in

torsion is expressed as

$$\frac{d}{dy}(GJ\frac{d\alpha_e}{dy}) + M_y = 0 \ , \tag{2.1}$$

where α_e is the nose up twist about the elastic axis, M_y is the nose up aerodynamic moment about the elastic axis per unit distance in y direction, and GJ is the torsional rigidity which can vary along the span. The boundary conditions for the cantilevered wing are

$$\alpha_e = 0 \quad \text{at} \quad y = 0 \quad , \text{ and } \quad GJ\frac{d\alpha_e}{dy} = 0 \quad \text{at} \quad y = l \ . \tag{2.2}$$

The aerodynamic theory used in this analysis is the strip theory approximation which assumes that the lift and aerodynamic moment at each spanwise section of the wing depend only on the angle of attack at the same section. Thus the aerodynamic moment about the elastic axis is given by

$$M_y = M_{a.c.} + L'e \ , \tag{2.3}$$

where $M_{a.c.}$ is the aerodynamic moment about the aerodynamic center per unit distance in y direction, L' is the lift per unit distance in y direction and e is the distance between the line of aerodynamic centers and the elastic axis. Writing Eq.(2.3) in terms of non-dimensional aerodynamic coefficients, and using a linear approximation in angle of attack and control surface deflection (assuming both angles to be small) gives

$$M_y = (C_{m_{a.c.0}} + \frac{\partial C_{m_{a.c.}}}{\partial \beta} \Upsilon\beta)qc^2 + [C_{l_0} + \frac{\partial C_l}{\partial \alpha}(\alpha_0 + \alpha_e) + \frac{\partial C_l}{\partial \beta} \Upsilon\beta]qce \ , \tag{2.4}$$

where β is the downward control surface deflection in radians, $\Upsilon = 1$ for $l_1 \leq y \leq l_2$ and $\Upsilon = 0$ everywhere else, q is the free-stream dynamic pressure, c is the wing chord and α_0 is some initial angle of attack. The lift-curve slope is denoted as $\partial C_l/\partial \alpha$

while $\partial C_{m_{a.c.}}/\partial\beta$ and $\partial C_l/\partial\beta$ represent the derivatives of the aerodynamic moment and lift coefficients with respect to the control surface deflection β, respectively. The only parameter in Eq.(2.4) which varies along the span is the twist angle α_e. Since the wing is represented as a flat plate, the aerodynamic coefficients $C_{m_{a.c.0}}$ and C_{l_0} are zero. Maintaining the strip theory assumptions, Eq.(2.4) becomes

$$M_y = \frac{\partial C_l}{\partial \alpha}(\alpha_0 + \alpha_e)qce + (\frac{c}{e}\frac{\partial C_{m_{a.c.}}}{\partial \beta} + \frac{\partial C_l}{\partial \beta})\Upsilon\beta qce \ . \tag{2.5}$$

Substituting Eq.(2.5) into Eq.(2.1) and non-dimensionalizing it by the torsional stiffness at the wing root designated by $(GJ)_r$, with $y = \eta l$ yields

$$\frac{d}{d\eta}(\overline{GJ}\frac{d\alpha_e}{d\eta}) + \lambda^2 \ \alpha_e = \kappa \ , \tag{2.6}$$

where

$$\overline{GJ} \equiv \frac{GJ}{(GJ)_r} \ , \tag{2.6.a}$$

$$\lambda^2 \equiv \frac{qcel^2}{(GJ)_r}\left(\frac{\partial C_l}{\partial \alpha}\right) \ , \tag{2.6.b}$$

$$\kappa \equiv -\lambda^2(\alpha_0 + \Upsilon\gamma\beta) \ , \tag{2.6.c}$$

$$\gamma \equiv \frac{c}{e}\frac{\partial C_{m_{a.c.}}/\partial\beta}{\partial C_l/\partial\alpha} + \frac{\partial C_l/\partial\beta}{\partial C_l/\partial\alpha} \ . \tag{2.6.d}$$

Notice that λ^2 is independent of η. The aerodynamic coefficients in Eq.(2.6.d) are approximated (for a wing in an incompressible flow) in terms of E, the ratio of the control surface chord to the wing chord as described by Fung[65]

$$\frac{\partial C_l/\partial \beta}{\partial C_l/\partial \alpha} = \frac{1}{\pi}\left[cos^{-1}(1-2E) + 2\sqrt{E(1-E)}\right] , \tag{2.7}$$

$$\frac{\partial C_{m_{a.c.}}/\partial \beta}{\partial C_l/\partial \alpha} = -\frac{1}{\pi}\left[(1-E)\sqrt{E(1-E)}\right] . \tag{2.8}$$

Having all the necessary physical and geometric relations, Eq.(2.6) can be solved next.

2.2 Solution of the Aeroservoelastic Equation

Equation (2.6) is a one-dimensional, second order differential equation which describes the boundary-value problem of simplified wing

$$\frac{d}{d\eta}(\overline{GJ}\frac{d\alpha_e}{d\eta}) + \lambda^2\ \alpha_e = \kappa\ , \tag{2.6}$$

with

$$\alpha_e = 0 \quad \text{at} \quad \eta = 0 \quad , \text{ and } \quad \overline{GJ}\frac{d\alpha_e}{d\eta} = 0 \quad \text{at} \quad \eta = 1\ .$$

The boundary conditions are homogeneous as in Eq.(2.2), but are now written in non-dimensional form. An approximate solution to Eq.(2.6) can be obtained using a variational method (e.g., Ritz, Galerkin, etc.). The variational solution is obtained by first writing the differential equation (2.6) in variational (or weak) form[66] as

$$\int_0^1 \nu\left[\frac{d}{d\eta}(\overline{GJ}\frac{d\alpha_e}{d\eta}) + \lambda^2\ \alpha_e\right]d\eta = \int_0^1 \nu\ \kappa\ d\eta\ , \tag{2.9}$$

where ν is called the test function. Using the Galerkin method, the twist angle α_e is approximated by a linear combination of appropriately selected functions

$$\alpha_e(\eta) = \sum_{n=1}^{N} a_n \alpha_n(\eta)\ , \tag{2.10}$$

where $\alpha_n(\eta)$ are the *shape functions* chosen to be $sin(2n-1)\pi\eta/2$ which satisfy both the essential boundary condition (i.e., $\alpha_e(0) = 0$) and the natural boundary condition (i.e., $\overline{GJ}d\alpha_e(1)/d\eta = 0$) associated with the problem. a_n are constant coefficients and N is the number of mode shapes used in the series. Since ν must be differentiable at least once and satisfy the condition $\nu(0) = 0$, it is chosen here to be $\alpha_m(\eta)$. Substituting Eq.(2.10) into Eq.(2.9) and replacing ν by $\alpha_m(\eta)$ gives

$$\int_0^1 \frac{d}{d\eta}\left[\overline{GJ}\frac{d}{d\eta}\sum_{n=1}^{N} a_n\alpha_n(\eta)\right]\alpha_m(\eta)d\eta + \lambda^2\int_0^1 \sum_{n=1}^{N} a_n\alpha_n(\eta)\alpha_m(\eta)d\eta = \int_0^1 \kappa\alpha_m(\eta)d\eta \ . \tag{2.11}$$

Exchanging the order of summation and integration, integrating the first integral on the left hand side by parts and applying the boundary conditions gives

$$\sum_{n=1}^{N} a_n\left(\int_0^1 \overline{GJ}\frac{d\alpha_n}{d\eta}\frac{d\alpha_m}{d\eta}d\eta - \lambda^2\int_0^1 \alpha_n\alpha_m d\eta\right) = -\int_0^1 \kappa\alpha_m d\eta \ . \tag{2.12}$$

In order to proceed further with the integration in Eq.(2.12), a control law must be defined. In this study, a feed-back control system is used. Physically, the spanwise twist, α_e can be measured by placing deflection sensors at various locations along the wing. Feeding this information back into the system as illustrated in Figure 2.3, the control surface can then be deflected by a desired amount by adjusting the

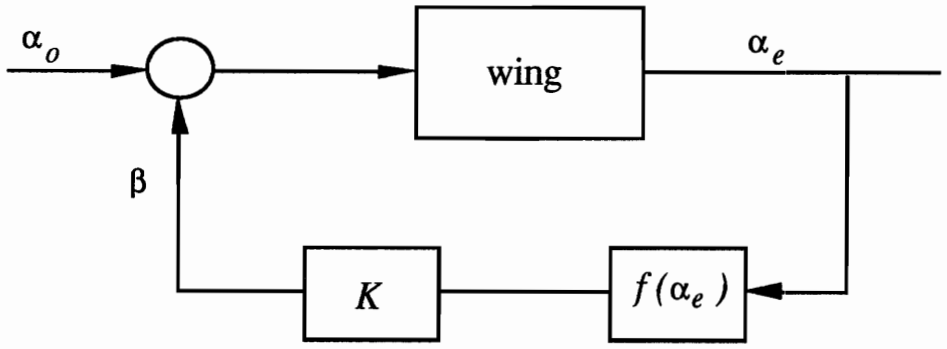

Figure 2.3 Feed-Back Control System Diagram

control gain. This deflection alters the lift distribution which through aeroelastic coupling changes the wing twist. Here, a control law is set up which relates the control surface deflection to the average value of the twist at distinct locations along the wing section where the control surface is located. The control surface is assumed to be rigid, and its deflection is given by

$$\beta = Kf(\alpha_e) \ , \tag{2.13}$$

where K is the control gain (which will be determined during the design optimization), and $f(\alpha_e)$ is the average twist which can be expressed using Eq.(2.10) as

$$f(\alpha_e) = \frac{1}{M}\sum_{j=1}^{M}\alpha_e(\eta_j) = \frac{1}{M}\left(\sum_{n=1}^{N} a_n \sum_{j=1}^{M}\alpha_n(\eta_j)\right) \ , \tag{2.14}$$

where M is the number of locations along the control-surface section of the wing where the twist is measured and η_j corresponds to the value of η at those locations. Combining Eqs.(2.14) and (2.13) and substituting the resulting equation into κ expression in Eq.(2.12) gives

$$\begin{aligned} \sum_{n=1}^{N} a_n\left(\int_0^1 \overline{GJ}\frac{d\alpha_n}{d\eta}\frac{d\alpha_m}{d\eta}d\eta \ - \ \lambda^2\int_0^1 \alpha_n\alpha_m d\eta\right) = \\ \lambda^2\alpha_0\int_0^1 \alpha_m d\eta \ + \ \lambda^2 \ \gamma \ K\sum_{n=1}^{N} a_n\left(\int_0^1 \Upsilon\bar{\alpha}_n\alpha_m d\eta\right) \end{aligned} \tag{2.15}$$

where

$$\bar{\alpha}_n \equiv \frac{1}{M}\sum_{j=1}^{M}\alpha_n(\eta_j) \ .$$

Repeating Eq.(2.15) for $m = 1, ..., N$, and writing the resulting equation in matrix notation gives

$$\Big[\mathbf{A} - \lambda^2[\mathbf{B} + \mathbf{C}]\Big]\{\boldsymbol{a}\} = \lambda^2\{\mathbf{D}\} \ , \tag{2.16}$$

where

$$A_{mn} \equiv \int_0^1 \overline{GJ} \frac{d\alpha_m}{d\eta} \frac{d\alpha_n}{d\eta} d\eta \ ,$$

$$B_{mn} \equiv \int_0^1 \alpha_m \alpha_n d\eta \ ,$$

$$C_{mn} \equiv \gamma K \int_0^1 \Upsilon \alpha_m \bar{\alpha}_n d\eta \ ,$$

$$D_m \equiv \alpha_0 \int_0^1 \alpha_m d\eta \ .$$

The vector $\boldsymbol{a}$ contains the coefficients a_1 through a_N. $\mathbf{A}$ is the structural influence coefficient matrix and $\mathbf{C}$ is the control system influence coefficient matrix. The matrices $\mathbf{A}$, $\mathbf{B}$ and $\mathbf{C}$ have the dimensions $N \times N$. Equation (2.16) may be used to solve for both divergence and lift-distribution problems.

2.3 Divergence Calculation

To determine the divergence dynamic pressure at a specified control gain setting, a non-trivial solution to the homogeneous part of Eq.(2.16)

$$\left[[\mathbf{B} + \mathbf{C}]^{-1} \mathbf{A} - \lambda^2 [\mathbf{I}] \right] \{\boldsymbol{a}\} = 0 \tag{2.17}$$

is sought. Equation (2.17) represents an eigenvalue problem with the lowest eigenvalue representing the critical λ^2 or λ_D^2, and the corresponding eigenvector is denoted as $\boldsymbol{a}_D$. The divergence dynamic pressure is then obtained from Eq.(2.6.b) as

$$q_D = \lambda_D^2 \left(\frac{(GJ)_r}{cel^2 (\partial C_l / \partial \alpha)} \right) . \tag{2.18}$$

2.4 Control Deflection Calculation

To calculate the control deflection β for a given value of control gain K, first Eq.(2.16) is solved for the coefficient vector $\boldsymbol{a}$ at a specified dynamic pressure ($q < q_D$ or $\lambda^2 < \lambda_D^2$) and α_0. Once this is done, the elastic twist at any point along the wing can be evaluated from Eq.(2.10). Then, using the coefficient vector $\boldsymbol{a}$ in conjunction with Eqs.(2.13) and (2.14), the control surface deflection β is determined.

3. SIMPLIFIED-WING DESIGN OPTIMIZATION

In this chapter the focus is on the structural-control design optimization of the simplified wing analyzed in the previous chapter. The objective of the wing design is to minimize the wing weight while satisfying the FAA divergence requirement, and limiting the control surface deflection to the linear range (i.e., $\beta < 10°$). Since the wing weight depends on the structural stiffness, it may be approximated as

$$W = \tau \int_0^1 \overline{GJ}(\eta)\, d\eta \ , \tag{3.1}$$

where $\overline{GJ}$ is the non-dimensional torsional stiffness of the wing and τ is a constant of proportionality which relates the structural weight of the wing to its non-dimensional torsional stiffness. To meet the FAA requirements, the divergence dynamic pressure must be at least 44% higher than the design dive dynamic pressure, q_{D_0}; this value is consistent with the 20% margin on the divergence speed. The properties of the optimized wing are normalized with respect to those of a uniform straight wing which has a divergence dynamic pressure of q_{D_0}. From Ref. 65

$$q_{D_0} = \lambda_{D_0}^2 \left(\frac{GJ}{cel^2(\partial C_l/\partial \alpha)} \right) \ , \tag{3.2}$$

where $\lambda_{D_0}^2 = \pi^2/4$. The optimized wing is required to be divergence free up to q_{D_0} without the control system. To achieve the 44% margin on q_D, the control system needs to be used. A limit of 10° is imposed on the control deflection at $q = q_{D_0}$ to prevent it from becoming too large, and hence avoiding nonlinear effects. However, if this deflection does not increase q_D to satisfy the 44% margin, then the structure will be stiffened gradually until the margin is met. Therefore, the margin on divergence dynamic pressure may be partly taken care of by the control system and partly by

the structural stiffness. These goals are to be achieved while minimizing the weight of the wing structure by changing the torsional stiffness GJ and the control gain.

The optimization problem is formulated as to find the control gain design variable K and torsional stiffness design variables $\overline{GJ}(0)$, $\overline{GJ}(0.5)$ and $\overline{GJ}(1)$ which

$$\begin{aligned} &\text{minimize} && W = \tau \int_0^1 \overline{GJ}(\eta) d\eta \ , \\ &\text{subject to} && g_1 = \frac{q_D}{q_{D_0}} - 1.44 \geq 0 \ , \\ & && g_2 = 1.0 - \frac{\beta}{\beta_{max}} \geq 0 \ . \end{aligned} \tag{3.3}$$

Here, the weights associated with the control sensors and actuator are assumed to be negligible compared to the structural weight and hence are ignored in the objective function formulation. The first constraint g_1, requires the divergence dynamic pressure to be at least 44% higher than q_{D_0}. The second constraint g_2, requires the control surface deflection (at $q = q_{D_0}$) to be less than or equal to β_{max} (chosen to be 10°) which is in accordance with the linear (i.e., strip) aerodynamic theory used in the analysis. The design variables chosen in this problem are the non-dimensional torsional stiffnesses at specified locations along the wing and the control gain. A lower bound of 0.1 is imposed on the stiffness design variables to prevent them from going to zero during the optimization process. To solve the optimization problem, two different approaches are taken: (1) the sequential approach, (2) the integrated approach. In sections 3.2 and 3.3 both of these approaches and the corresponding results are discussed.

3.1 Sensitivity Analysis

The objective function sensitivities are determined by differentiating the objective function with respect to the design variables as

$$\frac{\partial W}{\partial x_i} = \tau \int_0^1 \frac{\partial \overline{GJ}}{\partial x_i} d\eta \ , \qquad i = 1, ..., NDV \ , \tag{3.4}$$

where x_i represents the i^{th} design variable; in this problem, since the objective function is not a function of the control gain, its derivative with respect to the control design variable is zero. To determine the divergence sensitivities, it is more convenient to express the constraint g_1 in terms of the divergence parameter λ_D^2 such that

$$g_1 = \frac{\lambda_D^2}{\lambda_{D_0}^2} - 1.44 \geq 0 \ .$$

Then Eq.(2.17) is differentiated with respect to the design variables at $\lambda^2 = \lambda_D^2$

$$\left[\frac{\partial \mathbf{A}}{\partial x_i} - \frac{\partial \lambda_D^2}{\partial x_i}[\mathbf{B}+\mathbf{C}] - \lambda_D^2 \frac{\partial \mathbf{C}}{\partial x_i}\right]\{\boldsymbol{a}_D\} + \left[\mathbf{A} - \lambda_D^2[\mathbf{B}+\mathbf{C}]\right]\{\frac{\partial \boldsymbol{a}_D}{\partial x_i}\} = 0 \ . \qquad (3.5)$$

Since the $\mathbf{B}$ matrix is not a function of any of the design variables, its derivatives do not appear in Eq.(3.5). Multiplying Eq.(3.5) by the left eigenvector $[\boldsymbol{a}_L]^T$ defined by

$$[\boldsymbol{a}_L]^T\left[\mathbf{A} - \lambda_D^2[\mathbf{B}+\mathbf{C}]\right] = 0 \ , \qquad (3.6)$$

and simplifying the resulting equation gives

$$\frac{\partial \lambda_D^2}{\partial x_i} = \frac{\boldsymbol{a}_L^T\,(\partial \mathbf{A}/\partial x_i)\,\boldsymbol{a}_D - \lambda_D^2\,\boldsymbol{a}_L^T\,(\partial \mathbf{C}/\partial x_i)\boldsymbol{a}_D}{\boldsymbol{a}_L^T\,[\mathbf{B}+\mathbf{C}]\boldsymbol{a}_D} \ . \qquad (3.7)$$

The divergence-parameter sensitivities in Eq.(3.7) are given in terms of the derivatives of the structural and control influence coefficients where

$$\frac{\partial A_{mn}}{\partial x_i} = \int_0^1 \frac{\partial \overline{GJ}}{\partial x_i}\frac{d\alpha_m}{d\eta}\frac{d\alpha_n}{d\eta}d\eta \ , \qquad (3.7.a)$$

$$\frac{\partial C_{mn}}{\partial x_i} = \frac{\gamma}{M}\frac{\partial K}{\partial x_i}\int_0^1 \Upsilon \alpha_m \bar{\alpha}_n d\eta \ . \qquad (3.7.b)$$

The derivatives of A_{mn} are non-zero only for the structural design variables while the only non-zero derivative of C_{mn} is that with respect to the control design variable. The sensitivities of the divergence constraint are then given by

$$\frac{\partial g_1}{\partial x_i} = \frac{1}{\lambda_{D_0}^2}\frac{\partial \lambda_D^2}{\partial x_i} \ . \qquad (3.8)$$

To calculate the control surface deflection sensitivities, Eq.(2.13) is differentiated with respect to the design variables at $\lambda^2 = \lambda^2_{D_0}$

$$\frac{\partial \beta}{\partial x_i} = \frac{\partial K}{\partial x_i} f(\alpha_e) + K \frac{\partial f(\alpha_e)}{\partial x_i} \ . \tag{3.9}$$

The derivative of the gain K is equal to zero for the stiffness design variables and is equal to one for the control design variable which is the gain itself. The derivatives of $f(\alpha_e)$ however, are not so trivial to calculate. By examining Eq.(2.14), the dependence of $f(\alpha_e)$ on the torsional stiffness and the control gain can be realized through the coefficients a_n. Differentiating Eq.(2.14) with respect to the design variables gives

$$\frac{\partial f(\alpha_e)}{\partial x_i} = \frac{1}{M} \left(\sum_{n=1}^{N} \frac{\partial a_n}{\partial x_i} \sum_{j=1}^{M} \alpha_n(\eta_j) \right) \ . \tag{3.10}$$

To determine the derivatives of a_n, Eq.(2.16) must be differentiated with respect to the design variables as

$$\frac{\partial}{\partial x_i} \left(\left[\mathbf{A} - \lambda^2_{D_0} [\mathbf{B} + \mathbf{C}] \right] \{\boldsymbol{a}\} \right) = \frac{\partial}{\partial x_i} \left(\lambda^2_{D_0} \{\mathbf{D}\} \right) \ . \tag{3.11}$$

As mentioned earlier vector $\mathbf{a}$ contains the coefficients a_1 through a_N. Carrying out the differentiation and simplifying the resulting equation gives

$$\frac{\partial \boldsymbol{a}}{\partial x_i} = - \left[\mathbf{A} - \lambda^2_{D_0} [\mathbf{B} + \mathbf{C}] \right]^{-1} \left[\frac{\partial \mathbf{A}}{\partial x_i} - \lambda^2_{D_0} \frac{\partial \mathbf{C}}{\partial x_i} \right] \{\boldsymbol{a}\} \ . \tag{3.12}$$

The derivative of vector $\mathbf{D}$ does not appear in this equation since it is neither a function of the structural design variables nor of the control design variable. Equation (3.12) illustrates the dependency of vector $\boldsymbol{a}$ on the design variables through the derivatives of the structural and control influence coefficients. By substituting Eq.(3.12) into Eq.(3.10) and the resulting equation into Eq.(3.9), the sensitivities of the control surface deflection constraint are obtained as

$$\frac{\partial g_2}{\partial x_i} = - \frac{1}{\beta_{max}} \frac{\partial \beta}{\partial x_i} \ . \tag{3.13}$$

3.2 Sequential Optimization

As the name implies, in this approach the design optimization of the wing is done in a sequence. First, the wing structure alone is optimized for minimum weight by finding the optimum torsional stiffness variation along the wing. Then, through an iterative process which includes the divergence and control surface deflection calculations, the values of the control and the structural design variables which satisfy both constraints and minimize the objective function in Eq.(3.3) are determined. For the structural optimization two different approaches are taken: (1) an analytical approach; (2) a numerical approach.

3.2.1 Analytical Structural Optimization

In this approach, the homogeneous part of Eq.(2.6) is multiplied by α_e and integrated as

$$\int_0^1 \frac{d}{d\eta}\left(\overline{GJ}\frac{d\alpha_e}{d\eta}\right)\alpha_e d\eta + \lambda_D^2 \int_0^1 \alpha_e^2 d\eta = 0 \ . \tag{3.14}$$

Integrating the first integral by parts, applying the boundary conditions defined in Eq.(2.2) and specializing it for a uniform cross-section wing gives

$$\lambda_D^2 = \frac{\int_0^1 \overline{GJ}(d\alpha_e/d\eta)^2 d\eta}{\int_0^1 \alpha_e^2 d\eta} \ . \tag{3.15}$$

This is a Rayleigh's Quotient for the divergence parameter λ_D^2. To find the optimum torsional stiffness variation, instead of minimizing weight for fixed divergence speed, the weight is held fixed (to that for a uniform rectangular wing with divergence dynamic pressure q_{D_0}) and the divergence parameter is maximized. The optimization problem is formulated as to find the torsional stiffness design variables

$\overline{GJ}(0)$, $\overline{GJ}(0.5)$ and $\overline{GJ}(1)$ which

$$\begin{aligned} &\text{maximize} && f = \int_0^1 \overline{GJ}\left(\frac{d\alpha_e}{d\eta}\right)^2 d\eta \ , \\ &\text{subject to} && h_1 = \int_0^1 \alpha_e^2 d\eta = 1 \ , \\ & && h_2 = \int_0^1 \overline{GJ} d\eta = 1 \ . \end{aligned} \tag{3.16}$$

Using the Lagrange multiplier technique a Lagrangian functional f^* is formed as

$$f^* = \int_0^1 \overline{GJ}\left(\frac{d\alpha_e}{d\eta}\right)^2 d\eta \ - \ \mu_1\left(\int_0^1 \alpha_e^2 d\eta - 1\right) \ - \ \mu_2\left(\int_0^1 \overline{GJ} d\eta - 1\right) , \tag{3.17}$$

where μ_1 and μ_2 are the constant Lagrange multipliers. Taking the first variation of Eq.(3.17) and setting it equal to zero yields

$$\int_0^1 \left[2\overline{GJ}\frac{d\alpha_e}{d\eta}\delta(\frac{d\alpha_e}{d\eta}) + \delta(\overline{GJ})(\frac{d\alpha_e}{d\eta})^2 - 2\mu_1\alpha_e\delta(\alpha_e) - \mu_2\delta(\overline{GJ})\right] d\eta = 0 \ . \tag{3.18}$$

Integrating the first term by parts and applying the boundary conditions in Eq.(2.2) gives

$$\frac{d}{d\eta}\left(\overline{GJ}\frac{d\alpha_e}{d\eta}\right) + \mu_1\alpha_e = 0 \ , \tag{3.19}$$

$$\left(\frac{d\alpha_e}{d\eta}\right)^2 - \mu_2 = 0 \ . \tag{3.20}$$

Integrating Eq.(3.20) and applying the essential boundary condition at the wing root (i.e., $\alpha_e(0) = 0$) gives

$$\alpha_e = \sqrt{\mu_2}\ \eta \ . \tag{3.21}$$

This shows that the elastic twist varies linearly along the wing span. Substituting Eq.(3.21) into Eq.(3.19) and integrating the resulting expression gives

$$\overline{GJ} = -\mu_1\frac{\eta^2}{2} + C \ . \tag{3.22}$$

Using the natural boundary condition at the wing tip $\overline{GJ}d\alpha_e(1)/d\eta = 0$ and realizing that $d\alpha_e(1)/d\eta \neq 0$ (from Eq.(3.21)) gives $\overline{GJ}(1) = 0$. Hence, $C = \mu_1/2$ and $\overline{GJ}$ variation is given by

$$\overline{GJ} = \frac{\mu_1}{2}(1 - \eta^2) \ . \tag{3.23}$$

Substituting Eq.(3.23) into the constraint h_2 and integrating it gives $\mu_1 = 3$. Therefore, the optimum variation of $\overline{GJ}$ is given by

$$\overline{GJ}_{opt} = \frac{3}{2}(1 - \eta^2) \ . \tag{3.24}$$

This equation shows that $\overline{GJ}_{opt}$ varies quadratically from 1.5 at the wing root to 0. at the tip, with the latter value violating the lower bound constraint on $\overline{GJ}$. Substituting Eq.(3.21) into the constraint h_1 in Eq.(3.16) and integrating it gives $\mu_2 = 3$. Having determined $\overline{GJ}_{opt}$ and the corresponding α_e, the objective function f is obtained by substituting these parameters into Eq.(3.16). This gives

$$f_{max} = 3.0 \ , \qquad \text{or} \qquad \lambda^2_{\mathrm{D_{max}}} = 3.0 \ .$$

Comparing $\lambda^2_{D_{max}}$ to $\lambda^2_{D_0}$ $(= \pi^2/4)$, it is noticed that the structurally optimum rectangular wing has a divergence dynamic pressure q_D which is 21% higher than that for the uniform rectangular wing.

3.2.2 Numerical Structural Optimization

In this approach the wing weight is minimized while keeping the divergence parameter equal to q_{D_0}. Hence, the optimization problem is formulated as to find the torsional stiffness design variables $\overline{GJ}(0)$, $\overline{GJ}(0.5)$ and $\overline{GJ}(1)$ which

$$\begin{aligned} &\text{minimize} && W(\overline{GJ}) = \tau \int_0^1 \overline{GJ}(\eta) d\eta \ , \\ &\text{subject to} && g = \frac{\lambda^2_D}{\lambda^2_{D_0}} - 1.0 \geq 0 \ , \end{aligned} \tag{3.25}$$

with a side constraint $\overline{GJ} \geq 0.1$ which was absent in the analytical approach. Based on the previous findings, the $\overline{GJ}$ is modeled by a quadratic function with its coefficients functions of the design variables $\overline{GJ}(0)$, $\overline{GJ}(0.5)$ and $\overline{GJ}(1)$. For the twist angle, the first ten shape functions (i.e., $\sin(2n-1)\pi\eta/2,\ n = 1,...,10$) are used. Since the problem has only a single constraint, it is convenient to use the reciprocal-approximation based optimality criteria method[67] to solve it. In this method the objective function and the constraint are written in terms of the reciprocal of the design variables as

$$\begin{aligned} &\text{minimize} && W(Y)\ , \\ &\text{subject to} && g(Y) = g_0 + \sum_i \frac{\partial g}{\partial y_i} y_i \geq 0\ . \end{aligned} \tag{3.26}$$

where y_i are the reciprocal of the design variables x_i described earlier. The derivatives of g with respect to x_i are obtained from Eqs.(3.7) and (3.8) by omitting matrix $\mathbf{C}$ and its derivatives from these equations. This omission is done since the structural optimization is performed at $\beta = 0$ (or K = 0). Then, using the chain rule the derivatives of g with respect to y_i are calculated. The Lagrangian function for the problem is given as

$$\mathbf{L}(Y,\mu) = W(Y) - \mu\left(g_0 + \sum_i \frac{\partial g}{\partial y_i} y_i\right)\ , \tag{3.27}$$

where μ is the Lagrange multiplier. The Kuhn-Tucker (optimality) condition is

$$\frac{\partial W}{\partial y_i} - \mu \frac{\partial g}{\partial y_i} = 0\ . \tag{3.28}$$

Since the objective function is a linear function of the design variables, Eq.(3.28) is rewritten as

$$x_i^2 \frac{\partial W}{\partial x_i} + \mu \frac{\partial g}{\partial y_i} = 0\ . \tag{3.29}$$

Solving this equation for x_i gives

$$x_i = \left(-\frac{\mu(\partial g/\partial y_i)}{(\partial W/\partial x_i)} \right)^{\frac{1}{2}} , \qquad i = 1,2,3 . \tag{3.30}$$

The Lagrange multiplier μ is obtained from the requirement that $g(Y) = 0$ as

$$g_0 + \sum_i \frac{\partial g}{\partial y_i} \frac{1}{x_i} = 0 . \tag{3.31}$$

Substituting Eq.(3.30) into Eq.(3.31) gives

$$\mu = \left[\frac{1}{g_0} \sum_i \left(-\frac{\partial W}{\partial x_i} \frac{\partial g}{\partial y_i} \right)^{\frac{1}{2}} \right]^2 . \tag{3.32}$$

If no lower or upper bounds are imposed on the design variables, Eq.(3.30) and (3.32) can be used for solving the optimization problem. However, since a lower bound is placed on the stiffness design variables, Eqs.(3.31) and (3.32) have to be slightly modified such that

$$g_0^* + \sum_{i \in I_a} \frac{\partial g}{\partial y_i} \frac{1}{x_i} = 0 , \tag{3.33}$$

where

$$g_0^* = g_0 + \sum_{i \in I_p} \frac{\partial g}{\partial y_i} \frac{1}{x_i} . \tag{3.34}$$

The design variables which are at their lower bound are called passive and the set of these variables is denoted by I_p, and the rest are called active and their set is denoted by I_a. Modifying Eq.(3.32) for μ gives

$$\mu = \left[\frac{1}{g_0^*} \sum_{i \in I_a} \left(-\frac{\partial W}{\partial x_i} \frac{\partial g}{\partial y_i} \right)^{\frac{1}{2}} \right]^2 . \tag{3.35}$$

The initial design variables are chosen such that $I_p = 0$. This gives

$$g_0^* = g_0 = g(X_0) + \sum_i \frac{\partial g}{\partial x_i} x_{0_i} . \tag{3.36}$$

This method of solution is an iterative process, and it begins by calculating the derivatives of the divergence constraint and the objective function with respect to the design variables. Then, the Lagrange multiplier μ is calculated from Eq.(3.35) and the updated design variables from Eq.(3.30). The convergence is reached when the change in μ in two consecutive iterations is less than a satisfactory tolerance. In this problem the tolerance was set to 1×10^{-6}. The results obtained in this study are based on a simplified wing with parameters given below in Table 3.1.

Table 3.1 Simplified Wing Parameters

Geometric		Physical	
e/c	0.15	α_0	3.65°
E	0.25	C_L	0.4
l_1	0.70	$\partial C_l/\partial\alpha$	2π
l_2	1.00		

The iterative process converged in 9 iterations, and the same results were obtained from different starting points. The results of the numerical and analytical structural optimization are summarized in Table 3.2. The results of the numerical optimization indicate a weight saving of approximately 17.3% over the uniform wing while satisfying the constraint $\lambda_D^2 = \lambda_{D_0}^2$. The results of the analytical optimization show a divergence dynamic pressure increase of approximately 21% over the

Table 3.2 Comparison of Uniform and Structurally Optimum Wing Designs

Parameter	Uniform	Numerical Optimum	Analytical Optimum	Analytical* Optimum
$\overline{GJ}_{root}$	1.00000	1.29154	1.50000	1.24020
$\overline{GJ}_{mid.}$	1.00000	0.89281	1.12500	0.93015
$\overline{GJ}_{tip}$	1.00000	0.10000	0.00000	0.00000
q_D/q_{D_0}	1.00000	1.00000	1.21585	1.00527
W/τ	1.00000	0.82680	1.00000	0.82680
* Scaled to the same W/τ as in Numerical Optimum				

uniform wing for the same weight. The analytical results which are scaled to the same weight ratio as in the numerical optimum have a slightly higher divergence dynamic pressure ratio because the stiffness is allowed to go to zero at the tip. Hence, through structural optimization it is possible to either reduce the wing weight (holding $q_D = q_{D_0}$) or increase the divergence dynamic pressure (holding $W = W_0$) by a considerable amount.

3.2.3 Structural-Control Optimization

Previously, in the numerical optimization procedure the wing structure alone was optimized while holding the divergence dynamic pressure equal to q_{D_0}. Now, by including the control system the divergence dynamic pressure is to be increased to 1.44 q_{D_0}. Using the torsional stiffness variation $\overline{GJ}_{opt}$ determined earlier and selecting a positive value for the control gain K, the divergence dynamic pressure is determined by solving Eq.(2.17). Following this, the control surface deflection is determined by solving Eq.(2.13) (at $q = q_{D_0}$) according to the procedure discussed in section 2.4. Having found q_D and β, the constraints in Eq.(3.3) are calculated. If both constraints are active (i.e., $g_1 = 0$ and $g_2 = 0$), the optimum design is found. If on the other hand either one of the constraints is violated or is far from being active the search for the optimum design must continue. In a situation where β has reached its maximum value but the divergence margin has not been reached, the structure is stiffened such that $\overline{GJ} = \epsilon\ \overline{GJ}_{opt}$ where $\epsilon > 1.0$. The value of ϵ was determined manually in the process. The entire procedure is given in a flow chart shown in Figure 3.1. The results of the structural-control

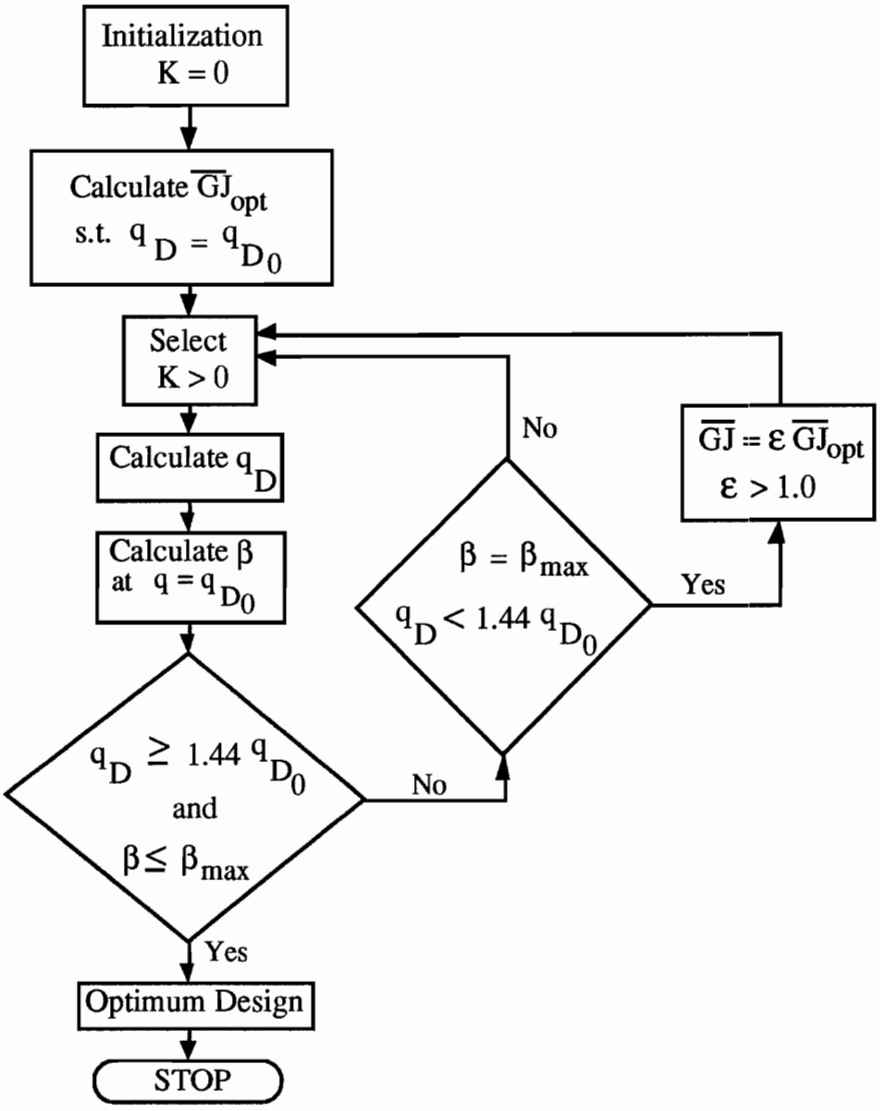

Figure 3.1 Sequential Optimization Flow Chart

optimization are given in Table 3.3 along with the results of the structural optimization for comparison. The structural optimization results indicate that it is possible to achieve the 44% margin on the divergence dynamic pressure and save approximately 17.3% on the weight. The combined optimization results show an additional weight savings of approximately 4.5% over the structurally optimum wing. The results obtained here indicate that most of the divergence alleviation is provided by the wing stiffness, while the control system contributes a marginal amount.

Table 3.3 Comparison of Uniform and Two Optimum Wing Designs

Parameter	Uniform	Structural Optimum	Structural-Control Optimum*
$\overline{GJ}_{root}$	1.44000	1.83702	1.77199
$\overline{GJ}_{mid.}$	1.44000	1.29765	1.22494
$\overline{GJ}_{tip}$	1.44000	0.10000	0.13720
K	0.00000	0.00000	0.91850
β	0.00000	0.00000	9.99055
q_D/q_{D_0}	1.44000	1.44000	1.43999
W/τ	1.44000	1.18739	1.13437
* $\epsilon = 1.372$			

3.3 Integrated Optimization

Unlike in the sequential approach where the wing structure was optimized without any influence from the control system, here the effect of control system on the aeroelastic characteristics and the effect of elastic behavior of the structure on the control deflection are felt through the cross-sensitivities evaluated from Eqs.(3.7) and (3.9). This produces a direct interaction (or coupling) between the structure and the control system which was absent in the sequential optimization. Hence, it is anticipated that this approach will yield better results than in the previous case. The problem formulated in Eq.(3.3) is solved directly using the general-purpose optimization package NEWSUMT-A[68] which is based on the extended interior penalty function method.[67] This method does not require the starting design to lie in the feasible domain, and it tolerates the occasional crossing of the design into the infeasible domain during the course of optimization.

3.3.1 Solution and Discussion of Results

The solution process begins with a selection of a set of structural and control design variables which define the initial design. Then the sensitivity derivatives of the objective function and the constraints are evaluated using the analytical sensitivity equations derived in section 3.1. This information is then supplied into the NEWSUMT-A along with the equations for the objective function and the constraints. The optimizer then uses the derivative information, and performs a series of one-dimensional searches starting from the initial design towards a local minimum point in the design space. When this process is completed, the new values for the objective function, constraints and the design variable vector are obtained.

If the constraints are active at the end of the optimization run, the Kuhn-Tucker conditions are then used to check for optimality. Similarly to Eq.(3.28), the Kuhn-Tucker conditions are given as

$$\mathbf{F} - T\mathbf{\Lambda} = 0 \ , \tag{3.37}$$

where $\mathbf{F}$ is a vector containing the derivatives of the objective function W with respect to the design variables, and T is a matrix containing the derivatives of the constraints g_1 and g_2 and the side constraint on $\overline{GJ}$ with respect to the design variables such that $t_{ij} = \partial g_j / \partial x_i$. $\mathbf{\Lambda}$ is the vector of Lagrange multipliers. Following the procedure discussed by Haftka and Kamat[67], the Lagrange multipliers in Eq.(3.37) are determined as

$$\mathbf{\Lambda} = (T^T T)^{-1} T^T \mathbf{F} \ . \tag{3.38}$$

Here, the optimality is checked by comparing the values of $\mathbf{F}$ and $T\mathbf{\Lambda}$ for closeness rather than for satisfying Eq.(3.37) exactly. If the difference between the corresponding elements in the two vectors is less than approximately 1%, the optimality

conditions are considered met. If these conditions are not satisfied, then the updated set of design variables are used as initial conditions for the next iteration. The flow chart for the integrated optimization scheme is shown in Figure 3.2.

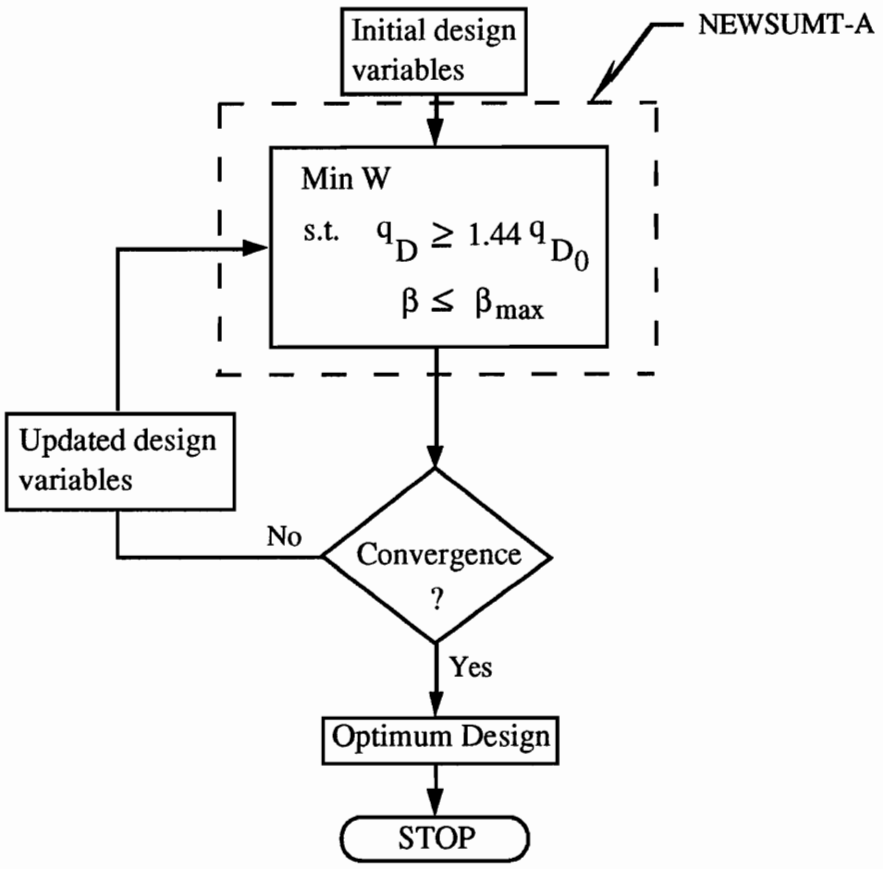

Figure 3.2 Integrated Optimization Flow Chart

The results obtained after 3 (optimization) iterations along with the initial design are given in Table 3.4. Table 3.5 gives the elements of vectors $\mathbf{F}$ and $T\mathbf{\Lambda}$ at the end of the third iteration. The final wing weight given in Table 3.4 is better than the one found in the sequential approach by an insignificant amount of 0.25%. This was unexpected. Because of the fact that the structure and control disciplines were integrated in the design process, it was expected that a much better design will be produced. This lack of significant reduction in the wing weight prompted further effort in finding ways to improve the integrated results by giving the optimizer more

Table 3.4 Initial and Optimum Wing Designs

Parameter	Initial	Final
$\overline{GJ}_{root}$	1.00000	1.78989
$\overline{GJ}_{mid.}$	1.00000	1.22539
$\overline{GJ}_{tip}$	1.00000	0.10003
K	0.10000	0.91794
β	0.00000	9.99967
q_D/q_{D_0}	1.00000	1.44001
W/τ	1.00000	1.13145

Table 3.5 Comparison of $\mathbf{F}$ and $T\mathbf{\Lambda}$

Design variables	$\mathbf{F}$	$T\mathbf{\Lambda}$
$\overline{GJ}_{root}$	0.167500	0.167761
$\overline{GJ}_{mid.}$	0.665000	0.664934
$\overline{GJ}_{tip}$	0.167500	0.167500
K	0.000000	0.000006

flexibility in finding the optimum design. The first attempt was to increase the number of structural design variables. this meant using a higher degree polynomial for the torsional stiffness variation. Table 3.6 gives the results obtained in this attempt.

Table 3.6 Final Normalized Wing Weight for Various Stiffness Polynomials

Deg. of Polynomial	W/τ
2	1.13145
3	1.13021
4	1.12963

The results in Table 3.6 indicate that even though some improvement in the design was possible by increasing the degree of the stiffness polynomial, it was not a very significant amount, only 0.4%. The next attempt was focused on increasing the number of gains and changing the control law such that

$$\beta = K_1\alpha_e(l_1) + K_2\alpha_e(l_2), \tag{3.39}$$

where K_1 and K_2 are the gains and $\alpha_e(l_1)$ and $\alpha_e(l_2)$ are respectively the wing twist angle at inboard and outboard-control edge locations where the outboard edge coincides with the wing tip. The change in the control law required a slight modification of the control influence coefficient matrix **C** such that

$$C_{mn} \equiv \gamma \int_0^1 \Upsilon \; \alpha_m \Big(K_1 \alpha_e(l_1) + K_2 \alpha_e(l_2) \Big) d\eta. \tag{3.40}$$

This change, of course, affects other equations following Eq.(3.7); but because of the similarity in the derivations, the details are not discussed here. Table 3.7 gives a summary of the results obtained in this effort. The results obtained were even

Table 3.7 Initial and Final Wing Designs With Two Gains

Parameter	Initial	Final
$\overline{GJ}_{root}$	1.00000	1.79064
$\overline{GJ}_{mid.}$	1.00000	1.22526
$\overline{GJ}_{tip}$	1.00000	0.10027
K_1	0.10000	0.44069
K_2	0.10000	0.48676
β	0.00000	9.99737
q_D/q_{D_0}	1.00000	1.44007
W/τ	1.00000	1.13152

slightly poorer than those given in Table 3.4; nevertheless, the effort continued by increasing the number of gains to seven, and instead of just measuring the wing twist at the edges of the control-section of the wing (i.e., l_1 and l_2), the twist was measured also at various other locations along the wing. The control law and other equations were modified to accommodate for this change. The results given in Table 3.8 indicate almost no improvement over the previous attempts. The results summarized in Tables 3.7 and 3.8 indicate that the number of gains and the location of the sensors have almost no effect on the wing weight. It appears as though the design is stiffness driven as indicated by the results given in Table 3.6 (and those

obtained previously in the sequential optimization), and the variations in the control system do not improve the results of the integrated optimization over the sequential one. Other attempts were also made along the line of increasing the degree of the torsional stiffness polynomial to even higher value than four, but no significant improvement was noticed in the wing weight. The difference in the results given in Table 3.3 and Table 3.6 is approximately 0.4%.

Table 3.8 Initial and Final Wing Designs With Seven Gains

Parameter	Initial	Final
$\overline{GJ}_{root}$	1.00000	1.78904
$\overline{GJ}_{mid.}$	1.00000	1.22563
$\overline{GJ}_{tip}$	1.00000	0.10040
K_1	0.10000	0.08706
K_2	0.10000	0.09214
K_3	0.10000	0.13978
K_4	0.10000	0.14282
K_5	0.10000	0.14558
K_6	0.10000	0.14759
K_7	0.10000	0.14833
β	0.00000	9.99611
q_D/q_{D_0}	1.00000	1.44015
W/τ	1.00000	1.13152

The reasons for the fact that the integrated optimization did not produce a wing which is significantly lighter than that obtained by the sequential approach may very well lie in the simplicity of the wing model. That is, the effect of the integration of various disciplines in the design process can be more profound when a more sophisticated analysis and modeling schemes are used in the wing design.

Nevertheless, the results obtained in this study showed that through structural-control optimization a wing design can be obtained which is approximately 22% lighter than the corresponding uniform wing with the same aeroelastic characteristics.

4. FORWARD-SWEPT WING PROBLEM

4.1 Design Problem

The Integrated aerodynamic-structural-control design of a forward-swept composite wing for a high-subsonic civil transport aircraft is considered here. While the focus of this study is on the wing design, the effect of the rest of the aircraft must be included as well. The aircraft in this design study is chosen to have the same characteristics as the transonic transport design obtained in a recent study at NASA Langley Research Center.[69] The pertinent characteristics of this, reference aircraft, is given in Table 4.1. However, the cruise Mach number is chosen here to be 0.68 which allows the use of a less costly subsonic aerodynamic analysis code. The objective of the wing design is to reduce the aircraft weight while maintaining the same total range and payload capacity as the reference aircraft.

The objective function is the aircraft gross weight given as

$$W = W_s + W_{uf} + W_p \ , \tag{4.1}$$

where W_s is the aircraft standard empty weight, W_{uf} is the usable fuel weight and W_p is the payload weight. The payload weight is chosen to be the same as that for the reference aircraft which includes the weight of 150 passengers, the flight crew and all the luggage. The standard empty weight of the aircraft is calculated from the standard empty weight of the reference aircraft W_{rs} by assuming that structural weight savings in the wing are amplified by a factor η due to corresponding savings in non-structural weight and in the tail and fuselage. That is

$$W_s = W_{rs} - \eta(W_{rw} - W_w) \ , \tag{4.2}$$

where W_{rw} and W_w are the structural weight of the wings of the reference and design aircraft, respectively. Here, η is chosen to be 2.8. For the reference aircraft the amount of fuel burned during take-off, landing and taxying W_{rfl}, climb to cruise altitude W_{rfc}, and descent W_{rfd} are known. Assuming that these portions of the usable fuel are proportional to the gross weight of the aircraft, their corresponding counterparts for the design aircraft are given by

$$\begin{aligned} W_{fl} &= W_{rfl}\left(\frac{W}{W_r}\right) , \\ W_{fc} &= W_{rfc}\left(\frac{W}{W_r}\right) , \\ W_{fd} &= W_{rfd}\left(\frac{W}{W_r}\right) , \end{aligned} \tag{4.3}$$

where W_r is the gross weight of the reference aircraft. Assuming that 60% of W_{fl} is used during initial taxying and take-off and 40% is used during landing and final taxying, the weight of aircraft at the beginning of the cruise W_i and at the end of the cruise W_f is determined as

$$\begin{aligned} W_i &= W - 0.6W_{fl} - W_{fc} , \\ W_f &= W - W_{uf} + W_{fd} + 0.4W_{fl} . \end{aligned} \tag{4.4}$$

The unusable fuel, used only for emergency situations, is assumed to be approximately 30% of the total fuel carried on board the aircraft; therefore, the total fuel weight W_{tf} is 1.42 W_{uf}. The usable fuel weight is chosen as a design variable which is adjusted by the optimization procedure so as to satisfy the range requirement.

Table 4.1 Reference Aircraft Characteristics

Weight, N:		
	Gross	4.494×10^5
	Empty	2.852×10^5
	Wing	3.020×10^4
	Payload	1.368×10^5
	Usable Fuel	2.738×10^4
Wing:		
	Aspect Ratio	14
	Area, m^2	83.98
	Span, m	34.29
	Thickness, %	12
	Sweep at c/4, deg.	15
	Taper Ratio	0.25
Tail:		
	Horizontal Area, m^2	11.71
	Vertical Area, m^2	17.74
Average Cruise:		
	Mach Number	0.78
	Lift Coefficient	0.672
	L/D (Lift to Drag Ratio)	20.7
	$\tilde{c}$ (Specific Fuel Consumption), $N/N - sec.$	0.43
Range, m:		2.34×10^6

4.2 Design Variables

The flexibility of a design depends, of course, on the variety of selected design variables. In this study, there are 48 design variables which belong to four general categories: (1) Aerodynamics, (2) Performance, (3) Control, and (4) Structures as described in Table 4.2.

Table 4.2 List of Design Variables

Aerodynamics:	
	P_1 Root chord length
	P_2 Break chord length
	P_3 Tip chord length
	P_4 Distance from root to break
	P_5 Distance from break to tip
	P_6 Leading edge sweep angle at break
	P_7 Wing twist angle at break relative to root
	P_8 Wing twist angle at tip relative to break
Performance:	
	P_9 Dynamic pressure
	P_{10} Usable fuel weight
Control:	
	P_{11} Gain # 1
	P_{12} Gain # 2
Structures:	
	$P_{13} - P_{16}$ $\pm 45°$ ply thickness (top skin)
	$P_{17} - P_{20}$ $0°$ ply thickness (top skin)
	$P_{21} - P_{24}$ $90°$ ply thickness (top skin)
	$P_{25} - P_{28}$ $\pm 45°$ ply thickness (bottom skin)
	$P_{29} - P_{32}$ $0°$ ply thickness (bottom skin)
	$P_{33} - P_{36}$ $90°$ ply thickness (bottom skin)
	$P_{37} - P_{38}$ Front spar cap cross-sectional area
	$P_{39} - P_{40}$ Rear spar cap cross-sectional area
	$P_{41} - P_{44}$ Ply angle (top skin)
	$P_{45} - P_{48}$ Ply angle (bottom skin)

The wing planform shown in Figure 4.1 is defined by the first six aerodynamic design variables (P_1 to P_6), while the wing twist is defined by the last two aerodynamic design variables (P_7 and P_8) which define the twist at the break relative to the root and the twist at the tip relative to the break. The performance variables are the dynamic pressure at cruise and the usable fuel weight which represents approximately 70% of the total fuel carried on board the aircraft. The control design

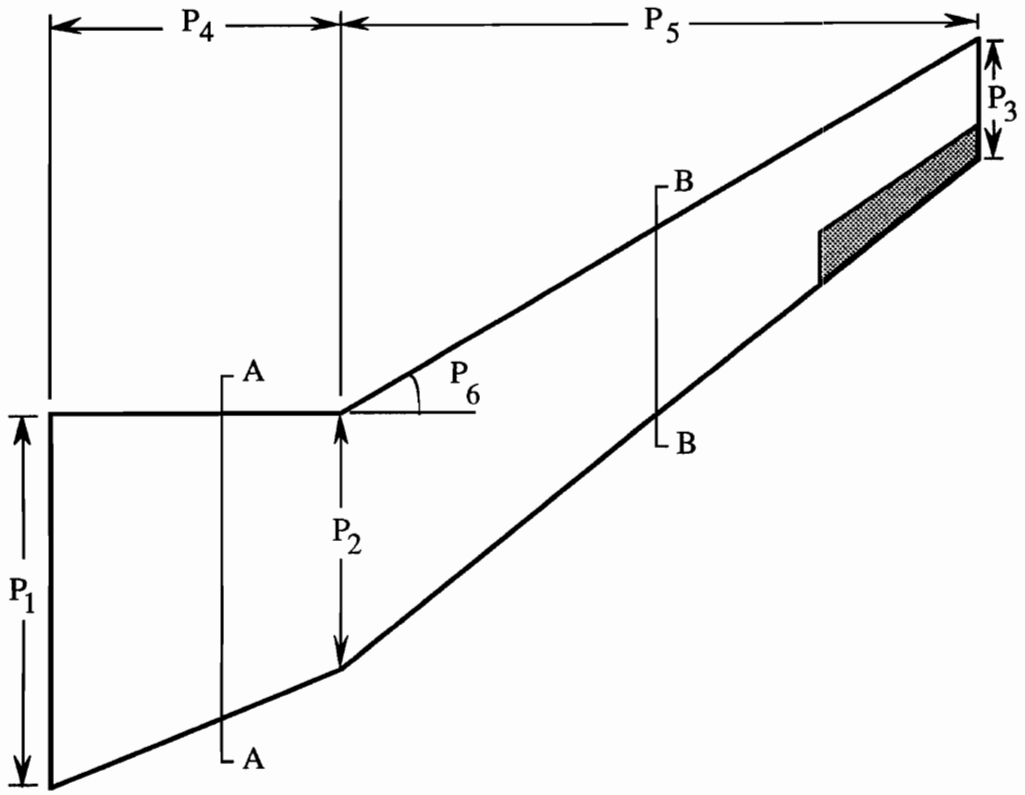

Figure 4.1 Wing-Shape Design Variables

variables are the gain values for the control system. The wing skin on the top and bottom surface is divided into four sections each, with the lines A-A and B-B in Figure 4.1 dividing the inboard and outboard wing boxes, respectively. These skin panels are made of 0°, ±45°, 90° laminates with the thickness of each ply held constant in each section; hence, there are 12 thickness design variables for the top and 12 for the bottom skin. The direction of the 0° ply in each section at the top and bottom skin as shown in Figure 4.2 is also chosen as a design variable giving a total of 8 ply orientation design variables (P_{41} to P_{48}). The cross-sectional area of the top and bottom caps on the front and rear spars are also selected as design variables.

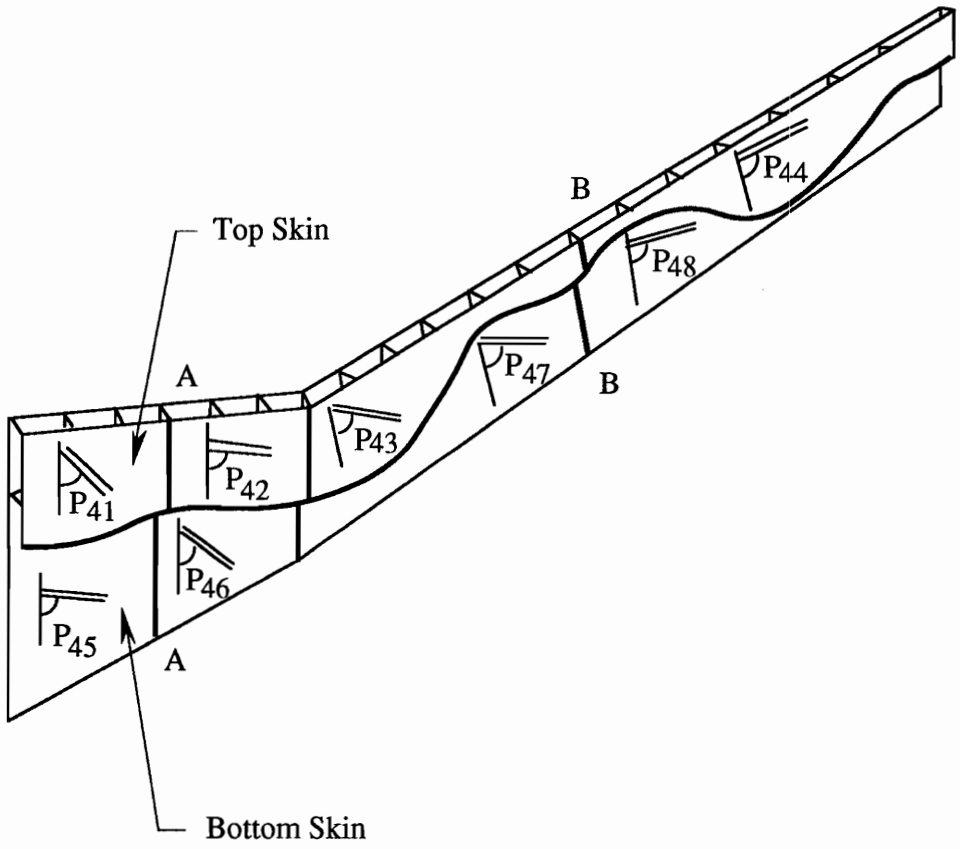

Figure 4.2 Ply Orientation Design Variables

4.3 Design Constraints

The wing design is bounded by 316 constraints as given in Table 4.3. In the following subsections the definition of all and the calculation of some of these constraints will be discussed.

4.3.1 Structural Constraints

There are 305 constraints on the wing structure which is designed to withstand a 2.5 g pull-up maneuver according to the FAA regulations with a 1.5 factor of safety. The maneuver is assumed to follow an altitude loss, and occurs at 2.5 times the cruise dynamic pressure. The allowable strains in the top and bottom skin plies

Table 4.3 List of Design Constraints

Structures:	
	1.-228. Maximum strain in composite skins
	229.-304. Maximum stress in spar caps
	305. Divergence dynamic pressure
Performance / Aerodynamics:	
	306. Range
	307. Fuel volume
	308. Landing speed
	309. Outboard-section C_L
	310. Outboard-section span
	311. Inboard-section twist
	312. Outboard-section twist
	313. Leading edge sweep angle at break
Control:	
	314.-315. Control deflection
	316. Control efficiency

Table 4.4 Wing-Structure Strain and Stress Allowables

Member	Top Skin			Bottom Skin			Spar Caps
Ply Angle	0°	±45°	90°	0°	±45°	90°	0°
ϵ_1	0.006	0.003	0.006	0.008	0.004	0.008	
ϵ_2	0.006	0.003	0.006	0.008	0.004	0.008	
ϵ_{12}	0.007	0.007	0.007	0.0093	0.0093	0.0093	
σ_1 (MPa)							1.048×10^3

and the allowable stress in the spar caps are given in Table 4.4. Since the top skin is in compression, buckling becomes an issue; however, since no buckling constraints are considered in the design, the allowable strains for the top skin are chosen to be lower than those for the bottom. Thus, in order to satisfy the strain constraints, the top skin becomes thicker which will indirectly reduce the possibility of buckling.

Of the 0°, ±45°, and 90° plies, a constraint is placed on the one with the largest strain making 114 constraints for the top and bottom skin each. Also a maximum stress constraint is placed on each of the 76 spar-cap elements in the front and aft spars. Since divergence is the most critical instability for a *cantilevered* forward-swept wing, its corresponding dynamic pressure is constrained to be at least 44% higher than the dynamic pressure at the pull-up maneuver in accordance with the FAA regulations.

4.3.2 Performance Constraints

The first of eight performance constraints is on the range which is determined as follows. If the small effect of the change in weight on the changes in the elastic deformation is ignored, the drag of the entire aircraft can be expressed as

$$D = qsC_D(C_L) \ , \tag{4.5}$$

where q is the dynamic pressure, s is the planform area of the wing and C_D is the drag coefficient which is assumed to be a function of the cruise lift coefficient C_L. The lift coefficient in cruise may be written as

$$C_L = \frac{W}{qs} \ , \tag{4.6}$$

where W is the gross weight. In order to reduce the fuel consumption during cruise, the aircraft must fly at an altitude where drag is minimum, and thus less thrust is needed to maintain equilibrium flight. The optimum dynamic pressure (and hence the optimum altitude) for cruise is determined by differentiating Eq.(4.5) with respect to q such that

$$sC_D + qs\frac{dC_D}{dC_L}\left(\frac{\partial C_L}{\partial q}\right) = 0 \ , \tag{4.7}$$

where

$$\frac{\partial C_L}{\partial q} = -\frac{W}{q^2 s} \ . \tag{4.7.a}$$

Rearranging Eq.(4.7) gives

$$q_{opt} = \frac{W}{sC_D}\frac{dC_D}{dC_L} \ , \tag{4.8}$$

with the drag corresponding to the optimum altitude determined as

$$D_{min} = W\frac{dC_D}{dC_L}(C_{L_{opt}}) \tag{4.9}$$

which indicates that D_{min} is proportional to the gross weight. Assuming that for an elastic wing, the minimum drag is still proportional to the weight, a constant of proportionality may be obtained as

$$\bar{D} = \frac{dC_D}{dC_L}|_{W=W_{50}} \ , \tag{4.10}$$

where W_{50} is the aircraft weight corresponding to half of the usable fuel. Here, $\bar{D}$ is assumed to be approximately constant over the cruise range which yields

$$D_{min} = \bar{D}W \ . \tag{4.11}$$

The rate of change of aircraft weight due to fuel consumption is given by

$$\frac{dW}{dt} = -\tilde{c}T = \tilde{c}D = -\tilde{c}\bar{D}W \ , \tag{4.12}$$

where T is the thrust and $\tilde{c}$ is the thrust specific fuel consumption, and is chosen to be equal to that for the reference aircraft given in Table 4.1. Integrating Eq.(4.12) from an initial cruise time t_i to a final cruise time t_f gives

$$log\left(\frac{W_i}{W_f}\right) = \tilde{c}\bar{D}(t_f - t_i) \ . \tag{4.13}$$

Assuming that the aircraft is flying at a constant speed, the range during cruise portion of the flight is determined as

$$R_c = V_c(t_f - t_i) = \frac{V_c}{\tilde{c}\bar{D}} log\left(\frac{W_i}{W_f}\right) . \tag{4.14}$$

where W_i and W_f are obtained from Eqs.(4.4), and V_c is the cruise speed chosen here to be 745 Km/hr. The calculation of $\bar{D}$ requires a priori knowledge of the optimum dynamic pressure. Instead of calculating q_{opt} from Eq.(4.8), it is considered a design variable, and its solution evolves with the other design variables through the integrated design process. For the design aircraft the horizontal distance traveled during the initial climb and final descent is taken to be the same as that for the reference aircraft; hence, the total range is the sum of this distance and the cruise range R_c.

The wing must be designed such that the entire fuel can be stored inside both wings; hence, a constraint is placed on the internal volume of both wings such that the total fuel would occupy 70% of the volume, while the internal wing structure, control cables, etc. would occupy the rest. To determine the wing volume the following procedure is used. The approximate volume of one wing can be determined by integrating the cross-sectional area of the wing along the semi-span as

$$\vartheta = \int_0^{P_4+P_5} k\ c^2(y)\ dy\ , \tag{4.15}$$

where $c(y)$ is the wing chord and k is the ratio of the wing cross-sectional area to c^2 at a given spanwise station. The airfoil section used here is a NASA supercritical airfoil shown in Figure 4.3, designated as SC(3)-0712(B) described by Johnson et al.[70]. Having the ordinates of the airfoil from Ref.13, the cross-sectional area was calculated using Trapezoidal rule. The value of parameter k for this airfoil is found to be 0.08035.

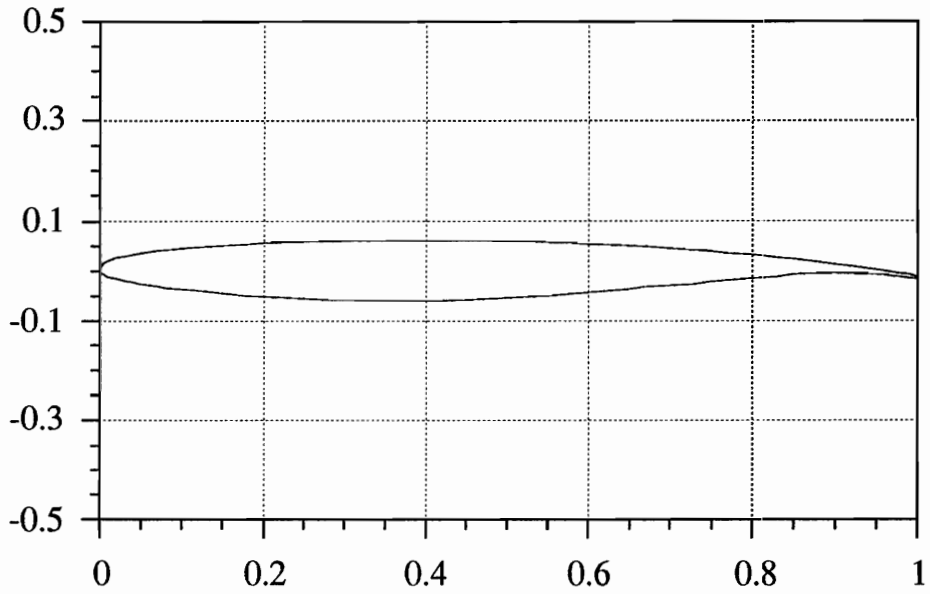

Figure 4.3 SC(3)-0712(B) Airfoil Geometry

Because of the discontinuity at the break (see Figure 4.1), the wing volume is divided into two parts as

$$\vartheta = \int_0^{P_4} kc_1^2(y)\, dy + \int_{P_4}^{P_4+P_5} kc_2^2(y)\, dy \;, \tag{4.16}$$

where

$$c_1(y) = P_1 - \left(\frac{P_1 - P_2}{P_4}\right) y \;,$$

$$c_2(y) = P_2 - \left(\frac{P_2 - P_3}{P_5}\right)(y - P_4) \;.$$

Integrating Eq.(4.16) gives

$$\vartheta = \frac{kP_4}{3}[P_1^2 + P_2^2 + P_1P_2] + \frac{kP_5}{3}[P_2^2 + P_3^2 + P_2P_3] \;. \tag{4.17}$$

The total volume available for the fuel is given as

$$\vartheta_{fa} = 2 \times 0.7\vartheta \ , \tag{4.18}$$

and the required fuel volume is determined based on the total fuel weight as

$$\vartheta_{fr} = \frac{W_{tf}}{\rho_f} \ , \tag{4.19}$$

with the fuel density ρ_f equal to 7385.76 N/m^3.

Another important design consideration is landing. Here, a landing (approach) speed constraint of 278 Km/hr (150 Kt) at approximately 2133 m (7000 ft) is imposed. The required landing speed for such aircraft is typically 30% higher than the stall speed. Since at landing the high lift devices such as flaps are extended, the landing C_L is assumed to be 1.5 times the maximum lift coefficient $C_{L_{max}}$ (with no flaps extended). Hence, the required approach speed is determined as

$$V_{L_r} = 1.3\sqrt{\frac{2W}{\rho s(1.5C_{L_{max}})}} \ . \tag{4.20}$$

To permit an emergency landing, the maximum landing weight is chosen to be the same as the take-off gross weight, W. This constraint also puts a lower bound on the total wing area.

To prevent the outboard-wing chord from shrinking to a value which results in a large lift coefficient, a constraint is placed on the outboard-section lift coefficient $C_{L_{out}}$ such that $C_{L_{out}} < 1.0$. Furthermore, since most of the aerodynamic and structural elements are located at the outboard-section, a constraint is imposed on the outboard span P_5 such that $P_5 > 0.6(P_4 + P_5)$. Furthermore, the two twist design variables P_7 and P_8 are bounded each between $\pm 4°$. Since the eventual goal is to design the aircraft for transonic Mach numbers, it is important to have a forward sweep configuration. However, since the Mach number currently used in this study is below the drag rise Mach number, the optimizer will try to remove the sweep (as was the case in the recent study[62]). Therefore, a lower bound of 20° is imposed on the leading-edge forward sweep angle at break.

4.3.3 Control Constraints

The problems associated with the control system include saturation and reversal. To prevent the control system from saturating in a situation such as an encounter with a gust, a limit must be imposed on the control system gains or control deflection in such a scenario. This limit leaves the control system with enough effectiveness to combat divergence on top of gust. To determine the control deflection due to a vertical gust the following procedure is used.

Using the FAR -25[71] (Federal Aviation Regulations for Transport Aircraft) the derived gust velocity V_g is given as

$$\begin{aligned} V_g &= 7.62 \ \ m/sec\ , && \text{sea level} < h < 6096.00\ m \\ V_g &= 10.162032 - 0.000417\ h \ \ m/sec, && 6096.00 < h < 15240.00\ m\ . \end{aligned} \tag{4.21}$$

This gust velocity corresponds to the design dive speed V_d curve in the $V-n$ diagram described in FAR-25

$$V_d = 1.25 V_c\ , \tag{4.22}$$

where V_c is the cruise speed. Having determined the gust and dive speeds, the gust-induced angle of attack increment $\Delta\alpha_g$ is determined as

$$\Delta\alpha_g = \tan^{-1}\left(\frac{V_g}{V_d}\right)\ . \tag{4.23}$$

In the aeroservoelastic analysis discussed in Chapter 6, the control surface deflection due to gust-induced angle of attack will be determined. A limit of $\pm 10°$ is imposed on this deflection to avoid saturation.

The control efficiency can be defined as the ratio of the root bending moment produced by a control deflection to that produced by the same deflection on an equivalent rigid wing. To avoid control reversal this ratio must be greater than zero. In this study, the simpler root bending moment is used instead of the rolling moment since at reversal the root bending moment due to control deflection also goes to zero. To avoid the loss of control effectiveness, however, a lower bound of 0.5 is imposed on the control efficiency.

5. MULTIDISCIPLINARY ANALYSIS TOOLS

The design of the forward-swept transport wing requires analysis tools with a greater degree of sophistication than those used in the simplified wing design discussed earlier (in chapters 2 and 3). This is especially true in the case of aerodynamic and structural models. In this chapter the model and method of analysis used for each discipline will be discussed.

5.1 Structural Model

The structural analysis is performed on a three-dimensional finite-element model of the wing developed by Kao[63] and slightly modified in this study. The model, shown in Figure 5.1 is made up of 1093 elements joined at 178 nodes with 534 total degrees of freedom. A list of the structural members with the corresponding number of finite elements used for each is given in Table 5.1. The mesh is generated based on two sets of information: the geometric shape of the wing, and the structural configuration. The wing geometry is defined by the six shape design variables described previously in chapter 4, and the airfoil geometry at the root, break and the tip. The structural configuration is defined by the number of spars, the number of ribs in the inboard and outboard sections of the wing, the rib-spar intersection angle measured relative to the front spar, the rib spacing measured normal to the rib, the locations of the ribs connected to the leading and trailing edges of the wing, and finally the location of the front and rear spars relative to the leading edge of the wing. The wing box is constructed with 4 spars and 19 ribs enclosed by the top and bottom skins. The spars are modeled by a series of one-dimensional truss

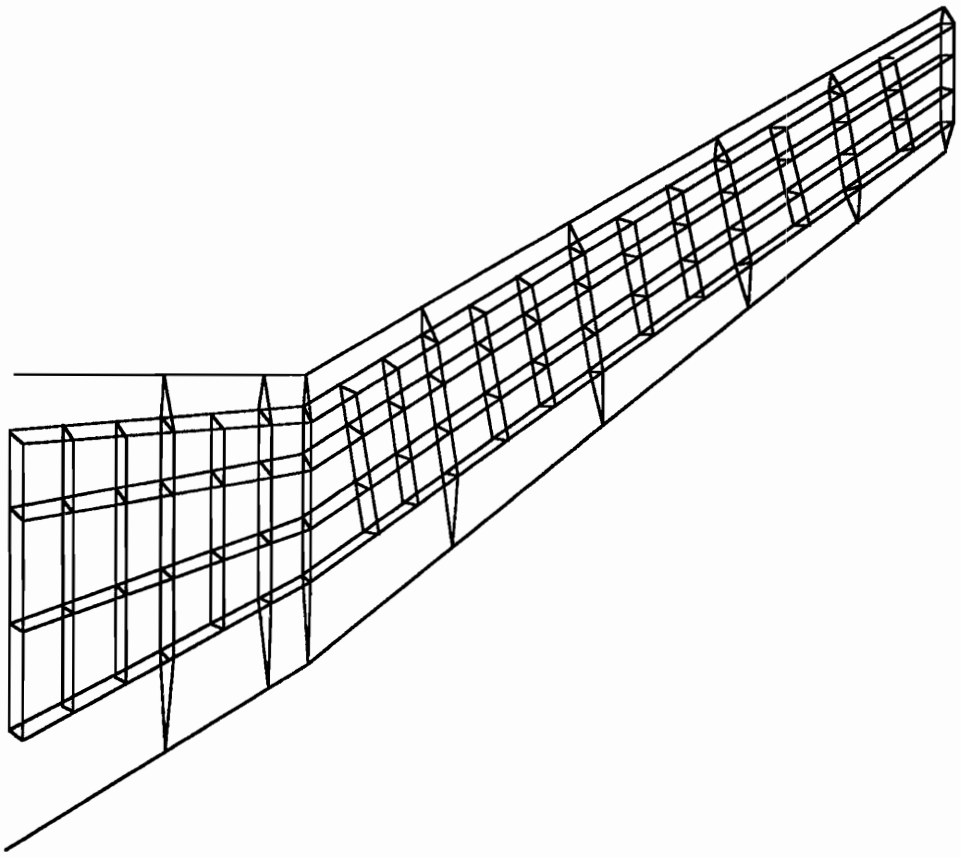

Figure 5.1 Finite-Element Model of the Wing

elements for the caps and two-dimensional (quadrilateral) elements for the shear webs. Each rib is modeled by three quadrilateral shear web elements which are attached to the spar shear webs with a vertical-rod element placed at each rib-spar joint. The thicknesses of all shear webs and the cross-sectional areas of the spar

Table 5.1 Finite-Element Model Break Down

Member	No. of Elements
Skin	684
Shear Web	133
Spar Cap	152
Vertical Rod	76
L.E. & T.E. Trusses	48

caps on the middle two spars along with all other truss elements are held fixed, throughout the design, at their minimum gage value given in Table 5.2. The top and bottom skins are modeled by two-dimensional (triangular) elements. A close-up

Table 5.2 Minimum Gage Value for Each Structural Member

Member	Minimum Gage
0° ply	0.0001250 m
±45° ply	0.0002500 m
90° ply	0.0001250 m
Shear Web*	0.0025000 m
Spar Cap	0.0001250 m^2
Vertical Rod*	0.0000625 m^2
L.E. & T.E. Trusses*	0.0002500 m^2
* member held fixed in the design	

view of a single wing-box cell with various structural members are shown in Figure 5.2. The leading and trailing edges of the wing are modeled by a series of one-dimensional truss elements. The wing structure is made of advanced composite

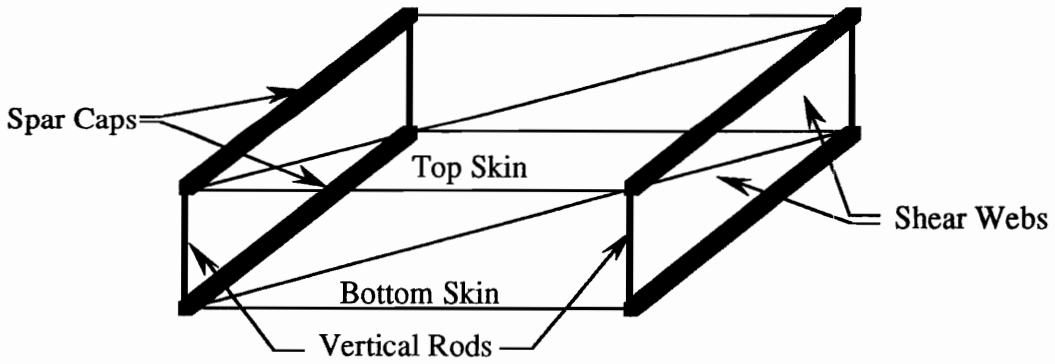

Figure 5.2 Close-Up View of a Single Wing-Box Cell

materials with properties for each member given in Table 5.3. The wing-top and bottom skin each is divided into four sections. As shown in Figure 5.3, each skin panel is made of a three-layer (0°, ±45°, 90°) laminate with the angle between the

Table 5.3 Wing-Structure Material Properties

Structural Member	Trusses	Skins			Shear Webs
Ply Angle	0°	0°	±45°	90°	Isotropic
Density (N/m^3)	1.574×10^4	1.574×10^4	1.574×10^4	1.574×10^4	1.574×10^4
E_1 (MPa)	1.310×10^5	1.310×10^5	2.202×10^4	1.303×10^4	7.563×10^4
E_2 (MPa)		1.303×10^4	2.202×10^4	1.310×10^5	
G_{12} (MPa)		6.412×10^4	3.399×10^4	6.412×10^4	
ν_{12}		0.38	0.718	0.0378	0.718

element line and 0° ply direction being a design variable. Also, the three layers in each panel are allowed to have different thicknesses. Hence, the top and bottom

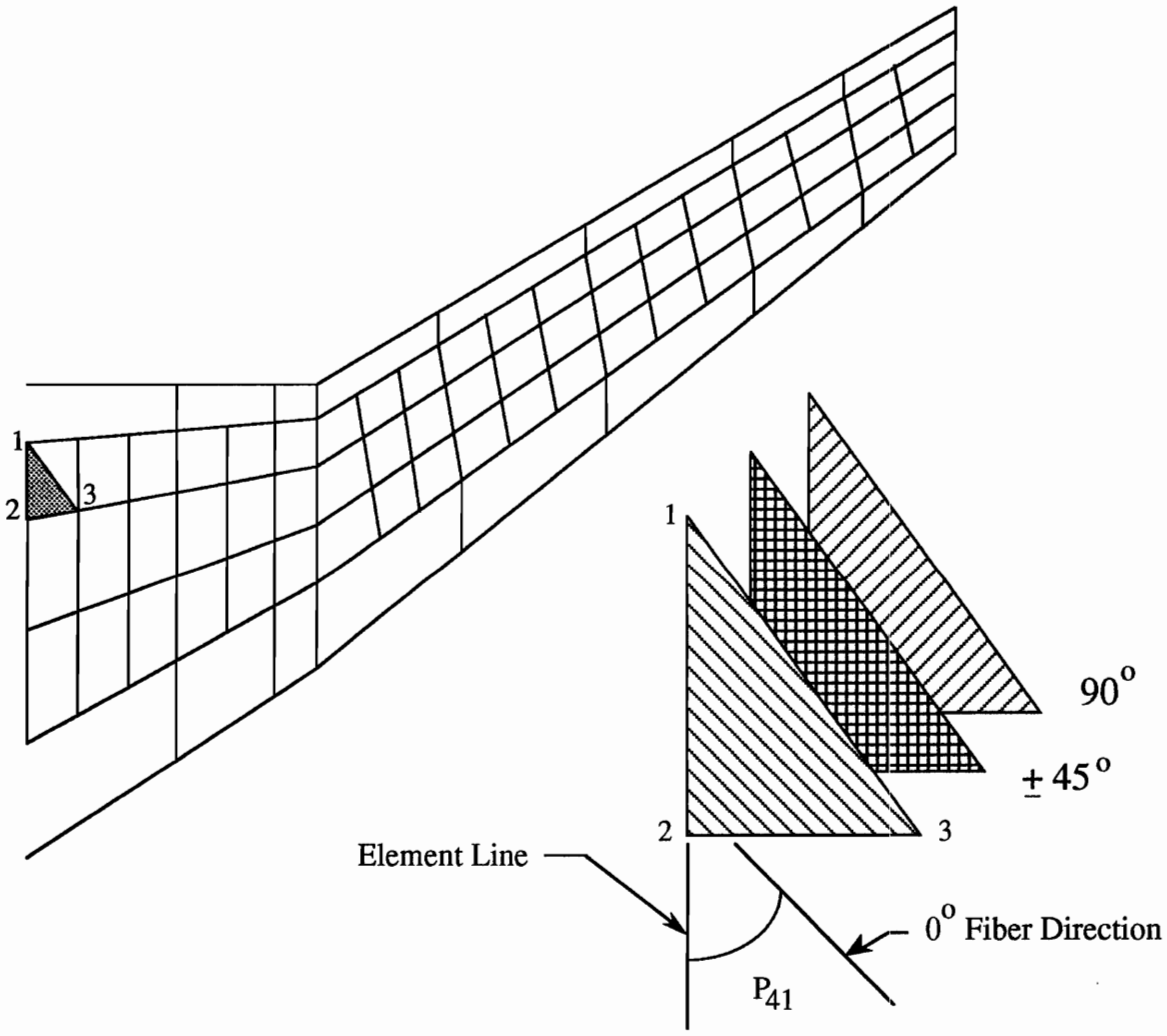

Figure 5.3 Ply Orientations in Each Panel

skins may or may not be symmetrical. The flexibility of having different ply orientations and thicknesses enhances the aeroelastic tailoring capability during the design. With the finite- element model and the material properties defined, the structural analysis is carried out using a modified version of WIDOWAC[72], a finite-element-based structural analysis and optimization code. This code is used to determine the nodal displacements due to inertia loads and the applied aerodynamic loads which are supplied as input. These deflections are then used for the aerodynamic load calculations. The post-processor of WIDOWAC gives the strains in the skin and the stresses in the spar caps which are used for structural constraint calculation during the design optimization.

5.2 Aerodynamic Model

The aerodynamic model used in this study was developed through previous research by Polen[61] and Unger[73]. The aerodynamic analysis is carried out using the vortex lattice method. This method has been commonly used for calculating the lift and induced drag in the subsonic range with satisfactory results. Here, the wing area is divided to 140 skew panels, 60 for the inboard and 80 for the outboard section of the wing. The number of panels in the chordwise direction is 10 in both sections. The airfoil section used for all spanwise stations is a supercritical airfoil designated as SC(2)-0712(B) described by Johnson et al.[70], and shown previously in Figure 4.5. A horseshoe vortex is placed in each panel with the control point located at the 75% chord of the panel as shown in Figure 5.4.

Using the Biot-Savart law, the relationship between the strength of each vortex filament and the velocity induced by that vortex at a point over the wing is obtained.

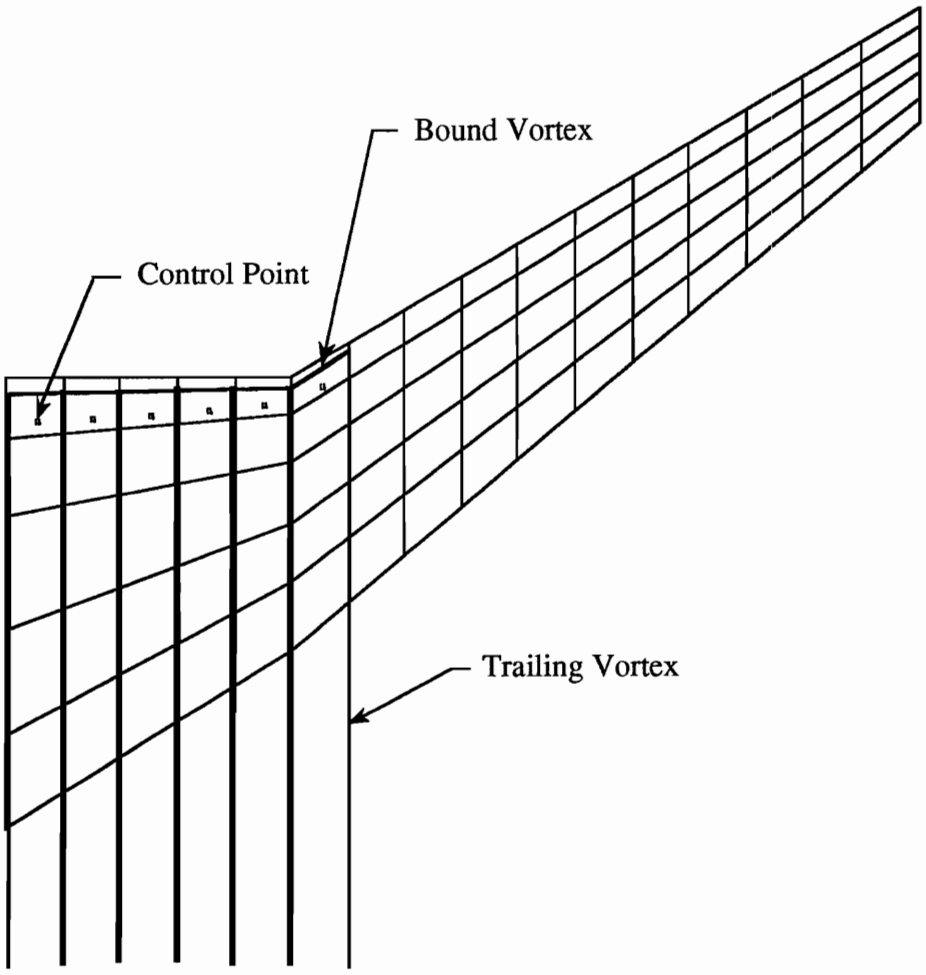

Figure 5.4 Vortex-Lattice Model

Summing the contributions of all horseshoe vortices over both wings, the total induced velocity at each control point is determined. By enforcing flow tangency at each panel, a vector of circulation strength $\mathbf{\Gamma}$ is computed. The aerodynamic forces are computed from a local application of the Kutta-Joukowski theorem as

$$\mathbf{F} = \rho \mathbf{V} \times \mathbf{\Gamma} \, , \tag{5.1}$$

and compressibility effects are included through a Göthert transformation. Equation (5.1) is used to calculate the lift but not the induced drag. Recent study[62] indicated that the induced drag obtained from this equation was low, with span

efficiencies greater than unity. The approach more commonly used involves the calculation of the induced drag from the far-field or Trefftz plane. In the far-field, the flow is approximated as a two dimensional flow (with no variations in the streamwise direction) induced by the trailing vortex sheet. The circulation distribution over the wing is represented by a Fourier sine series as

$$\Gamma(\psi) = 2bV_\infty \sum_{n=1}^{N_{max}} A_n \sin n\psi \ , \tag{5.2}$$

where V_∞ is the free-stream velocity, b is the span and $\cos\psi = 2y/b$. Having determined the circulation distribution previously from the vortex lattice method, the coefficients A_n are calculated from Eq.(5.2). Then the induced drag is determined as

$$D_i = -\rho_\infty V_\infty^2 b^2 \sum_{n=1}^{N_{max}} n A_n^2 \sin^2 n\psi \ , \tag{5.3}$$

The induced drag coefficient is obtained by integrating Eq.(5.3) and nondimensionalizing the result such that

$$C_{D_i} = \frac{C_L^2}{\pi \ AR \ e} \ , \tag{5.4}$$

where

$$e = \left[1 + \sum_{n=2}^{N_{max}} n\left(\frac{A_n}{A_1}\right)^2\right]^{-1} \ .$$

AR is the wing aspect ratio and C_L is the total lift coefficient given by

$$C_L = \frac{L}{qs} \ , \tag{5.5}$$

where

$$L = 2\int_0^{b/2} l \ dy \ , \tag{5.5.a}$$

and

$$l = \rho_\infty V_\infty \Gamma \ . \tag{5.5.b}$$

The calculations were performed with a 32 term series expansion using the LIDRAG subprogram found in TRO3D computer code[74]. The viscous drag for each wing section is calculated from the measured airfoil drag polar given in Ref. 5. The drag associated with the aircraft fuselage and the tail section is assumed to be constant and equal to that for the reference aircraft (described in Table 4.1). The drag coefficient associated with the fuselage and the tail at zero angle of attack is determined by subtracting the total wing drag coefficient from the aircraft drag coefficient as

$$C_{D_{F\&T}} = C_{D_{AC}} - C_{D_W} \tag{5.6}$$

where $C_{D_{AC}}$ and C_{D_W} are the total drag coefficient and the sum of wing induced and viscous drag coefficients of the reference aircraft at zero angle of attack, respectively. Equation (5.6) may not be valid in a comprehensive aircraft design, but for this study it is a reasonable approximation.

5.3 Aerodynamic-Structural Interface

When dealing with a multidisciplinary analysis, the incompatibility of the models used for various disciplines becomes an issue. For instance, as is the case here, the structural finite-element nodes do not match the location and the number of aerodynamic control points. Hence, it is necessary to develop a mechanism by which the aerodynamic loads are transferred to the structural grid nodes and the structural deformations are transferred to the aerodynamic control points. To achieve this, it is assumed that the effect of the aerodynamics on structural deformations can be approximated by lumping the aerodynamic forces at n_l structural grid nodes

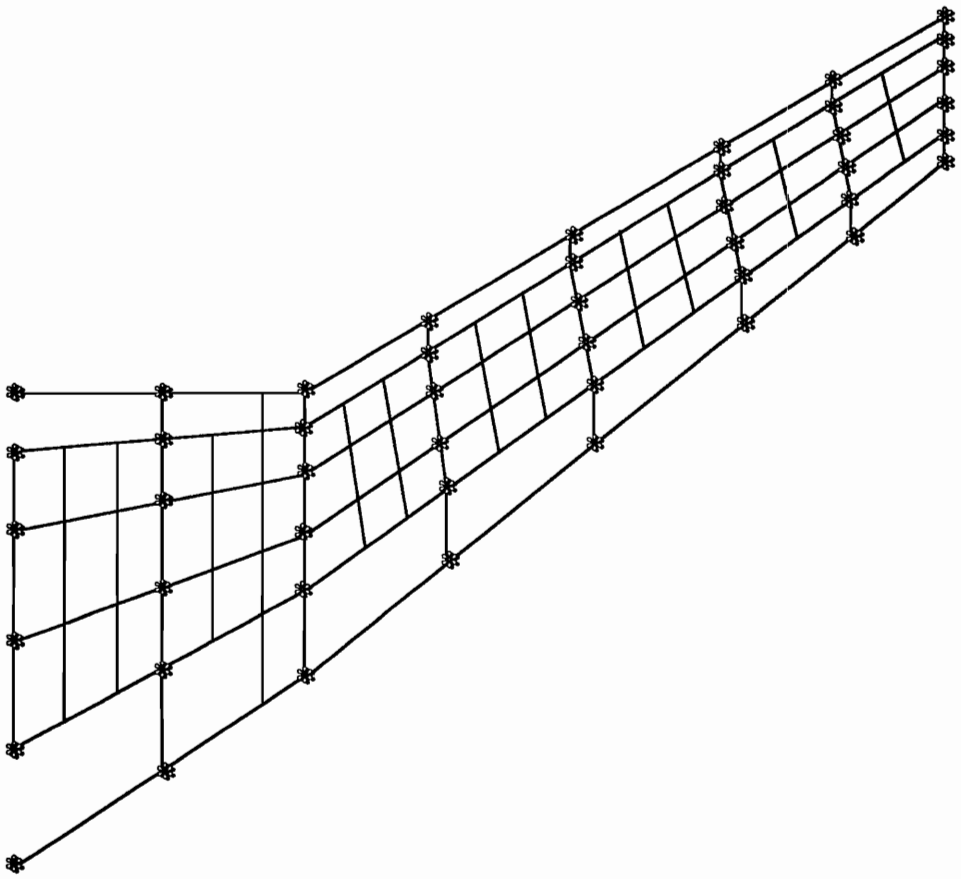

Figure 5.5 Load-Set Nodes

(which will be referred to as the load set), and including only the vertical components of loads. Here, n_l is taken to be 48 with locations shown in Figure 5.5. Furthermore, it is assumed that the the effect of structural deformations on the aerodynamic response can be approximated in terms of the vector of vertical displacements $\boldsymbol{w}$ at the load set. The interface used in this study is that developed by Unger[73]. In it, a set of linear isoparametric functions are used to represent the structural deformations in a functional form. These shape functions are then used to interpolate the deflection at the load set nodes to the aerodynamic control points and forces to the load set nodes conserving work and energy.

5.4 Control Model

The control system used in this study consists of an aileron type control surface located at the aft section of the wing near the tip as shown in Figure 5.6, with 1 actuator and 4 sensors. The control surface is assumed rigid with dimensions kept as a fixed percentage of the wing outboard-section span and chord such that its hinge line and leading edge lie behind the aft spar. The control surface size is approximately 3% of the total wing area which is similar to the aileron on the Boeing 727[75], for example. The weight of the actuator is assumed negligible compared to the structural weight of the wing, and hence is ignored in both analysis and design. The gains associated with control system are treated as design variables to be determined during the design optimization. Of the 4 sensors, 2 are placed at the break and 2 at the tip section of the wing as shown in Figure 5.6. These sensors measure the vertical deflection at those points.

The control deflection β is assumed to be related to the twist at the break and the tip such that

$$\beta = P_{11}\left(\frac{w_{s_1} - w_{s_2}}{P_2}\right) + P_{12}\left(\frac{w_{s_3} - w_{s_4}}{P_3}\right) , \tag{5.7}$$

where w_{s_1}, w_{s_2}, w_{s_3}, and w_{s_4} are the vertical displacements at the nodes where sensors 1, 2, 3, and 4 are located, respectively. P_2 and P_3 are the chord length design variables at the break and the tip, respectively, and P_{11} and P_{12} are the gain design variables for the control system. Writing Eq.(5.7) in vector form, and allowing the control to be deflected only when the load set deflections are different from those at the $2.5g$ pull-up maneuver, gives

$$\beta = \mathbf{G}^T(\boldsymbol{w} - \boldsymbol{w}_m) , \tag{5.8}$$

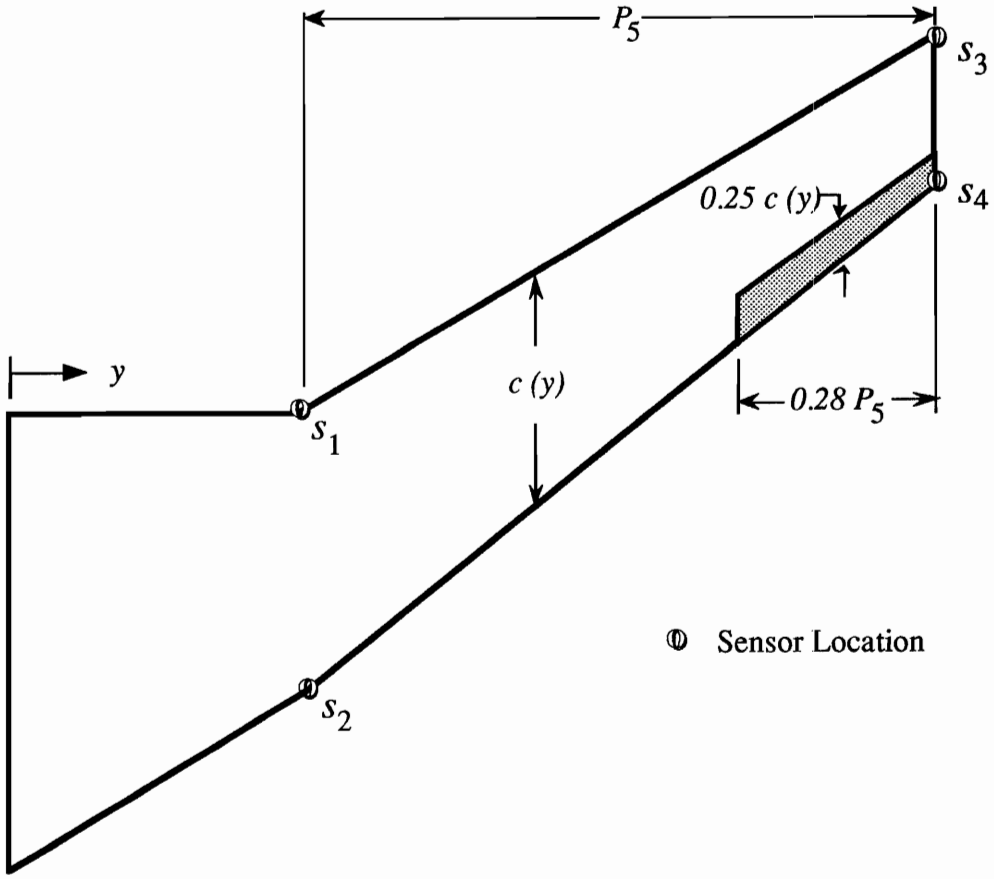

Figure 5.6 Control Surface and Sensor Locations

where β is measured positive down, and $\boldsymbol{w}$ is the load set deflection vector with $\boldsymbol{w}_m$ representing its value at maneuver. Equation (5.8) is a control law based on feed-back control theory. The vector $\mathbf{G}$ in Eq.(5.8) is defined as

$$\mathbf{G}^T = \boldsymbol{g}^T \, H \; . \tag{5.9}$$

The elements in vector $\boldsymbol{g}$ are:

$$g_1 = \frac{P_{11}}{P_2} \quad \text{(for sensor \#1)} \; , \tag{5.9.a}$$

$$g_2 = -\frac{P_{11}}{P_2} \quad \text{(for sensor \#2)} \; , \tag{5.9.b}$$

$$g_3 = \frac{P_{12}}{P_3} \quad \text{(for sensor \#3)} \; , \tag{5.9.c}$$

$$g_4 = -\frac{P_{12}}{P_3} \quad \text{(for sensor \#4)} \; , \tag{5.9.d}$$

where H is a [4 x 48] Boolean matrix which expands $\boldsymbol{g}$ to the entire load set. All the elements of H are zero except for $h_{1,13}$, $h_{2,18}$, $h_{3,43}$ and $h_{4,48}$ which are all equal to one. The sign and magnitude of P_{11} and P_{12} will be determined during the design optimization. The sign of P_{11} and P_{12} will be determined based on the fact that whether a downward or an upward control deflection is needed to suppress the wing divergence instability. Since the wing is forward swept with tailored composite skins, it is not intuitively obvious which direction the control surface must be deflected to push the center of pressure aft to delay or suppress divergence.

6. AEROSERVOELASTIC ANALYSES AND SENSITIVITIES

The structure, aerodynamic and control disciplines are all coupled together in the aeroservoelastic analysis. In order to formulate the proper equations, a number of assumptions are made. As mentioned previously in section 5.2, the aerodynamic and structure models are linked together by assuming that the effect of the aerodynamics on structural deformations can be approximated by lumping the aerodynamic forces at the load set nodes (see Figure 5.5), and including only the vertical components of the loads $\mathbf{F}_a$. Also, it is assumed that the effect of structural deformations on the aerodynamic response can be approximated in terms of the vertical displacements w at the load set. Furthermore, the effect of the control deflection β on the aerodynamic response can be approximated in terms of the vertical displacements at the load set nodes located at the trailing edge of the control surface. Finally, the overall response of the aircraft is assumed to affect the wing by changing the root angle of attack α.

With these assumptions in mind, the aerodynamic load vector $\mathbf{F}_a$ is obtained from an aerodynamic analysis using the vortex lattice method discussed in the previous chapter. The aerodynamic load can be represented in a functional form as

$$\mathbf{F}_a = f_1(\mathbf{P}, \alpha, w, \beta) \ , \tag{6.1}$$

where $\mathbf{P}$ is a vector of design variables, and is known for the analysis problem.

The angle of attack α is obtained from aircraft equilibrium in the vertical direction as

$$f_2(\mathbf{P}, \mathbf{F}_a) = \frac{1}{2} nW - \mathbf{N}^T \mathbf{F}_a = 0 \ , \tag{6.2}$$

where n is the load factor and $\mathbf{N}^T$ is a summation vector.

The vertical displacements at the load set $\boldsymbol{w}$ are obtained from a structural analysis using a modified version of the finite-element based program, WIDOWAC. First, the displacement at each finite-element node is determined by solving

$$K(\mathbf{P})\mathbf{U} = T\mathbf{F}_a + n\mathbf{F}_I(\mathbf{P}) \ , \tag{6.3}$$

where K is the stiffness matrix, $\mathbf{U}$ is the finite-element nodal displacement vector, T is a Boolean matrix which expands $\mathbf{F}_a$ to the full set of degrees of freedom, and $\mathbf{F}_I$ is the inertia and gravitational load vector. The strains in the skin and stresses in the spar cap elements are calculated from the displacement vector $\mathbf{U}$. The vertical displacements at the load set are extracted from $\mathbf{U}$ as

$$\boldsymbol{w} = T^T\mathbf{U} \ . \tag{6.4}$$

Equations (6.3) and (6.4) can be combined as

$$\boldsymbol{w} = \boldsymbol{f}_3(\mathbf{P}, \mathbf{F}_a) \ . \tag{6.5}$$

The control deflection β is determined from the control law given in Eq.(5.8), and can be represented as

$$\beta = f_4(\mathbf{P}, \boldsymbol{w}) = \mathbf{G}^T(\mathbf{P})\ (\boldsymbol{w} - \boldsymbol{w}_m) \ , \tag{6.6}$$

where $\boldsymbol{w}_m$ is the load-set vertical displacement vector at maneuver. The root bending moment M_b is determined as

$$M_b = f_5(\mathbf{P}, \mathbf{F}_a) = \boldsymbol{y}^T(\mathbf{P})\mathbf{F}_a \ , \tag{6.7}$$

where $\boldsymbol{y}$ is a vector of load-set spanwise coordinates.

Using the modular approach of Sobieski[42], the individual discipline analysis procedures are treated as *black boxes* which do not need to be changed in the integration procedure. Here, $\boldsymbol{f}_1$ represents an aerodynamic black box, $\boldsymbol{f}_3$ represents a structural black box, and f_4 represents a control black box.

6.1 Aeroelastic Analysis at Maneuver

Assuming that at maneuver the pilot trims the control deflection to zero (i.e., β=0), only the aeroelastic (aerodynamic-structural) interactions need to be considered. Equations (6.1), (6.2) and (6.5) form a set of nonlinear coupled equations for $\mathbf{F}_a$, $\boldsymbol{w}$ and α.

Given an initial estimate for the solution $\mathbf{F}_a^0$, $\boldsymbol{w}^0$ and α^0, Newton's method is used to improve that estimate. The iterative process may be written as

$$J\Delta\mathbf{X} = \Delta\boldsymbol{f}, \tag{6.8}$$

where

$$\Delta\mathbf{X} = \begin{Bmatrix} \Delta\mathbf{F}_a \\ \Delta\alpha \\ \Delta\boldsymbol{w} \end{Bmatrix}, \tag{6.8.a}$$

and

$$\Delta\boldsymbol{f} = \begin{Bmatrix} \boldsymbol{f}_1(\mathbf{P}, \alpha^0, \boldsymbol{w}^0) - \mathbf{F}_a^0 \\ f_2(\mathbf{P}, \mathbf{F}_a^0) \\ \boldsymbol{f}_3(\mathbf{P}, \mathbf{F}_a^0) - \boldsymbol{w}^0 \end{Bmatrix}, \tag{6.8.b}$$

and the Jacobian J is given as

$$J = \begin{bmatrix} I & -\partial\boldsymbol{f}_1/\partial\alpha & -\partial\boldsymbol{f}_1/\partial\boldsymbol{w} \\ -\partial f_2/\partial\mathbf{F}_a & 0 & 0 \\ -\partial\boldsymbol{f}_3/\partial\mathbf{F}_a & 0 & I \end{bmatrix}$$

$$= \begin{bmatrix} I & -q\mathbf{R} & -qA \\ \mathbf{N}^T & 0 & 0 \\ -S & 0 & I \end{bmatrix}. \tag{6.8.c}$$

The Jacobian is given in terms of the dynamic pressure q, the incremental aerodynamic force vector $q\mathbf{R}$, the aerodynamic influence coefficient matrix qA and the flexibility matrix S. The incremental aerodynamic force vector is defined such that its component qR_i represents the change in F_{a_i} due to a unit change in angle of attack α, and the aerodynamic influence coefficient matrix is defined such that its component qa_{ij} represents the change in F_{a_i} due to a unit change in w_j. Similarly,

the flexibility matrix is defined such that its component s_{ij} represents the change in w_i due to a unit change in F_{a_j}.

Partial solution of Eq.(6.8) yields the following three equations for the increments $\Delta \boldsymbol{w}$, $\Delta\alpha$ and $\Delta \mathbf{F}_a$:

$$(I - qSA^*)\Delta \boldsymbol{w} = SB\Delta \boldsymbol{f}_1 + \frac{S\mathbf{R}}{\mathbf{N}^T\mathbf{R}}\Delta f_2 + \Delta \boldsymbol{f}_3 \ , \tag{6.9}$$

$$\Delta\alpha = \frac{\Delta f_2 - \mathbf{N}^T\Delta \boldsymbol{f}_1 - q\mathbf{N}^T A\Delta \boldsymbol{w}}{q\mathbf{N}^T\mathbf{R}} \ , \tag{6.10}$$

$$\Delta \mathbf{F}_a = \Delta \boldsymbol{f}_1 + q\mathbf{R}\Delta\alpha + qA\Delta \boldsymbol{w} \ , \tag{6.11}$$

where

$$B \equiv I - \frac{\mathbf{R}\mathbf{N}^T}{\mathbf{N}^T\mathbf{R}} \ ,$$

$$A^* \equiv BA \ .$$

Starting with a rigid wing approximation $\mathbf{F}_a^0 = \mathbf{F}_{ar}$, $\alpha^0 = \alpha_r$ and $\boldsymbol{w}$= 0 where

$$\mathbf{F}_{ar} = \boldsymbol{f}_1 + q\alpha_r\mathbf{R} \ , \tag{6.12}$$

$$\alpha_r = \frac{\frac{1}{2}nW - \mathbf{N}^T\boldsymbol{f}_1}{q\mathbf{N}^T\mathbf{R}} \ , \tag{6.13}$$

and executing a single Newton iteration gives the approximate flexible wing response at maneuver. The force vector $\boldsymbol{f}_1$ is evaluated through a vortex-lattice analysis at conditions ($\mathbf{P}^0, \alpha = 0$ and $\boldsymbol{w} = 0$). The derivative vector $\mathbf{R}$ as defined in Eq.(6.8.c) is also calculated at the same conditions by perturbing the angle of attack, calculating the corresponding force vector, and then using finite-differences to determine $\mathbf{R}$. The gross weight W is calculated from Eqs.(4.1) and (4.2). From equilibrium equation in vertical direction, Eq.(6.13), the rigid-wing angle of attack α_r is calculated next. The aerodynamic influence coefficient matrix A is calculated by finite-differences by perturbing each load-set node in vertical direction and calculating the vertical load vector $\boldsymbol{f}_1$. The A matrix is calculated at conditions ($\mathbf{P}^0$, $\alpha = \alpha_r$ and $\boldsymbol{w} = 0$).

No aeroelastic calculation is done at cruise. This implies that the cruise range is determined based on the drag calculated under rigid-wing conditions (i.e., $\mathbf{F}_a = \mathbf{F}_{ar}$, $\alpha = \alpha_r$, and $w = 0$) with $q = q_c = P_9$. This assumption is permissible because the wing will be manufactured with an initial twist which under cruise loading will be reduced to that defined by design variables P_7 and P_8.

6.2 Gust-Induced Control Deflection Calculation

Following the discussion on control saturation in chapter 4, it is necessary to calculate the control deflection due to gust. Equation (4.23) gives the gust induced angle of attack increment as

$$\Delta\alpha_g = \tan^{-1}\left(\frac{V_g}{V_d}\right) , \tag{4.23}$$

where V_g is the vertical gust speed and V_d is the design dive speed.

The gust-induced control deflection is calculated at a fixed angle of attack, because it is assumed that the pilot does not react fast enough to change the angle of attack in an encounter with a gust. It is also assumed that $\Delta\alpha_g$ is small, so that the effect of the gust can be calculated by a linear approximation. That is

$$\beta_a = \frac{\partial\beta}{\partial\Delta\alpha_g}\Delta\alpha_g , \tag{6.14}$$

where β_a is the approximate value of the control deflection. To obtain $\partial\beta/\partial\Delta\alpha_g$ Eqs. (6.1), (6.5) and (6.6) are differentiated with respect to $\Delta\alpha_g$ for a given set of design variables $\mathbf{P}$ as

$$\frac{\partial\mathbf{F}_a}{\partial\Delta\alpha_g} = \frac{\partial f_1}{\partial\Delta\alpha_g} + \frac{\partial f_1}{\partial w}\frac{\partial w}{\partial\Delta\alpha_g} + \frac{\partial f_1}{\partial\beta}\frac{\partial\beta}{\partial\Delta\alpha_g} , \tag{6.15}$$

$$\frac{\partial w}{\partial\Delta\alpha_g} = \frac{\partial f_3}{\partial\mathbf{F}_a}\frac{\partial\mathbf{F}_a}{\partial\Delta\alpha_g} , \tag{6.16}$$

$$\frac{\partial \beta}{\partial \Delta \alpha_g} = \frac{\partial f_4}{\partial \boldsymbol{w}} \frac{\partial \boldsymbol{w}}{\partial \Delta \alpha_g} \ . \tag{6.17}$$

Rewriting Eqs.(6.14) to (6.16) in matrix form gives

$$\begin{bmatrix} I & -qA & -q\mathbf{C} \\ -S & I & 0 \\ 0 & -\mathbf{G}^T & I \end{bmatrix} \begin{Bmatrix} \partial \mathbf{F}_a / \partial \Delta \alpha_g \\ \partial \boldsymbol{w} / \partial \Delta \alpha_g \\ \partial \beta / \partial \Delta \alpha_g \end{Bmatrix} = \begin{Bmatrix} \mathrm{q}\mathbf{R} \\ 0 \\ 0 \end{Bmatrix} , \tag{6.18}$$

where $q\mathbf{C}$ is the incremental aerodynamic force vector with qC_i representing the change in F_{a_i} due to a unit change in β. Equation (6.18) is solved for the derivatives of $\mathbf{F}_a$, $\boldsymbol{w}$ and β with respect to $\Delta \alpha_g$.

6.3 Control Efficiency Calculation

The control efficiency is determined by differentiating Eqs.(6.1), (6.5) and (6.7) with respect to control deflection β for a given value of $\mathbf{P}$ as

$$\frac{\partial \mathbf{F}_a}{\partial \beta} = \frac{\partial \boldsymbol{f}_1}{\partial \boldsymbol{w}} \frac{\partial \boldsymbol{w}}{\partial \beta} + \frac{\partial \boldsymbol{f}_1}{\partial \beta} \ , \tag{6.19}$$

$$\frac{\partial \boldsymbol{w}}{\partial \beta} = \frac{\partial \boldsymbol{f}_3}{\partial \mathbf{F}_a} \frac{\partial \mathbf{F}_a}{\partial \beta} \ , \tag{6.20}$$

$$\frac{\partial M_b}{\partial \beta} = \frac{\partial f_4}{\partial \mathbf{F}_a} \frac{\partial \mathbf{F}_a}{\partial \beta} \ . \tag{6.21}$$

Writing Eqs.(6.19) to (6.21) in matrix form gives

$$\begin{bmatrix} I & -qA & 0 \\ -S & I & 0 \\ -\boldsymbol{y}^T & 0 & I \end{bmatrix} \begin{Bmatrix} \partial \mathbf{F}_a / \partial \beta \\ \partial \boldsymbol{w} / \partial \beta \\ \partial M_b / \partial \beta \end{Bmatrix} = \begin{Bmatrix} \mathrm{q}\mathbf{C} \\ 0 \\ 0 \end{Bmatrix} \ . \tag{6.22}$$

Equation (6.22) is solved for the derivative of the root bending moment of the flexible wing with respect to the control deflection.

For the rigid wing, Eq.(6.22) is simplified since the terms depending on $\boldsymbol{w}$ will disappear from the formulation. This gives

$$\left(\frac{\partial M_b}{\partial \beta} \right)_{rigid} = q \boldsymbol{y}^T \mathbf{C} \ . \tag{6.23}$$

The control efficiency is defined by the ratio of the two derivatives of M_b obtained from Eqs.(6.22) and (6.23) as

$$CE = \frac{(\partial M_b/\partial\beta)}{(\partial M_b/\partial\beta)_{rigid}} \,. \tag{6.24}$$

To assure control effectiveness and avoid control reversal this ratio must be greater than zero.

6.4 Divergence Calculation

The aeroelastic divergence instability is calculated at a fixed angle of attack, and is characterized by a non-trivial solution to the homogeneous part of Eq.(6.17) as

$$\begin{bmatrix} I & -qA & -q\mathbf{C} \\ -S & I & 0 \\ 0 & -\mathbf{G}^T & I \end{bmatrix} \begin{Bmatrix} \partial\mathbf{F}_a/\partial\Delta\alpha_g \\ \partial\boldsymbol{w}/\partial\Delta\alpha_g \\ \partial\beta/\partial\Delta\alpha_g \end{Bmatrix} = \begin{Bmatrix} 0 \\ 0 \\ 0 \end{Bmatrix} \,. \tag{6.25}$$

This is an eigenvalue problem for q, with the lowest real eigenvalue representing the divergence dynamic pressure q_D. The corresponding eigenvector is denoted as $[\mathbf{F}_{a_D}, \boldsymbol{w}_D, \beta_D]^T$. Equation (6.25) can be reduced to a standard linear eigenvalue problem by substituting $\partial\boldsymbol{w}/\partial\Delta\alpha_g$ and $\partial\beta/\partial\Delta\alpha_g$ in terms of $\partial\mathbf{F}_a/\partial\Delta\alpha_g$ to obtain

$$\left[[A + \mathbf{C}\mathbf{G}^T]S - \frac{I}{q}\right] \left\{\frac{\partial\mathbf{F}_a}{\partial\Delta\alpha_g}\right\} = 0 \,, \tag{6.26}$$

with the largest real eigenvalue being $1/q_D$.

6.5 Aeroelastic Sensitivity Analysis at Maneuver

The method used in the aeroelastic calculation earlier can also be utilized in calculating the derivatives of the aeroelastic response with respect to each of the design variables. These derivatives are needed in the design problem, and can be calculated by differentiating Eqs.(6.9) to (6.11) with respect to each design variable.

This approach requires the calculation of derivatives of matrices A and S which can be very costly. Here, instead, the technique developed by Sobieski[41,42] is followed, and Eqs.(6.1), (6.2) and (6.5) are differentiated with respect to a design variable P to obtain

$$J\mathbf{X}' = \boldsymbol{f}' \,, \tag{6.27}$$

where a prime denotes partial differentiation with respect to P and where

$$\mathbf{X}' = \begin{Bmatrix} \mathbf{F}'_a \\ \alpha' \\ \boldsymbol{w}' \end{Bmatrix} \,, \tag{6.27.a}$$

$$\boldsymbol{f}' = \begin{Bmatrix} \boldsymbol{f}'_1 \\ \boldsymbol{f}'_2 \\ \boldsymbol{f}'_3 \end{Bmatrix} \,, \tag{6.27.b}$$

along with the definition $f'_i = \partial f_i / \partial P$ for $i = 1, 2, 3$. The Jacobian J appearing in Eq.(6.27) is the same as the one utilized in the analysis in Eq.(6.8). Equation (6.27) can be partially solved to yield

$$(I - qSA^*)\boldsymbol{w}' = SB\boldsymbol{f}'_1 + \frac{S\mathbf{R}}{\mathbf{N}^T\mathbf{R}} f'_2 + \boldsymbol{f}'_3 \,, \tag{6.28}$$

$$\alpha' = \frac{f'_2 - \mathbf{N}^T\boldsymbol{f}'_1 - q\mathbf{N}^TA\boldsymbol{w}'}{q\mathbf{N}^T\mathbf{R}} \,, \tag{6.29}$$

$$\mathbf{F}'_a = \boldsymbol{f}'_1 + q\mathbf{R}\alpha' + qA\boldsymbol{w}' \,. \tag{6.30}$$

This approach does not require any derivatives of A and S but only partial derivatives of $\boldsymbol{f}_1$, $\boldsymbol{f}_2$ and $\boldsymbol{f}_3$. For example, $\boldsymbol{f}'_1$ denotes the derivative of $\mathbf{F}_a$ with respect to a design variable when α and $\boldsymbol{w}$ are fixed.

Note that Eqs.(6.28) to (6.30) are based on the Jacobian J being calculated at the point where Eqs.(6.1), (6.2) and (6.5) are satisfied. Because the single Newton iteration satisfies these equations only approximately, the derivatives are also approximate.

6.6 Control Deflection Sensitivity Analysis

The design problem requires the derivatives of control deflection with respect to the design variables. To determine them, Eq.(6.14) must be differentiated with respect to each design variable P as

$$\frac{\partial \beta_a}{\partial P} = \frac{\partial}{\partial P}\left(\frac{\partial \beta}{\partial \Delta\alpha_g}\right)\Delta\alpha_g + \frac{\partial \beta}{\partial \Delta\alpha_g}\frac{\partial \Delta\alpha_g}{\partial P} \,. \tag{6.31}$$

The calculation of each term on the right hand side of Eq.(6.31) is explained in the following subsections.

6.6.1 $\partial(\partial\beta/\partial\Delta\alpha_g)/\partial P$ Calculation

The derivative of $\partial\beta/\partial\Delta\alpha_g$ with respect to each design variable is calculated by differentiating Eq.(6.18) as

$$\begin{bmatrix} 0 & -\partial(qA)/\partial P & -\partial(q\mathbf{C})/\partial P \\ -\partial S/\partial P & 0 & 0 \\ 0 & -\partial \mathbf{G}^T/\partial P & 0 \end{bmatrix} \begin{Bmatrix} \partial \mathbf{F}_a/\partial\Delta\alpha_g \\ \partial \boldsymbol{w}/\partial\Delta\alpha_g \\ \partial\beta/\partial\Delta\alpha_g \end{Bmatrix} +$$

$$\begin{bmatrix} I & -qA & -q\mathbf{C} \\ -S & I & 0 \\ 0 & -\mathbf{G}^T & I \end{bmatrix} \begin{Bmatrix} \partial(\partial \mathbf{F}_a/\partial\Delta\alpha_g)/\partial P \\ \partial(\partial \boldsymbol{w}/\partial\Delta\alpha_g)/\partial P \\ \partial(\partial\beta/\partial\Delta\alpha_g)/\partial P \end{Bmatrix} = \begin{Bmatrix} \partial(q\mathbf{R})/\partial P \\ 0 \\ 0 \end{Bmatrix} , \tag{6.32}$$

where

$$\frac{\partial A}{\partial P} = A' + \frac{\partial A}{\partial \alpha_r}\frac{\partial \alpha_r}{\partial P} \,, \tag{6.32.a}$$

$$\frac{\partial \mathbf{C}}{\partial P} = \mathbf{C}' + \frac{\partial \mathbf{C}}{\partial \alpha_r}\frac{\partial \alpha_r}{\partial P} \,, \tag{6.32.b}$$

$$\frac{\partial S}{\partial P} = S' \,, \tag{6.32.c}$$

$$\frac{\partial \mathbf{G}^T}{\partial P} = (\mathbf{G}^T)' \,, \tag{6.32.d}$$

$$\frac{\partial \mathbf{R}}{\partial P} = \mathbf{R}' \,, \tag{6.32.e}$$

$$\frac{\partial \alpha_r}{\partial P} = \frac{\partial \alpha_r}{\partial W}\frac{\partial W}{\partial P} + \frac{\partial \alpha_r}{\partial \boldsymbol{f}_1}\frac{\partial \boldsymbol{f}_1}{\partial P} + \frac{\partial \alpha_r}{\partial \mathbf{R}}\frac{\partial \mathbf{R}}{\partial P} \,, \tag{6.32.f}$$

where for example, A' denotes the derivative of A with respect to a design variable holding α, $\boldsymbol{w}$ and β fixed. A and $\mathbf{C}$ are evaluated at rigid wing conditions with dependency on both rigid angle of attack α_r and design variable vector $\mathbf{P}$. S, $\mathbf{G}^T$ and $\mathbf{R}$ depend only on the design variable vector $\mathbf{P}$. Equations (6.32) can be reworked to get the equations for the second derivatives of $\mathbf{F}_a$, $\boldsymbol{w}$ and β as

$$\frac{\partial}{\partial P}\left(\frac{\partial \mathbf{F}_a}{\partial \Delta\alpha_g}\right) = q[I - qAS - q\mathbf{C}\mathbf{G}^T S]^{-1} \left[\mathbf{R}' + A'\frac{\partial \boldsymbol{w}}{\partial \Delta\alpha_g} + \left(\frac{\partial A}{\partial \alpha_r}\frac{\partial \alpha_r}{\partial P}\right)\frac{\partial \boldsymbol{w}}{\partial \Delta\alpha_g} + \mathbf{C}'\frac{\partial \beta}{\partial \Delta\alpha_g} + \left(\frac{\partial \mathbf{C}}{\partial \alpha_r}\frac{\partial \alpha_r}{\partial P}\right)\frac{\partial \beta}{\partial \Delta\alpha_g} + \mathbf{C}(\mathbf{G}^T)'\frac{\partial \boldsymbol{w}}{\partial \Delta\alpha_g} + [A + \mathbf{C}\mathbf{G}^T]S'\frac{\partial \mathbf{F}_a}{\partial \Delta\alpha_g}\right], \tag{6.33}$$

$$\frac{\partial}{\partial P}\left(\frac{\partial \boldsymbol{w}}{\partial \Delta\alpha_g}\right) = S'\frac{\partial \mathbf{F}_a}{\partial \Delta\alpha_g} + S\frac{\partial}{\partial P}\left(\frac{\partial \mathbf{F}_a}{\partial \Delta\alpha_g}\right), \tag{6.34}$$

$$\frac{\partial}{\partial P}\left(\frac{\partial \beta}{\partial \Delta\alpha_g}\right) = (\mathbf{G}^T)'\frac{\partial \boldsymbol{w}}{\partial \Delta\alpha_g} + \mathbf{G}^T\frac{\partial}{\partial P}\left(\frac{\partial \mathbf{F}_a}{\partial \Delta\alpha_g}\right). \tag{6.35}$$

Equations (6.33) to (6.35) contain the derivatives of A and S matrices with respect to P, which were avoided before. However, by utilizing the technique discussed by Grossman et al.[60] the terms containing A' and S' can be calculated without determining either of these derivatives explicitly. Using the definition of A in Eq.(6.8.c), it is noted that

$$qA'\left(\frac{\partial \boldsymbol{w}}{\partial \Delta\alpha_g}\right) = \frac{\partial}{\partial P}\left(\frac{\partial \boldsymbol{f}_1}{\partial \boldsymbol{w}}\right)\frac{\partial \boldsymbol{w}}{\partial \Delta\alpha_g}. \tag{6.36}$$

To see how $qA'(\partial \boldsymbol{w}/\partial \Delta\alpha_g)$ can be calculated without calculating A', a more generic case is considered. Let f be a function of vector $\mathbf{Z}$, and let $\mathbf{Q}$ be a given unit vector. Let $\mathbf{Z}_0$ be a particular choice for $\mathbf{Z}$, then the scalar product of the gradient $\partial f/\partial \mathbf{Z}$ at $\mathbf{Z}_0$ and the vector $\mathbf{Q}$ is the directional derivative of f in the direction $\mathbf{Q}$, that is

$$\begin{aligned}\left(\frac{\partial f}{\partial \mathbf{Z}}\right)_{\mathbf{Z}_0}\mathbf{Q} &= \lim_{\epsilon \to 0}\frac{1}{\epsilon}[f(\mathbf{Z}_0 + \epsilon\mathbf{Q}) - f(\mathbf{Z}_0)] \\ &= \frac{d}{d\epsilon}[f(\mathbf{Z}_0 + \epsilon\mathbf{Q})]_{\epsilon=0}.\end{aligned} \tag{6.37}$$

Equation (6.37) holds even if $\mathbf{Q}$ is not a unit vector, but has an arbitrary magnitude. Equation (6.37) provides a way of calculating the product $\partial f/\partial \mathbf{Z}$ times $\mathbf{Q}$ without calculating the individual components of $\partial f/\partial \mathbf{Z}$. Now considering Eq.(6.36) and using $\boldsymbol{w}$ as the vector $\mathbf{Z}$ and $\partial \boldsymbol{w}/\partial \Delta\alpha_g$ as the vector $\mathbf{Q}$ yields

$$\left(\frac{\partial f_{1_i}}{\partial \boldsymbol{w}}\right)\frac{\partial \boldsymbol{w}}{\partial \Delta\alpha_g} = \frac{d}{d\epsilon}\left[f_{1_i}(\boldsymbol{w}_0 + \frac{\partial \boldsymbol{w}}{\partial \Delta\alpha_g}\epsilon)\right]_{\epsilon=0}, \qquad \text{for } i = 1,\ldots,n_l\,, \tag{6.38}$$

where f_{1_i} is a component of $\boldsymbol{f}_1$ and $\boldsymbol{w}_0$ is the value of vector $\boldsymbol{w}$ at which the A matrix is calculated. Here, $\boldsymbol{w}_0$ is zero. Note that $\partial f_{1_i}/\partial \boldsymbol{w}$ is a row vector with elements composed of the derivatives of f_{1_i} with respect to the individual components of $\boldsymbol{w}$. Equation (6.38) can also be written as

$$\left(\frac{\partial \boldsymbol{f}_1}{\partial \boldsymbol{w}}\right)\frac{\partial \boldsymbol{w}}{\partial \Delta\alpha_g} = \frac{d}{d\epsilon}\left[\boldsymbol{f}_1(\frac{\partial \boldsymbol{w}}{\partial \Delta\alpha_g}\epsilon)\right]_{\epsilon=0}, \tag{6.39}$$

where $\boldsymbol{f}_1$ is a nonlinear function of $\boldsymbol{w}$. Here the right hand side of Eq.(6.39) is calculated by finite-differences as

$$\left(\frac{\partial \boldsymbol{f}_1}{\partial \boldsymbol{w}}\right)\frac{\partial \boldsymbol{w}}{\partial \Delta\alpha_g} = \frac{\boldsymbol{f}_1(\mathbf{P}, \alpha_r, (\partial \boldsymbol{w}/\partial \Delta\alpha_g)\epsilon, 0) - \boldsymbol{f}_1(\mathbf{P}, \alpha_r, 0, 0)}{\epsilon}\,. \tag{6.40}$$

For Eq.(6.36) the derivative of $(\partial \boldsymbol{f}_1/\partial \boldsymbol{w})\partial \boldsymbol{w}/\partial \Delta\alpha_g$ with respect to P holding $\partial \boldsymbol{w}/\partial \Delta\alpha_g$ fixed (because the derivative with respect to P in Eq.(6.36) applies only to the aerodynamic coefficient matrix A) must be calculated. Using the forward finite-difference scheme, it gives

$$qA'\left(\frac{\partial \boldsymbol{w}}{\partial \Delta\alpha_g}\right) = \frac{\left[(\partial \boldsymbol{f}_1/\partial \boldsymbol{w})\partial \boldsymbol{w}/\partial \Delta\alpha_g\right]_{P+\Delta P} - \left[(\partial \boldsymbol{f}_1/\partial \boldsymbol{w})\partial \boldsymbol{w}/\partial \Delta\alpha_g\right]_{P}}{\Delta P}\,. \tag{6.41}$$

Since the aerodynamic force vector is only a function of the wing shape and dynamic pressure design variables (i.e., P_1 to P_9), the solution of Eq.(6.41) requires 20 calculations of the force vector $\boldsymbol{f}_1$. Equation (6.40) is calculated once for P and

once for $P+\Delta P$ (for P_1 to P_9) with each requiring two $\boldsymbol{f}_1$ calculations. By contrast, the calculation of A' requires the perturbation of n_l aerodynamic solutions which translates into $10 \times 48 = 480$ force vector calculations.

The derivative in the right hand side of Eq.(6.40) was determined for various values of ϵ, but did not show a strong sensitivity to the value of stepsize; hence ϵ was chosen to be 1°. The non-zero derivatives (i.e., those with respect to P_1 to P_9) found from Eq.(6.41), however, showed some variations with the stepsize ΔP. Hence, to select the best stepsize for the finite-difference calculations, the normalized (logarithmic) derivative in Eq.(6.41) was calculated for several values of stepsize (i.e., $\Delta P = 1 \times 10^{-5}$ to $\Delta P = 1 \times 10^{-1}$ in increments of 10). The stepsize selected was $\Delta P = 1 \times 10^{-4}$, since it was contained in the region where the derivative showed the least amount of variation with the stepsize.

To calculate the product $S'(\partial \mathbf{F}_a / \partial \Delta\alpha_g)$, a similar procedure is used, noting that

$$S' \frac{\partial \mathbf{F}_a}{\partial \Delta\alpha_g} = \frac{\partial}{\partial P}\left(\frac{\partial \boldsymbol{f}_3}{\partial \mathbf{F}_a}\right)\frac{\partial \mathbf{F}_a}{\partial \Delta\alpha_g} , \tag{6.42}$$

and

$$\left(\frac{\partial \boldsymbol{f}_3}{\partial \mathbf{F}_a}\right)\frac{\partial \mathbf{F}_a}{\partial \Delta\alpha_g} = \frac{d}{d\epsilon}\left[\boldsymbol{f}_3(\mathbf{F}_{a_0} + \frac{\partial \mathbf{F}_a}{\partial \Delta\alpha_g}\epsilon)\right]_{\epsilon=0} , \tag{6.43}$$

where $\mathbf{F}_{a_0}$ is the nominal value of $\mathbf{F}_a$. By examining Eqs.(6.3) to (6.5), it is apparent that $\boldsymbol{f}_3$ is a linear function of $\mathbf{F}_a$, and the right hand side of Eq.(6.43) can be calculated by solving

$$K\mathbf{U}_g = T\frac{\partial \mathbf{F}_a}{\partial \Delta\alpha_g} , \tag{6.44}$$

$$\frac{d}{d\epsilon}\left[\boldsymbol{f}_3(\mathbf{F}_{a_0} + \frac{\partial \mathbf{F}_a}{\partial \Delta\alpha_g}\epsilon)\right]_{\epsilon=0} = T^T\mathbf{U}_g , \tag{6.45}$$

where $\mathbf{U}_g$ is the gust-induced finite-element nodal displacement vector. For Eq.(6.42), the derivative of $(\partial \boldsymbol{f}_3/\partial \mathbf{F}_a)\partial \mathbf{F}_a/\partial \Delta\alpha_g$ with respect to P holding $\partial \mathbf{F}_a/\partial \Delta\alpha_g$ fixed

(because the derivative with respect to P in Eq.(6.42) applies only to the flexibility matrix S) must be calculated. Realizing that the right hand side of Eq.(6.45) is equal to the displacement vector at the load set $\boldsymbol{w}_g$ due to $\partial \mathbf{F}_a / \partial \Delta\alpha_g$, the right hand side of Eq.(6.42) is determined by calculating the derivative of a single displacement solution. However, the derivative of $\boldsymbol{w}_g$ with respect to P is not $\boldsymbol{w}'_g$ since $\partial \mathbf{F}_a / \partial \Delta\alpha_g$ is kept fixed.

Using the forward finite-difference scheme, $S'(\partial \mathbf{F}_a / \partial \Delta\alpha_g)$ is calculated as

$$S' \frac{\partial \mathbf{F}_a}{\partial \Delta\alpha_g} = \frac{(\boldsymbol{w}_g)_{P+\Delta P} - (\boldsymbol{w}_g)_P}{\Delta P} \,. \tag{6.46}$$

The stepsize here was chosen similarly to the previous case by calculating the logarithmic derivative $(\Delta \boldsymbol{w}/\boldsymbol{w})/(\Delta P/P)$ for several values of ΔP among which $\Delta P = 1 \times 10^{-3}$ was found to be the best for the non-zero derivatives (i.e., all except P_9 to P_{12}).

The non-zero derivatives (i.e., those with respect to P_1 to P_9) in $\mathbf{R}'$, $\mathbf{C}'$ are evaluated using a forward finite-difference scheme with a stepsize of $\Delta P = 1 \times 10^{-4}$, $\Delta P = 1 \times 10^{-5}$, respectively. The non-zero derivatives (i.e., all except P_{11} and P_{12}) in $\partial \alpha_r / \partial P$ are also evaluated using forward finite-differences with a stepsize of $\Delta P = 1 \times 10^{-4}$. Here again the stepsizes were chosen by calculating the logarithmic derivatives in each case for several value of the stepsize.

The derivatives $\partial \mathbf{C} / \partial \alpha_r$ and $\partial A / \partial \Delta\alpha_g$ were also calculated by finite-differences with a stepsize of 1° for each. These derivatives did not show any considerable variation with the stepsize.

The derivatives of $\mathbf{G}^T$ with respect to $\mathbf{P}$ were calculated analytically by differentiating Eq.(5.9). $\mathbf{G}^T$ is a row vector with only 4 (out of 48) non-zero terms. The

derivatives of these non-zero terms are

$$\frac{\partial G_{13}}{\partial P_2} = -\frac{P_{11}}{P_2^2} , \tag{6.47.a}$$

$$\frac{\partial G_{18}}{\partial P_2} = \frac{P_{11}}{P_2^2} , \tag{6.47.b}$$

$$\frac{\partial G_{43}}{\partial P_3} = -\frac{P_{12}}{P_3^2} , \tag{6.47.c}$$

$$\frac{\partial G_{48}}{\partial P_3} = \frac{P_{12}}{P_3^2} , \tag{6.47.d}$$

$$\frac{\partial G_{13}}{\partial P_{11}} = \frac{1}{P_2} , \tag{6.47.e}$$

$$\frac{\partial G_{18}}{\partial P_{11}} = -\frac{1}{P_2} , \tag{6.47.f}$$

$$\frac{\partial G_{43}}{\partial P_{12}} = \frac{1}{P_3} , \tag{6.47.g}$$

$$\frac{\partial G_{48}}{\partial P_{12}} = -\frac{1}{P_3} , \tag{6.47.h}$$

where P_{11} and P_{12} are the gain design variables, and P_2 and P_3 are the break and tip chord design variables, respectively.

Having calculated all the necessary terms in Eqs.(6.33) to (6.35), the second derivatives, $\partial(\partial\beta/\partial\Delta\alpha_g)/\partial P$ can now be determined.

6.6.2 $\partial\Delta\alpha_g/\partial P$ Calculation

By examining Eq.(4.23), it is noted that the gust-induced angle of attack increment $\Delta\alpha_g$ is a function of vertical gust speed which is determined from Eq.(4.21) for a given cruise altitude. Since the cruise altitude is determined from cruise dynamic pressure ($q_c = P_9$), $\Delta\alpha_g$ is then an implicit function of P_9. Hence, the only non-zero derivative of $\Delta\alpha_g$ is that with respect to P_9, and is determined numerically as

$$\frac{\partial\Delta\alpha_g}{\partial P_9} = \frac{(\Delta\alpha_g)_{P_9+\Delta P_9} - (\Delta\alpha_g)_{P_9}}{\Delta P_9} . \tag{6.48}$$

The stepsize chosen for this derivative was 1×10^{-3}.

6.7 Control Efficiency Sensitivity Analysis

The derivatives of the control efficiency CE with respect to the design variables $\mathbf{P}$ are needed in the design problem, and are determined by calculating the derivatives of $\partial M_b/\partial\beta$ with respect to $\mathbf{P}$ for both flexible and rigid wings.

6.7.1 $\partial(\partial M_b/\partial\beta)/\partial P$ Calculation for Flexible Wing

To determine the derivatives of $\partial M_b/\partial\beta$ with respect to each of the design variables, Eq.(6.22) is differentiated with respect to P as

$$\begin{bmatrix} 0 & -\partial(qA)/\partial P & 0 \\ -\partial S/\partial P & 0 & 0 \\ -\partial \boldsymbol{y}^T/\partial P & 0 & 0 \end{bmatrix} \begin{Bmatrix} \partial \mathbf{F}_a/\partial\beta \\ \partial \boldsymbol{w}/\partial\beta \\ \partial M_b/\partial\beta \end{Bmatrix} +$$

$$\begin{bmatrix} I & -qA & 0 \\ -S & I & 0 \\ -\boldsymbol{y}^T & 0 & I \end{bmatrix} \begin{Bmatrix} \partial(\partial \mathbf{F}_a/\partial\beta)/\partial P \\ \partial(\partial \boldsymbol{w}/\partial\beta)/\partial P \\ \partial(\partial M_b/\partial\beta)/\partial P \end{Bmatrix} = \begin{Bmatrix} \partial(q\mathbf{C})/\partial P \\ 0 \\ 0 \end{Bmatrix} , \tag{6.49}$$

where

$$\frac{\partial \boldsymbol{y}^T}{\partial P} = (\boldsymbol{y}^T)' , \tag{6.49.a}$$

and the other first order derivatives in Eq.(6.49) are the same as those defined previously in subsection(6.6.1). Equation (6.49) can be rearranged to get the equations for the second order derivatives of $\mathbf{F}_a$, $\boldsymbol{w}$ and M_b as

$$\frac{\partial}{\partial P}\left(\frac{\partial \mathbf{F}_a}{\partial\beta}\right) = q[I - qAS]^{-1} \left[A'\frac{\partial \boldsymbol{w}}{\partial\beta} + \left(\frac{\partial A}{\partial\alpha_r}\frac{\partial\alpha_r}{\partial P}\right)\frac{\partial \boldsymbol{w}}{\partial\beta} + \mathbf{C}' + \frac{\partial \mathbf{C}}{\partial\alpha_r}\frac{\partial\alpha_r}{\partial P} + [AS']\frac{\partial \mathbf{F}_a}{\partial\beta}\right] , \tag{6.50}$$

$$\frac{\partial}{\partial P}\left(\frac{\partial \boldsymbol{w}}{\partial\beta}\right) = S'\frac{\partial \mathbf{F}_a}{\partial\beta} + S\frac{\partial}{\partial P}\left(\frac{\partial \mathbf{F}_a}{\partial\beta}\right) , \tag{6.51}$$

$$\frac{\partial}{\partial P}\left(\frac{\partial M_b}{\partial\beta}\right) = (\boldsymbol{y}^T)'\frac{\partial \mathbf{F}_a}{\partial\beta} + \boldsymbol{y}^T\frac{\partial}{\partial P}\left(\frac{\partial \mathbf{F}_a}{\partial\beta}\right) . \tag{6.52}$$

The terms involving A' and S' are calculated by following the same procedure as before.

The term $qA'(\partial \boldsymbol{w}/\partial\beta)$ can be expressed as

$$qA'\left(\frac{\partial \boldsymbol{w}}{\partial\beta}\right) = \frac{\partial}{\partial P}\left(\frac{\partial \boldsymbol{f}_1}{\partial \boldsymbol{w}}\right)\frac{\partial \boldsymbol{w}}{\partial\beta}\ , \tag{6.53}$$

where

$$\left(\frac{\partial \boldsymbol{f}_1}{\partial \boldsymbol{w}}\right)\frac{\partial \boldsymbol{w}}{\partial\beta} = \frac{d}{d\epsilon}\left[\boldsymbol{f}_1(\boldsymbol{w}_0 + \frac{\partial \boldsymbol{w}}{\partial\beta}\epsilon)\right]_{\epsilon=0}\ . \tag{6.54}$$

Using the finite-difference approach to calculate the right hand side in Eq.(6.54) gives

$$\left(\frac{\partial \boldsymbol{f}_1}{\partial \boldsymbol{w}}\right)\frac{\partial \boldsymbol{w}}{\partial\beta} = \frac{\boldsymbol{f}_1(\mathbf{P}, \alpha_r, (\partial \boldsymbol{w}/\partial\beta)\epsilon, 0) - \boldsymbol{f}_1(\mathbf{P}, \alpha_r, 0, 0)}{\epsilon}\ . \tag{6.55}$$

Equation (6.55) is evaluated nine different times (for P_1 to P_9) while holding $\partial \boldsymbol{w}/\partial\beta$ fixed. Hence, the derivative in Eq.(6.53) is determined as

$$qA'\left(\frac{\partial \boldsymbol{w}}{\partial\beta}\right) = \frac{\left[(\partial \boldsymbol{f}_1/\partial \boldsymbol{w})\partial \boldsymbol{w}/\partial\beta\right]_{P+\Delta P} - \left[(\partial \boldsymbol{f}_1/\partial \boldsymbol{w})\partial \boldsymbol{w}/\partial\beta\right]_{P}}{\Delta P}\ . \tag{6.56}$$

The best stepsizes for Eqs.(6.55) and (6.56) were found to be $\epsilon = 1°$ and $\Delta P = 1 \times 10^{-4}$, respectively by examining the logarithmic derivatives in each case the same way as before.

To calculate the product $S'(\partial \mathbf{F}_a/\partial\beta)$, a similar procedure is used, noting that

$$S'\frac{\partial \mathbf{F}_a}{\partial\beta} = \frac{\partial}{\partial P}\left(\frac{\partial \boldsymbol{f}_3}{\partial \mathbf{F}_a}\right)\frac{\partial \mathbf{F}_a}{\partial\beta}\ , \tag{6.57}$$

and

$$\left(\frac{\partial \boldsymbol{f}_3}{\partial \mathbf{F}_a}\right)\frac{\partial \mathbf{F}_a}{\partial\beta} = \frac{d}{d\epsilon}\left[\boldsymbol{f}_3(\mathbf{F}_{a_0} + \frac{\partial \mathbf{F}_a}{\partial\beta}\epsilon)\right]_{\epsilon=0} = \boldsymbol{w}_\beta\ . \tag{6.58}$$

Following the same procedure as before, the derivatives in Eq.(6.57) are calculated as

$$S'\frac{\partial \mathbf{F}_a}{\partial\beta} = \frac{(\boldsymbol{w}_\beta)_{P+\Delta P} - (\boldsymbol{w}_\beta)_P}{\Delta P}\ . \tag{6.59}$$

The stepsize for ΔP was found to be 1×10^{-3}.

The derivatives of the vector of load-set spanwise coordinates $\boldsymbol{y}^T$ were calculated only for the shape design variables as

$$(\boldsymbol{y}^T)' = \frac{(\boldsymbol{y}^T)_{P+\Delta P} - (\boldsymbol{y}^T)_P}{\Delta P} \ . \tag{6.60}$$

6.7.2 $\partial(\partial M_b/\partial\beta)/\partial P$ Calculation for Rigid Wing

To determine the derivatives of $(\partial M_b/\partial\beta)_{rigid}$ with respect to each of the design variables, Eq.(6.23) is differentiated with respect to P as

$$\frac{\partial}{\partial P}\left(\frac{\partial M_b}{\partial \beta}\right)_{rigid} = q(\boldsymbol{y}^T)'\mathbf{C} + q\boldsymbol{y}^T\left(\mathbf{C}' + \frac{\partial \mathbf{C}}{\partial \alpha_r}\frac{\partial \alpha_r}{\partial P}\right) . \tag{6.61}$$

With all the terms on the right hand side of Eq.(6.61) already calculated, the derivatives of $(\partial M_b/\partial\beta)_{rigid}$ with respect to P can be determined.

6.8 Divergence Sensitivity Analysis

To determine the derivatives of divergence dynamic pressure q_D with respect to each of the design variables, Eq.(6.25) is differentiated at $q = q_D$ with respect to P as

$$\begin{bmatrix} 0 & -\partial(q_D A)/\partial P & -\partial(q_D \mathbf{C})/\partial P \\ -\partial S/\partial P & 0 & 0 \\ 0 & -\partial \mathbf{G}^T/\partial P & 0 \end{bmatrix} \begin{Bmatrix} \mathbf{F}_{a_D} \\ \boldsymbol{w}_D \\ \beta_D \end{Bmatrix} + \begin{bmatrix} I & -q_D A & -q_D \mathbf{C} \\ -S & I & 0 \\ 0 & -\mathbf{G}^T & I \end{bmatrix} \begin{Bmatrix} \partial \mathbf{F}_{a_D}/\partial P \\ \partial \boldsymbol{w}_D/\partial P \\ \partial \beta/\partial P \end{Bmatrix} = \begin{Bmatrix} 0 \\ 0 \\ 0 \end{Bmatrix} . \tag{6.62}$$

Premultiplying Eq.(6.62) by the left eigenvector of Eq.(6.25) $[\mathbf{F}_{a_L}^T, \boldsymbol{w}_L^T, \beta_L]$, defined by

$$[\mathbf{F}_{a_L}^T \quad \boldsymbol{w}_L^T \quad \beta_L] \begin{bmatrix} I & -q_D A & -q_D \mathbf{C} \\ -S & I & 0 \\ 0 & -\mathbf{G}^T & I \end{bmatrix} = 0 \tag{6.63}$$

gives

$$[\mathbf{F}_{a_L}^T \quad \boldsymbol{w}_L^T \quad \beta_L] \begin{bmatrix} 0 & -\partial(q_D A)/\partial P & -\partial(q_D \mathbf{C})/\partial P \\ -\partial S/\partial P & 0 & 0 \\ 0 & -\partial \mathbf{G}^T/\partial P & 0 \end{bmatrix} \begin{Bmatrix} \mathbf{F}_{a_D} \\ \boldsymbol{w}_D \\ \beta_D \end{Bmatrix} = 0 \,, \tag{6.64}$$

or

$$\frac{\partial q_D}{\partial P} = -\frac{q_D \mathbf{F}_{a_L}^T A' \boldsymbol{w}_D + \boldsymbol{w}_L^T S' \mathbf{F}_{a_D} + \beta_L (\mathbf{G}^T)' \boldsymbol{w}_D + q_D \mathbf{F}_{a_L}^T \mathbf{C}' \beta_D}{\mathbf{F}_{a_L}^T A \boldsymbol{w}_D + \mathbf{F}_{a_L}^T \mathbf{C} \beta_D} \,. \tag{6.65}$$

Here also the derivatives of A and S matrices appear. The method of calculation of the terms involving A' and S' is identical to that discussed previously for the other sensitivity calculation.

The term $q_D A' \boldsymbol{w}_D$ may be expressed as

$$q_D A' \boldsymbol{w}_D = \frac{\partial}{\partial P} \left(\frac{\partial \boldsymbol{f}_1}{\partial \boldsymbol{w}} \right) \boldsymbol{w}_D \,, \tag{6.66}$$

where

$$\begin{aligned} \left(\frac{\partial \boldsymbol{f}_1}{\partial \boldsymbol{w}} \right) \boldsymbol{w}_D &= \frac{d}{d\epsilon} \Big[\boldsymbol{f}_1 (\boldsymbol{w}_0 + \epsilon \boldsymbol{w}_D) \Big]_{\epsilon=0} \\ &= \frac{\boldsymbol{f}_1(\mathbf{P}, \alpha_r, \boldsymbol{w}_D, 0) - \boldsymbol{f}_1(\mathbf{P}, \alpha_r, 0, 0)}{\epsilon} \,. \end{aligned} \tag{6.67}$$

The term $q_D \; A' \boldsymbol{w}_D$ is determined as

$$q_D \; A' \boldsymbol{w}_D = \frac{\Big[(\partial \boldsymbol{f}_1 / \partial \boldsymbol{w}) \boldsymbol{w}_D \Big]_{P+\Delta P} - \Big[(\partial \boldsymbol{f}_1 / \partial \boldsymbol{w}) \boldsymbol{w}_D \Big]_P}{\Delta P} \,. \tag{6.68}$$

For this calculation, the best stepsizes were found to be $\epsilon = 10$ and $\Delta P = 1 \times 10^{-2}$.

The term $S' \mathbf{F}_{a_D}$ similarly to previous cases may be expressed as

$$S' \mathbf{F}_{a_D} = \frac{\partial}{\partial P} \left(\frac{\partial \boldsymbol{f}_3}{\partial \mathbf{F}_a} \right) \frac{\partial \mathbf{F}_a}{\partial \beta} \,, \tag{6.69}$$

where

$$\left(\frac{\partial \boldsymbol{f}_3}{\partial \mathbf{F}_a}\right)\mathbf{F}_{a_D} = \frac{d}{d\epsilon}\left[\boldsymbol{f}_3(\mathbf{F}_{a_0} + \epsilon \mathbf{F}_{a_D}\right]_{\epsilon=0} = \boldsymbol{w}_D \ . \tag{6.70}$$

Following the same procedure as before, the derivatives in Eq.(6.69) are calculated as

$$S'\mathbf{F}_{a_D} = \frac{(\boldsymbol{w}_D)_{P+\Delta P} - (\boldsymbol{w}_D)_P}{\Delta P} \ . \tag{6.71}$$

the best stepsize was found to be $\Delta P = 1 \times 10^{-3}$.

For the term $q_D \mathbf{C}' \beta_D$ a direct finite difference for $\mathbf{C}'$ was used. This calculation, similar to $\mathbf{R}'$ calculation, is not as expensive as that for A' or S', thus there is no need for modular approach. The best stepsize for the non-zero terms in $\mathbf{C}'$ (i.e., for P_1 to P_9) was found to be $\Delta P = 1 \times 10^{-3}$.

7. APPROXIMATE OPTIMIZATION PROCEDURE AND RESULTS

Having defined the design problem along with the associated variables and constraints previously in chapter 4, the optimization problem can now be formulated and solved. The forward-swept wing optimization problem with gross weight W as the objective function is formulated as to find the design variable vector $\mathbf{P}$ which

$$
\begin{aligned}
\text{minimizes} \quad & W(\mathbf{P}) \,, \\
\text{subject to} \quad & \mathbf{g}_s \geq 0 \,, \\
& q_D(\mathbf{P}) \geq 1.44 q_m(\mathbf{P}) \,, \\
& R(\mathbf{P}, D) \geq R_r \,, \\
& \vartheta(\mathbf{P}) \geq \vartheta_{fr} \,, \\
& V_L(\mathbf{P}, W) \leq V_{Lr} \,, \\
& C_{L_{out}}(\mathbf{P}) \leq 1.0 \,, \\
& -10^\circ \leq \beta_a(\mathbf{P}) \leq 10^\circ \,, \\
& CE(\mathbf{P}) \geq 0.5 \,, \\
& P_5 \geq 0.6(P_4 + P_5) \,, \\
& P_6 \geq 20^\circ \,, \\
& -4^\circ \leq P_7 \leq 4^\circ \,, \\
& -4^\circ \leq P_8 \leq 4^\circ \,,
\end{aligned}
\tag{7.1}
$$

where the vector $\mathbf{g}_s$ represents the structural constraints on stresses and strains, q_D and q_m are the divergence and maneuver dynamic pressures, respectively. The calculated and required range are represented by R and R_r, respectively. The quantities ϑ and ϑ_{fr} represent the available wing and required fuel volume, respectively.

The outboard-section lift coefficient is denoted by $C_{L_{out}}$. The approximate value of the control deflection is represented by β_a, and the control efficiency is denoted by CE. The outboard span P_5 and leading-edge sweep angle at the break P_6 have only lower bounds imposed on them, while the two twist design variables P_7 and P_8 are confined by both lower and upper bounds.

The solution of an optimization problem usually requires many calculations of the objective function, constraints, and their derivatives which are used for calculating search directions. In problems where these calculations are very involved and time consuming, various techniques may be applied to reduce the computational cost. One such technique is the sequential approximate optimization[67] which uses the linear approximation of the objective function and constraints based on the initial set of design variables $\mathbf{P}^0$ and the derivative information at the initial design to determine an approximate solution to the optimization problem defined by the design variable vector $\mathbf{P}^L$. Move limits are imposed on the design variables to assure a certain degree of accuracy necessary in the approximation. The approximate solution defined by the design variable vector $\mathbf{P}^L$ may still be far away from a local optima. To obtain the optimum design or to get as close to it as possible, the approximate solution defined by $\mathbf{P}^L$ will be used as the initial design for the next iteration (cycle). This process may continue for many iterations before convergence is reached.

Since the forward-swept wing problem involves many elaborate and costly analysis calculations, it is naturally a good candidate for the application of the sequential approximate optimization. Each approximate optimization problem may be

formulated as

$$
\begin{aligned}
\text{minimize} \quad & W(\mathbf{P}) \ , \\
\text{subject to} \quad & \mathbf{g}_s(\mathbf{P}) = \mathbf{g}_s(\mathbf{P}^0) + \sum_{i=1}^{N_{DV}} \left(\frac{\partial \mathbf{g}_s}{\partial P_i} \right)_{\mathbf{P}^0} \Delta P_i \geq 0 \ , \\
& q_D(\mathbf{P}) = q_D(\mathbf{P}^0) + \sum_{i=1}^{N_{DV}} \left(\frac{\partial q_D}{\partial P_i} \right)_{\mathbf{P}^0} \Delta P_i \geq 1.44 q_m(\mathbf{P}) \ , \\
& R(\mathbf{P}, D) \geq R_r \ , \\
& \vartheta(\mathbf{P}) \geq \vartheta_{fr} \ , \\
& V_L(\mathbf{P}, W) \leq V_{Lr} \ , \\
& C_{L_{out}}(\mathbf{P}) \leq 1.0 \ , \\
& -10^\circ \leq \beta_a(\mathbf{P}) = \beta_a(\mathbf{P}^0) + \sum_{i=1}^{N_{DV}} \left(\frac{\partial \beta_a}{\partial P_i} \right)_{\mathbf{P}^0} \Delta P_i \leq 10^\circ \ , \\
& CE(\mathbf{P}) \geq 0.5 \ , \\
& P_5 \geq 0.6(P_4 + P_5) \ , \\
& P_6 \geq 20^\circ \ , \\
& -4^\circ \leq P_7 \leq 4^\circ \ , \\
& -4^\circ \leq P_8 \leq 4^\circ \ .
\end{aligned}
\tag{7.2}
$$

Recalling from chapter 4, the gross weight is given in terms of the aircraft standard empty weight W_s, usable fuel weight W_{uf} and the payload weight W_p as

$$W = W_s + W_{uf} + W_p \ , \tag{4.1}$$

where

$$W_s = W_{rs} - \eta(W_{rw} - W_w) \ , \tag{4.2}$$

with W_{rs} representing the standard empty weight of the reference aircraft and W_w and W_{rw} representing the structural wing weight of the design and reference

aircraft, respectively. Here, the objective function is calculated exactly from a linear approximation to the wing structural weight as

$$W_w(\mathbf{P}) = W_w(\mathbf{P}^0) + \sum_{i=1}^{N_{DV}} \left(\frac{\partial W_w}{\partial P_i}\right)_{\mathbf{P}^0} \Delta P_i \ . \tag{7.3}$$

The derivatives of wing structural weight with respect to structural design variables (P_{13} to P_{48}) in Eq.(7.3) are determined by WIDOWAC while the derivatives with respect to the other design variables are determined by finite-differences with $\Delta P = 1 \times 10^{-2}$.

The derivatives of the structural constraints $\partial \mathbf{g}_s / \partial P_i$ are evaluated by finite-differences with $\Delta P = 1 \times 10^{-2}$ for P_1 to P_8 and $\Delta P = 1 \times 10^{-3}$ for the rest. The derivatives of the divergence dynamic pressure $q_D{}'$ are determined from Eq.(6.65).

The range R is calculated exactly at $q = q_c$ from a linear approximation to the total drag given by

$$D(\mathbf{P}) = D(\mathbf{P}^0) + \sum_{i=1}^{N_{DV}} \left(\frac{\partial D}{\partial P_i}\right)_{\mathbf{P}^0} \Delta P_i \ , \tag{7.4}$$

where the derivatives of drag with respect to design variables are determined at cruise condition as

$$\frac{\partial D}{\partial P_i} = D' + \frac{\partial D}{\partial \alpha} \alpha' \ , \tag{7.5}$$

where $'$ denotes differentiation with respect to P_i holding α and $\boldsymbol{w}$ fixed. Here, D' is evaluated for the first 10 design variables by finite-differences with $\Delta P = 1 \times 10^{-3}$. For the other design variables (i.e., structural and control) D' is zero. The derivatives of drag with respect to angle of attack, $\partial D / \partial \alpha$ is evaluated at rigid conditions (i.e., $\alpha = \alpha_r$ and $\boldsymbol{w} = 0$) by finite-differences with stepsize $\Delta P = 1 \times 10^{-5}$.

The quantities ϑ, V_L and $C_{L_{out}}$ are all calculated exactly in the optimization process. The derivatives of the approximate control deflection $\partial \beta_a / \partial P_i$ may be expressed as

$$\frac{\partial \beta_a}{\partial P_i} = \frac{\partial}{\partial P_i}\left(\frac{\partial \beta}{\partial \Delta \alpha_g} \Delta \alpha_g\right) \ , \tag{7.6}$$

where the derivatives on the right hand side of Eq.(7.6) can be determined from Eq.(6.31).

The control efficiency CE is calculated exactly from Eq.(6.24) based on a linear approximation to $\partial M_b/\partial\beta$ for both flexible and rigid wings as

$$\frac{\partial M_b}{\partial \beta}(\mathbf{P}) = \frac{\partial M_b}{\partial \beta}(\mathbf{P}^0) + \sum_{i=1}^{N_{DV}} \frac{\partial}{\partial P_i}\left(\frac{\partial M_b}{\partial \beta}\right)_{\mathbf{P}^0} \Delta P_i \ , \tag{7.7}$$

and

$$\left(\frac{\partial M_b}{\partial \beta}\right)_{rigid}(\mathbf{P}) = \left(\frac{\partial M_b}{\partial \beta}\right)_{rigid}(\mathbf{P}^0) + \sum_{i=1}^{N_{DV}} \frac{\partial}{\partial P_i}\left(\frac{\partial M_b}{\partial \beta}\right)_{rigid|_{\mathbf{P}^0}} \Delta P_i \ . \tag{7.8}$$

The optimizer used in this study is the NEWSUMT-A program[68] which was also used earlier in the integrated design optimization of the simplified wing. The optimization algorithm used in NEWSUMT-A is based on an extended interior penalty function method, and allows for various levels of constraint and objective function approximations.

7.1 Solution Procedure

The solution process begins by first selecting a set of design variables $\mathbf{P}^0$ which define the initial design. The finite-element mesh generator then uses the planform design variables along with the information about the wing-interior structural configuration (e.g., number of spars, ribs, etc.) and generates the structural grid. The load-set nodal locations are then defined with respect to the structural grid nodes. The wing structural weight W_w is calculated next through a structural analysis by WIDOWAC. The general analyses calculations which follow are modularized as shown in Figure 7.1.

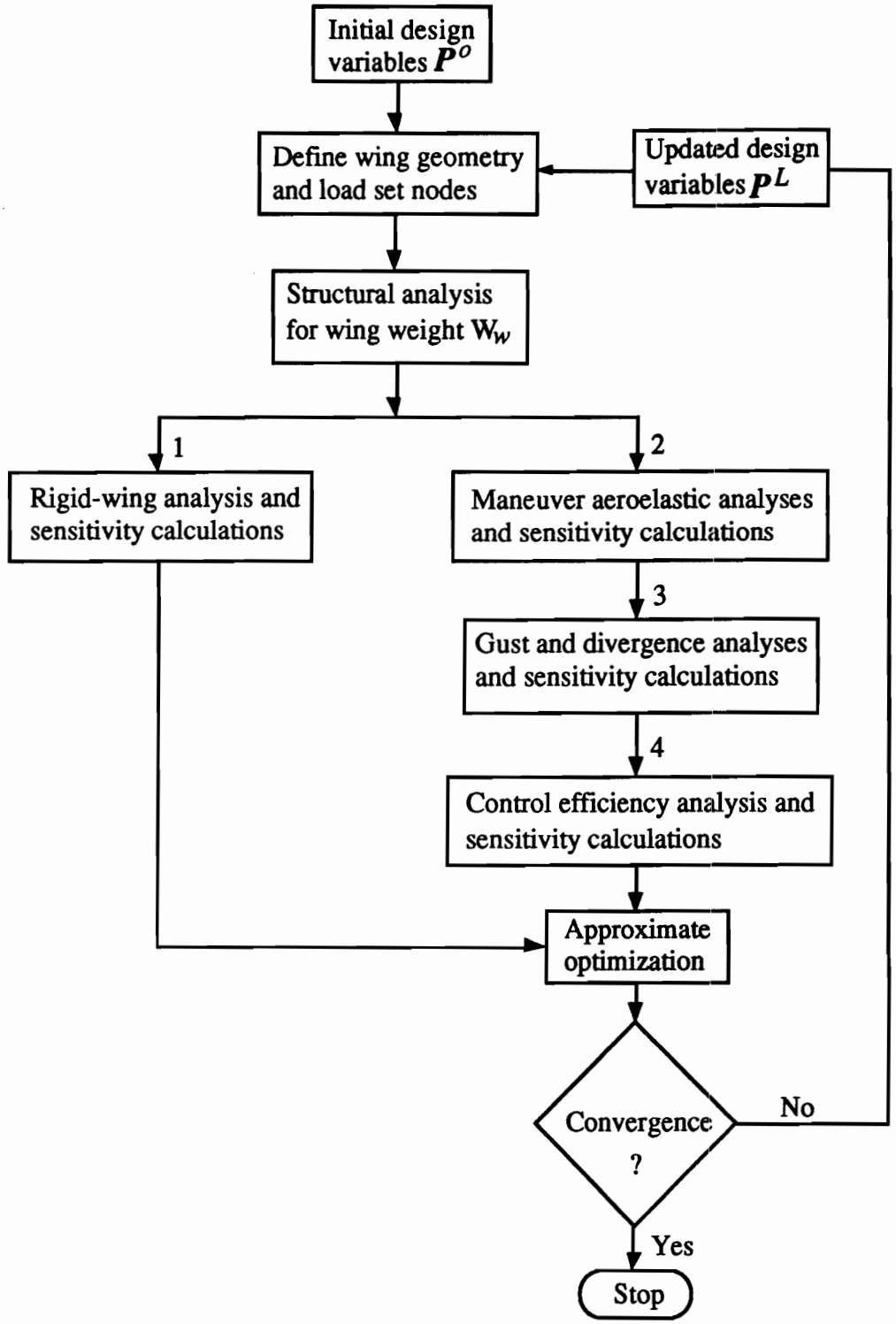

Figure 7.1 Design Procedure Flow Chart

The initial information along with the structural wing weight are used for rigid-wing drag analysis and sensitivity calculations at $q = q_c = P_9$. With the vectors $\boldsymbol{f}_1$ and $\mathbf{R}$, matrix A, gross weight W and rigid angle of attack α_r already determined in chapter 6, the total drag D is then calculated at the same conditions (i.e., $\mathbf{P}^0$, $\alpha = \alpha_r$ and $\boldsymbol{w} = 0$) by an aerodynamic analysis which includes the induced and viscous drag calculations.

To calculate the drag sensitivities, first $\boldsymbol{f}_1'$ and f_2' are calculated by finite differences. Then Eq.(6.27) is used to calculate α' by setting $\boldsymbol{w}'$ and $\boldsymbol{f}_3'$ equal to zero which is consistent with the rigid-wing assumptions. Next, the partial derivatives D' and $\partial D/\partial\alpha$ are calculated by finite differences. Finally Eq.(7.5) is used to calculate the sensitivities of drag with respect to each design variable P_i. This procedure is shown in a flow chart in Figure 7.2.

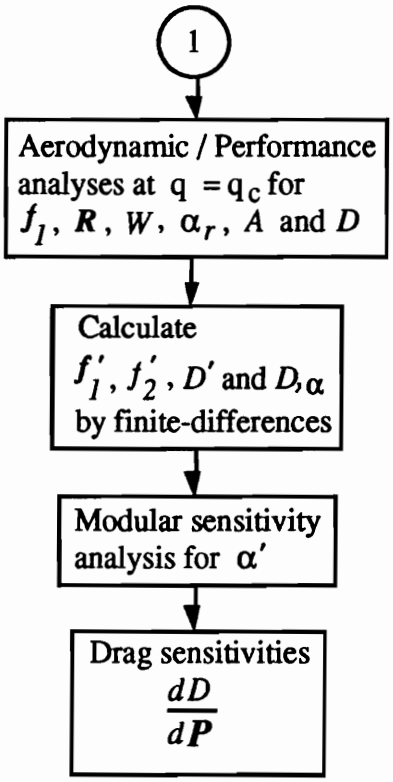

Figure 7.2 Rigid-Wing Analysis and Sensitivity Calculations Flow Chart

The Maneuver analyses begin by first calculating the structural flexibility matrix S by WIDOWAC. Then, the procedure discussed previously for the rigid-wing is repeated up to the end of A matrix calculations with $q = q_m = 2.5q_c$. Aeroelastic analysis is performed next by solving Eqs.(6.9) to (6.11), and calculating the force vector $\mathbf{F}_a$, the angle of attack α and the load-set vertical displacement vector $\boldsymbol{w}$. The finite-difference approach is used to calculate the derivatives $\boldsymbol{f}_1'$, $\boldsymbol{f}_2'$ and $\boldsymbol{f}_3'$. Then using the modular sensitivity approach, the derivatives $\mathbf{F}_a'$, α' and $\boldsymbol{w}'$ are calculated by solving Eqs.(6.28) to (6.30). The force vector $\mathbf{F}_a$ and the derivative matrix $\mathbf{F}_a'$ evaluated at $\mathbf{P}^0$ are then used in formulating a first order Taylor series expansion for the aerodynamic force vector $\mathbf{F}_a$ which is used along with the inertia and gravitational force vector $\mathbf{F}_I$ in an structural analysis for the calculation of structural constraints (on stresses and strains) and their derivatives. This procedure is shown in Figure 7.3.

The gust and divergence calculations are performed as follows. First the aerodynamic incremental force vector $\mathbf{C}$ is calculated at conditions ($\mathbf{P}^0, \alpha = 0$ and $\boldsymbol{w} = 0$) by making a simultaneous and uniform perturbation in all load-set nodes which are located at the trailing edge of the control surface. This is consistent with making a unit perturbation in the control deflection β. The perturbed force vector is then calculated from a vortex-lattice analysis. Then the vector $\mathbf{C}$ is calculated by finite-differences. Equation (6.25) is then used to calculate the divergence dynamic pressure q_D and its corresponding eigenvectors (i.e., $\mathbf{F}_{a_D}$, $\boldsymbol{w}_D$ and β_D). Equation (6.63) is used to calculate the left eigenvectors (i.e., $\mathbf{F}_{a_L}$, $\boldsymbol{w}_L$ and β_L). The modular sensitivity approach is used to calculate the terms involving the derivatives of matrices A and S in Eq.(6.65) which is then used to calculate the divergence sensitivities $\partial q_D / \partial P_i$.

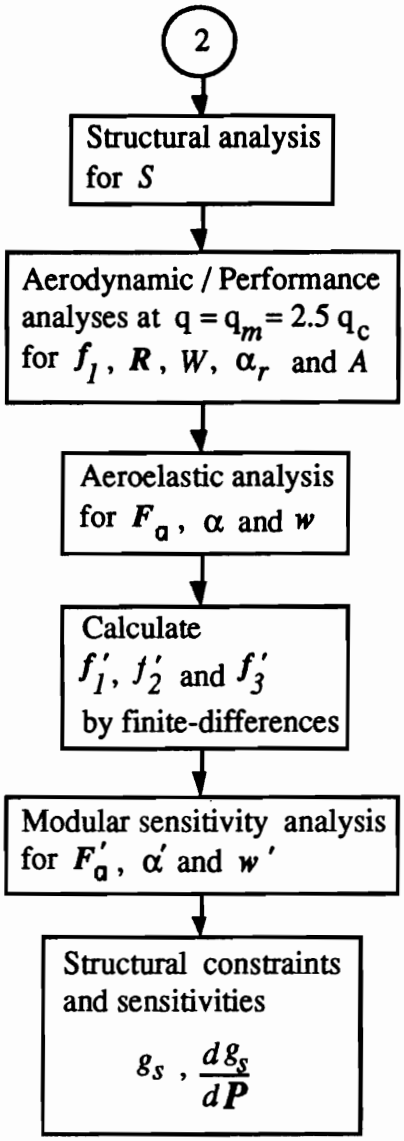

Figure 7.3 Maneuver Aeroelastic and Sensitivity Calculations Flow Chart

The gust analyses follow the calculation of the **C** vector by calculating the gust-induced incremental angle of attack $\Delta\alpha_g$. Equation (6.18) is then solved for the derivatives of $\mathbf{F}_a$, $\boldsymbol{w}$ and β with respect to $\Delta\alpha_g$. The approximate control deflection β_a is calculated based on a linear approximation to β from Eq.(6.14). Following the procedure in section 6.6, the control deflection sensitivities $\partial\beta_a/\partial P_i$ are calculated from Eq.(6.31). The gust and divergence analyses procedure is shown in Figure 7.4.

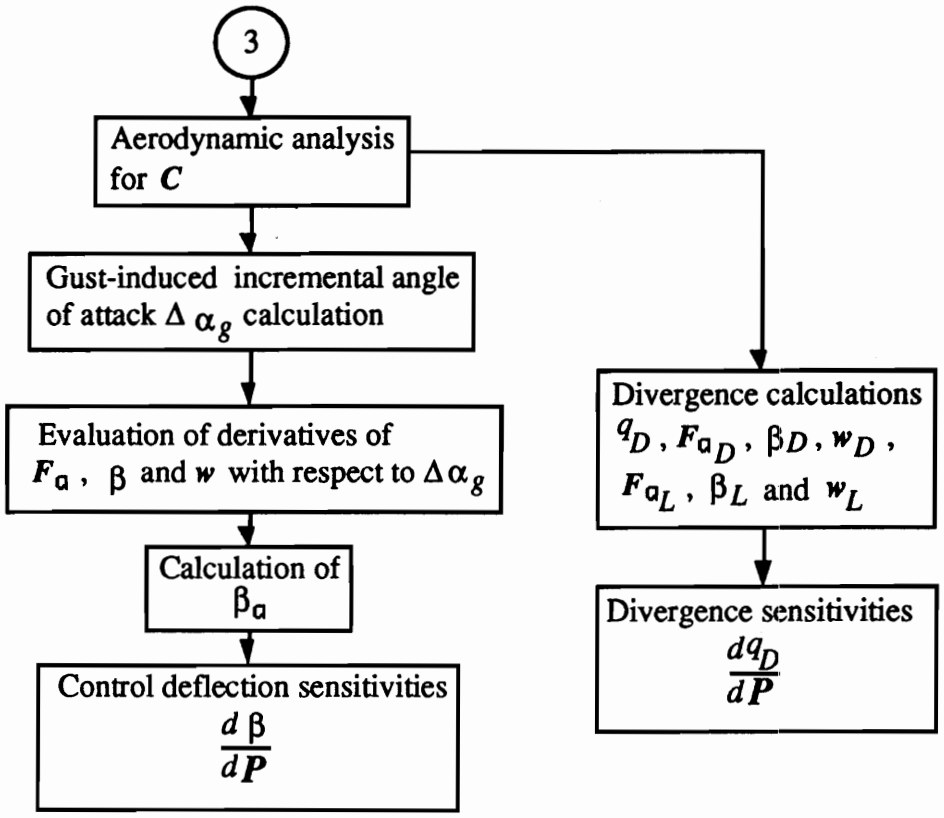

Figure 7.4 Gust and Divergence Analyses and Sensitivity Calculations Flow Chart

The control efficiency analysis begins by calculating the derivative of the root bending moment with respect to control deflection $\partial M_b/\partial\beta$ for both flexible and rigid wings from Eqs. (6.22) and (6.23). The second derivatives of M_b and $M_{b_{rigid}}$ with respect to P_i are evaluated from Eqs.(6.49) and (6.61). The control efficiency CE at $\mathbf{P}^0$ is calculated next from Eq.(6.24). During optimization, the control efficiency will be calculated exactly based on the first order Taylor series approximation for the derivatives of the bending moment given by Eqs.(7.7) and (7.8). The flow chart for this procedure is shown in Figure 7.5.

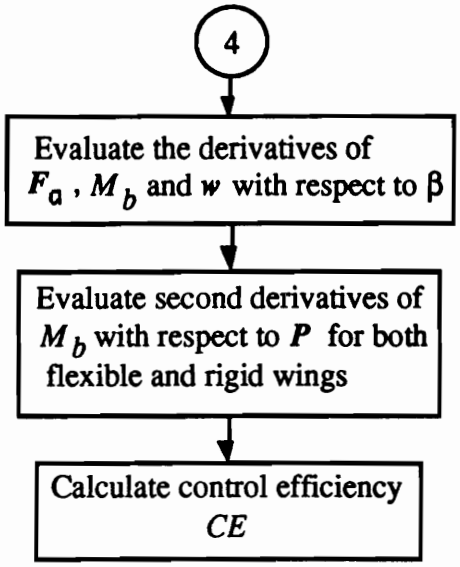

Figure 7.5 Control Efficiency and Sensitivity Calculations Flow Chart

7.2 Optimization Results

The optimization procedure began with the case which utilizes both active controls and aeroelastic tailoring for divergence suppression. The initial design had very thin wing-box skins which resulted in 194 structural constraints (mostly the skin strains and including the divergence dynamic pressure) violations. Also the outboard-section span constraint was violated initially. At the beginning the move limits were set to 5% for all design variables except the gain design variables which had 10% move limits. These move limits were chosen to ensure accuracy in the approximation used for most of the constraints. However, larger move limits were also tried at the beginning, but proved to be inappropriate as they resulted in a substantial difference between the approximate values of some of the constraints (mostly structural) at the end of an approximate optimization cycle (iteration) and the exact values determined at the start of the next cycle. With the selected move limits being fairly small and the number of initial constraint violations rather large,

it took 7 approximate optimization cycles to gradually satisfy all the constraints. The results of the optimization for the case which includes both active controls and aeroelastic tailoring are plotted in Figures 7.6 to 7.22.

Initially the gross weight decreased followed by a temporary increase. This behavior was traced to the changes in the wing and fuel weights. The wing's initial weight increase was mostly due to the increase in the wing planform area and partially due to the increase in thickness of some skin plies and area of some spar cap elements in order to satisfy the structural constraints. However, this weight increase was offset by the reduction in fuel weight, and the gross weight subsequently decreased. After the 4th cycle, the increase in the wing weight and the resulting standard empty weight exceeded the reduction in fuel weight, and the gross weight gradually increased until the end of the 7th approximate optimization cycle at which point all structural constraints were satisfied.

The optimization process continued using the same move limits till the end of 13th cycle. At this point an upper limit of 10 was imposed on the control efficiency. This was done because as the control efficiency became larger, the approximation for flexible-wing bending moment became poorer. As a result the control efficiency at the end of an approximate optimization cycle would be very far from the exact value determined at the beginning of the next cycle. At this point, it was also felt that a reduction in move limits was also necessary to assure greater accuracy in the approximations. Hence the move limits were reduced from 5% to 3% with the move limits on the gain design variables kept at 10%.

At the end of 20th cycle while keeping the other move limits fixed, the move limit on fuel weight design variable was increased to 8%. This move limit increase was considered proper since the fuel weight was continuously decreasing through out the design while the range constraint was always satisfied (see Figure 7.22).

The process continued to 29th cycle with the gross weight continuously decreasing. Also, since no upper limit was imposed on the cruise altitude, the dynamic pressure was being reduced by increasing the cruise altitude and at the same time increasing the total wing span and aspect ratio which resulted in substantial drag reduction. Since the engine performance was not included in the analyses, it was necessary to impose a reasonable ceiling on the cruise altitude. At this point a ceiling of 13500 m (45000 ft) was placed on the cruise altitude. This altitude cap resulted in the rapid reduction in the wing span which affected the wing area and structural weight which led to a sudden reduction in the gross weight and sudden increase in dynamic pressure and drag. The increase in drag resulted in an increase in fuel weight. Since the cruise-altitude ceiling was imposed rapidly over the following 4 cycles, it resulted in an oscillation in the wing twist design variables, sweep angle, control deflection, control efficiency, drag and usable fuel weight immediately following the 29th cycle. Following this interruption, the optimization process continued smoothly till 52nd cycle at which point the move limits were all reduced to 2% with those for gain design variables also reduced to 5%. This was necessary because most of the structural constraints were becoming active and the gross weight variation was becoming smaller, indicating convergence approach.

The control deflection necessary to suppress divergence was in upward or negative direction. This pattern continued through out the design till the maximum value of upward deflection ($-10°$) was reached eventually. The sequential approximate optimization procedure was continued till the end of the 60th cycle at which point the improvement in gross weight per cycle was approximately 0.005% with 40 of the skin strain constraints being active (i.e., $g_s < 2\%$). The margins on the other structural constraints (with the exception of the spar caps stress constraints)

were in the order of 10% to 30%. Also the constraints on landing speed, control deflection, divergence dynamic pressure and range were all active at this point.

The initial and final wing-planform geometry for this case are shown in Figure 7.23. The final wing area is approximately 28% smaller than the initial wing with approximately 14% higher aspect ratio. The overall improvement in the gross weight is approximately 6% over the initial value. The improvement in the structural weight of one wing at the end of the optimization effort is approximately 20%. The completion of 60 cycles required approximately 42 (CPU) hrs. with each approximate optimization cycle taking over 2500 (CPU) sec. on an IBM 3090 mainframe.

In order to determine the contribution of the active controls and aeroelastic tailoring each in divergence suppression of the forward-swept wing design problem, the active control terms were removed from the divergence calculations. However, the control efficiency constraint was kept in the design optimization. To avoid additional computational cost, the design at the 40th cycle in the previous case was chosen as the initial design. The weight iteration history for this case is compared with the previous case in Figures 7.24 and 7.25. Since the effect of active control on divergence suppression was suddenly removed, the optimizer increased the structural sizing variables to avoid divergence which resulted in a rapid increase in the structural and gross weights. However, in just 2 cycles the optimizer began utilizing the aeroelastic tailoring more effectively which resulted in the reduction of structural sizing and gross weight. After 20 cycles the optimization reached an acceptable convergence, and the procedure was stopped.

The wing planform geometry in this case is compared to that in the previous case in Figure 7.26. As can be seen, the difference between the two final designs is minimal. The design characteristics in both cases are compared to the initial

design in Table 7.1. The initial and final design variables are listed in Tables 7.2 to 7.4. Comparing the results obtained in this study, a difference of only 0.2% in the gross weight and 2% in the structural wing weight is observed. This small difference indicates that most of the divergence suppression capability in the forward-swept wing example comes from aeroelastic tailoring of composite skins.

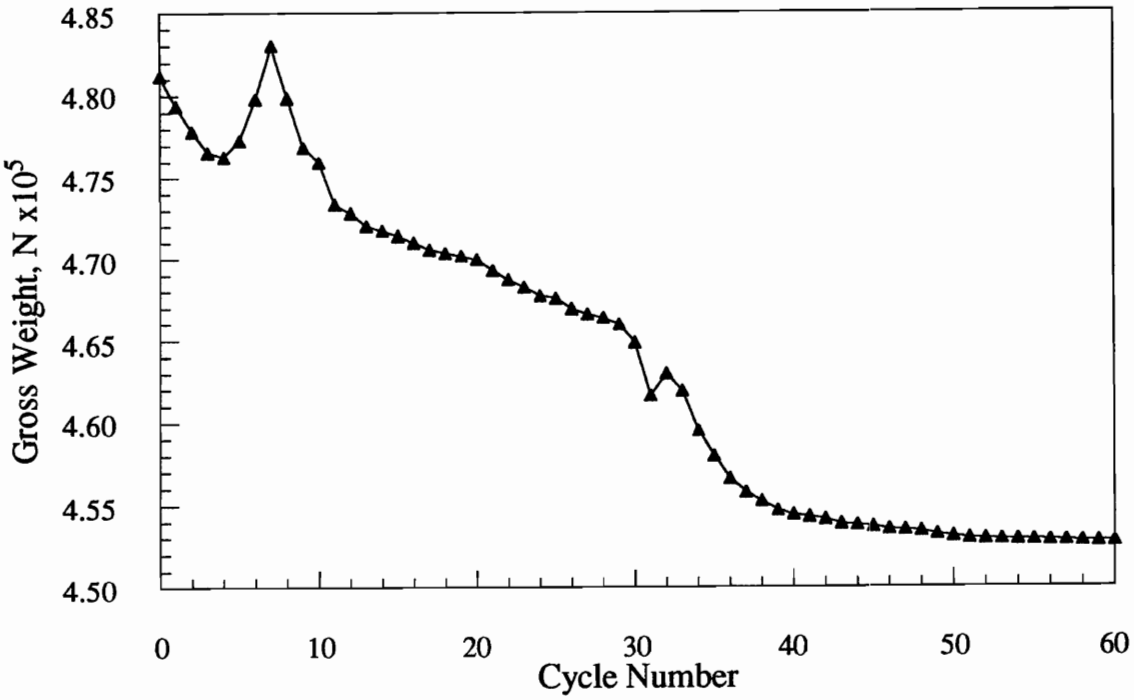

Figure 7.6 Gross Weight Convergence History

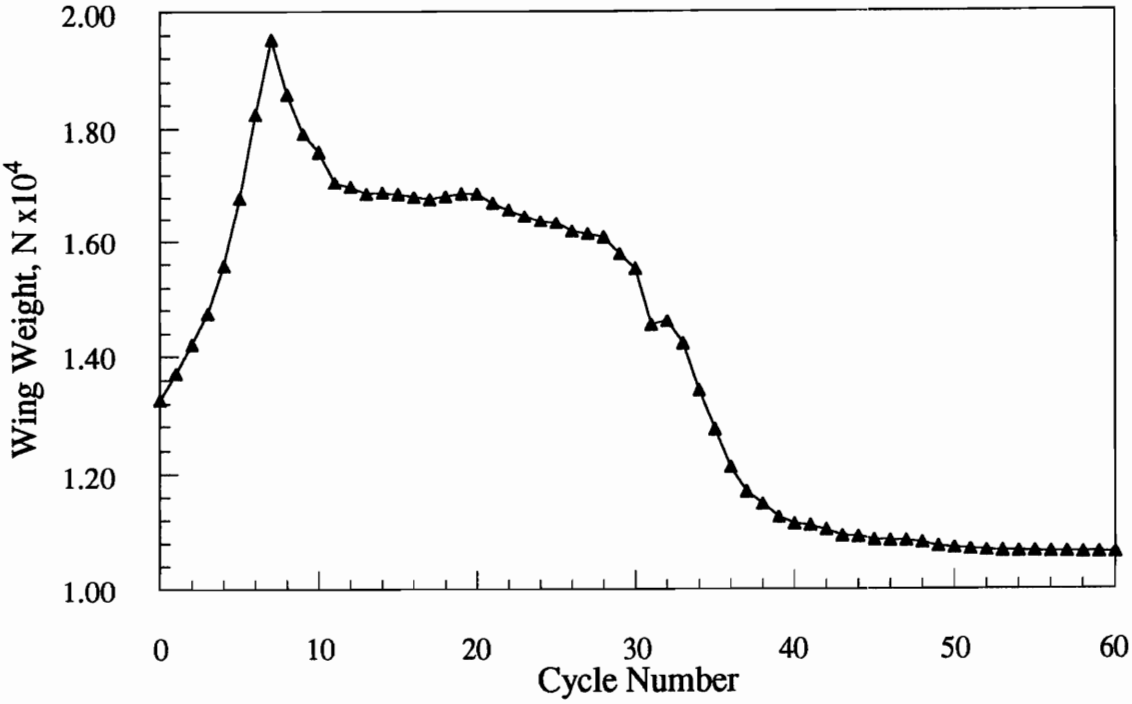

Figure 7.7 Wing Weight Convergence History

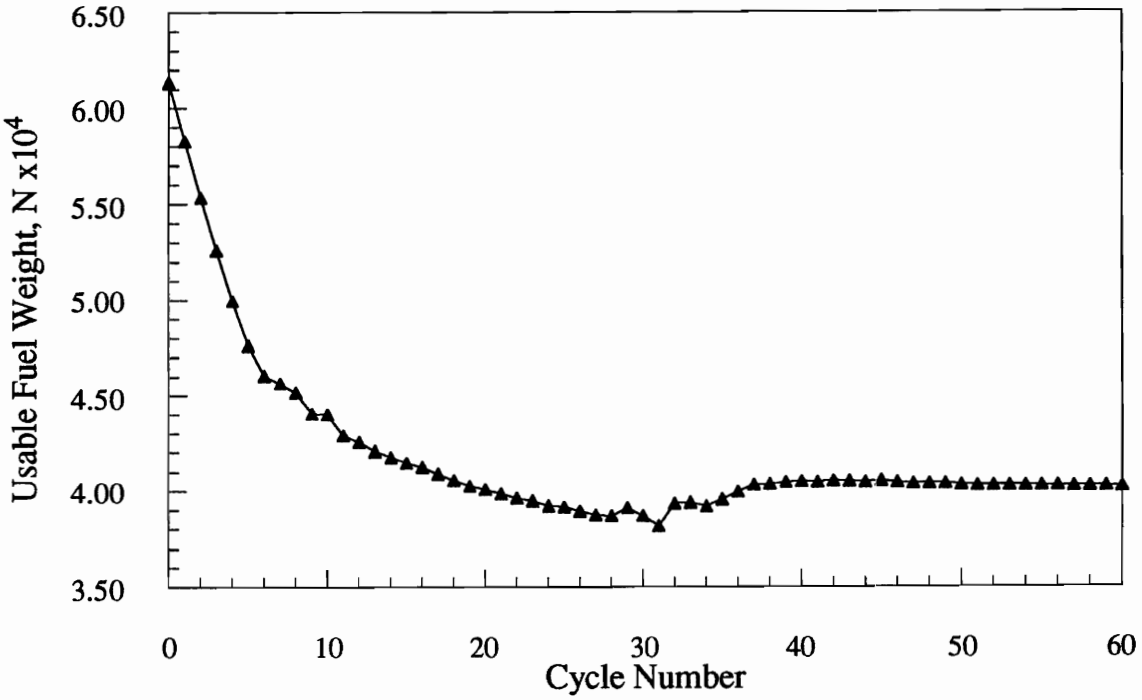

Figure 7.8 Usable Fuel Weight Vs Cycle Number

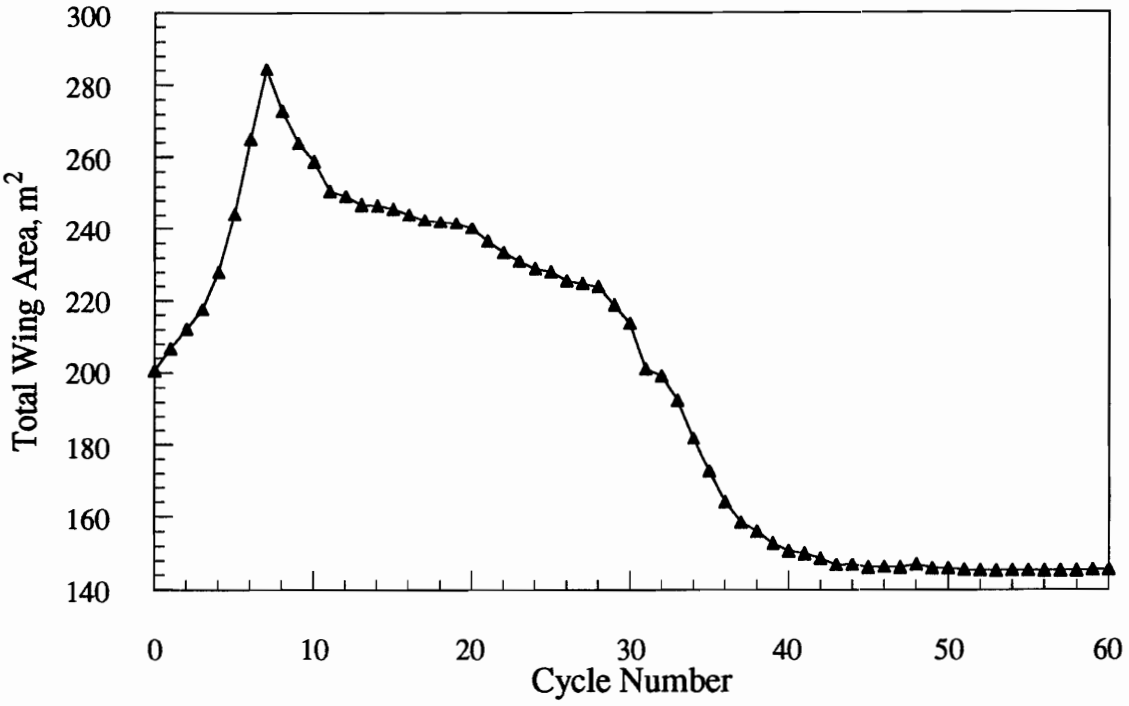

Figure 7.9 Total Wing Area Vs Cycle Number

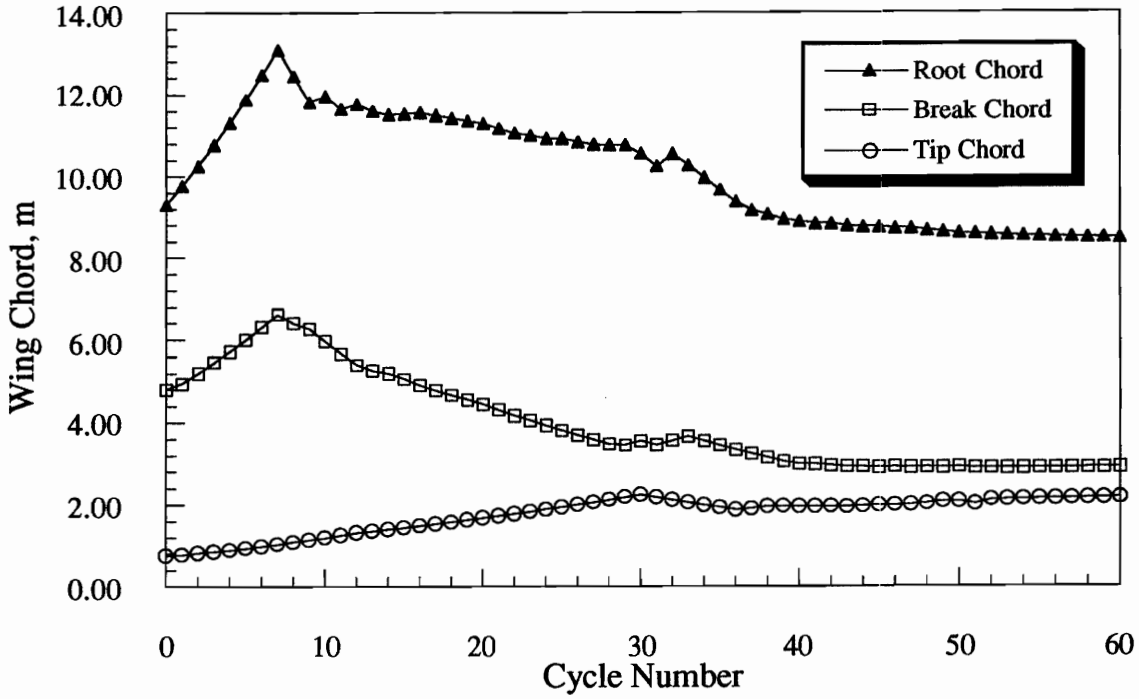

Figure 7.10 Wing Chord Vs Cycle Number

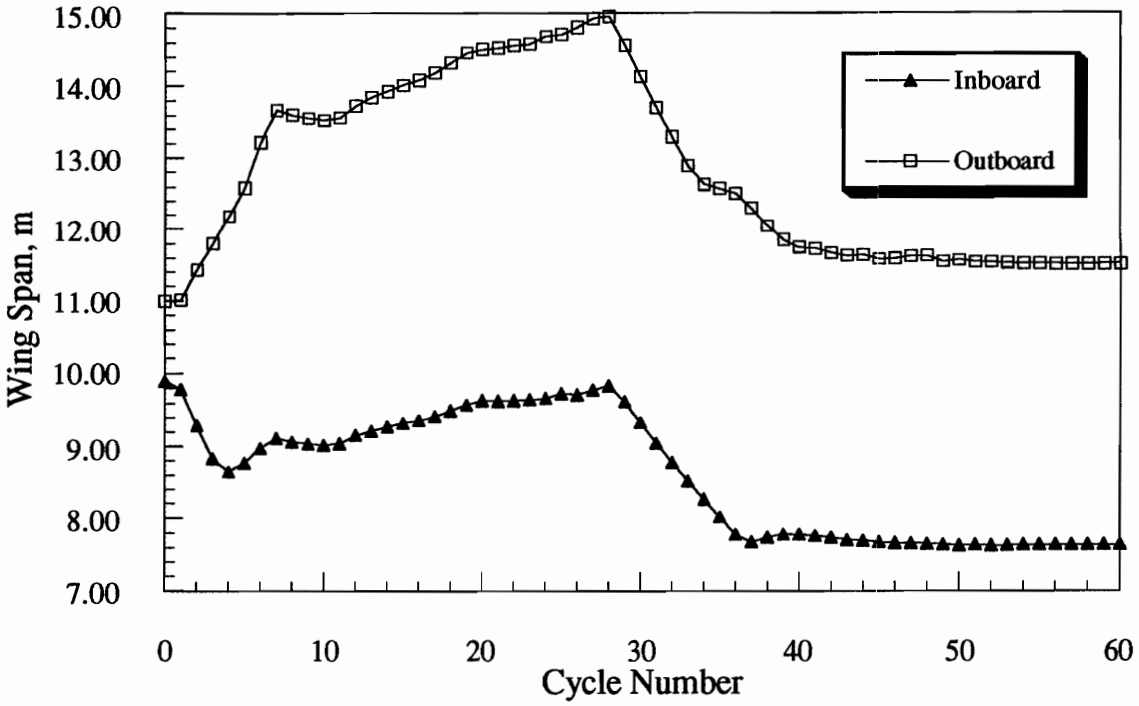

Figure 7.11 Wing-Section Span Vs Cycle Number

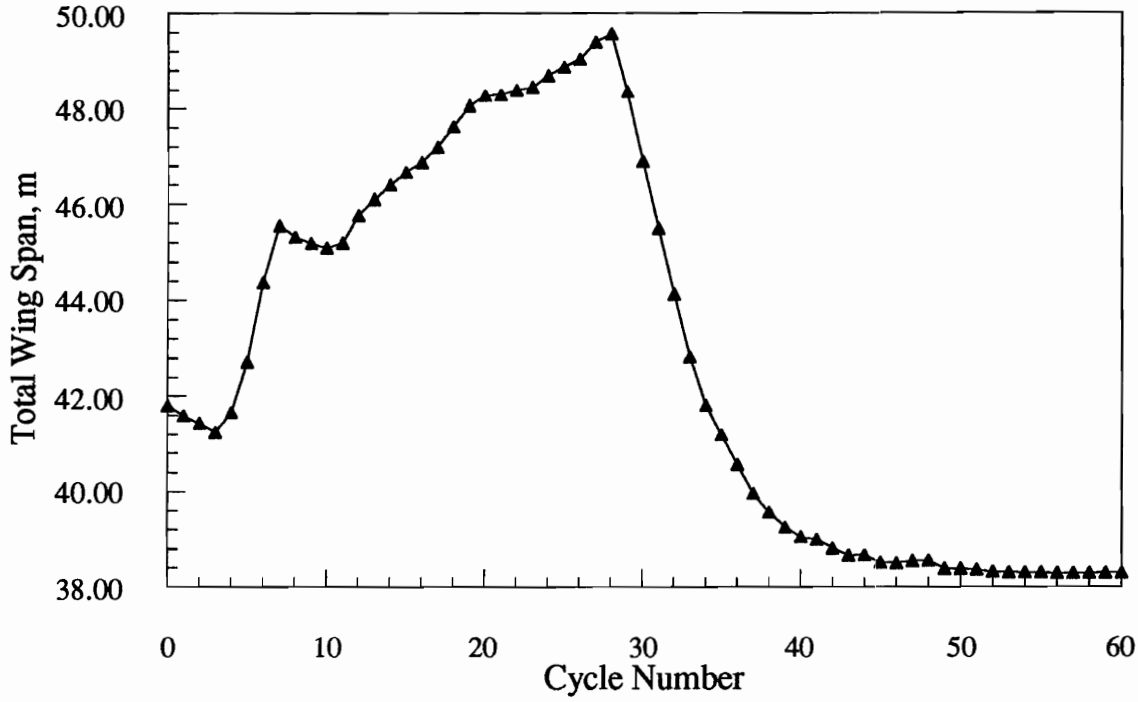

Figure 7.12 Total Wing Span Vs Cycle Number

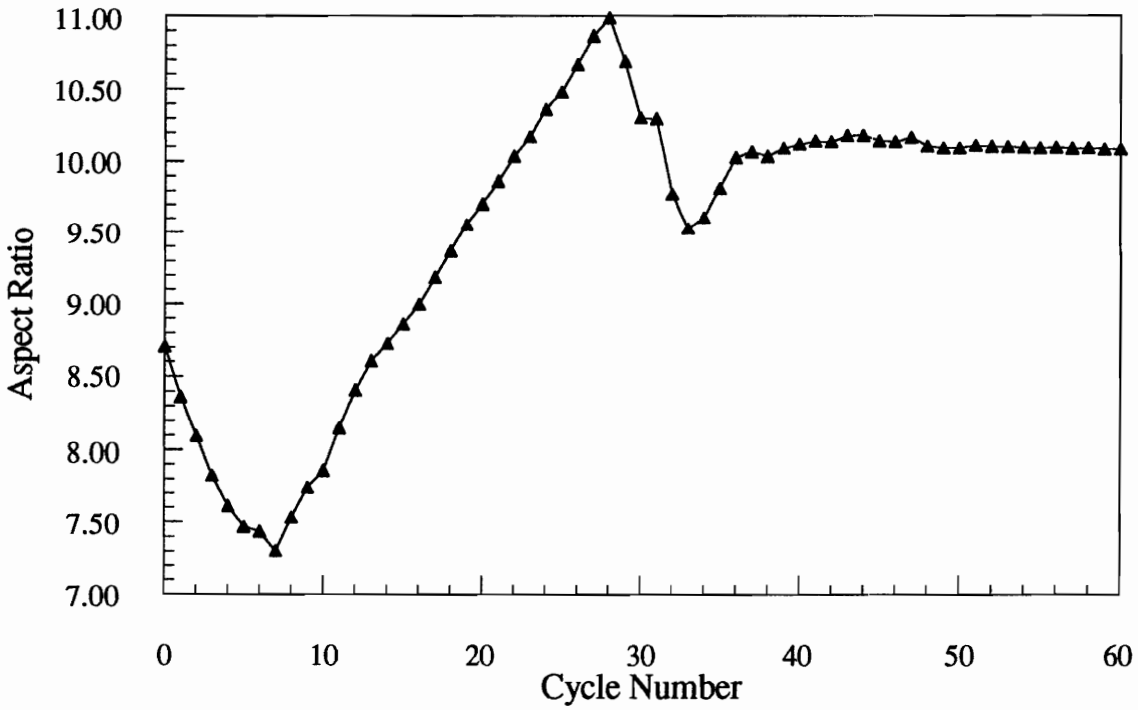

Figure 7.13 Aspect Ratio Vs Cycle Number

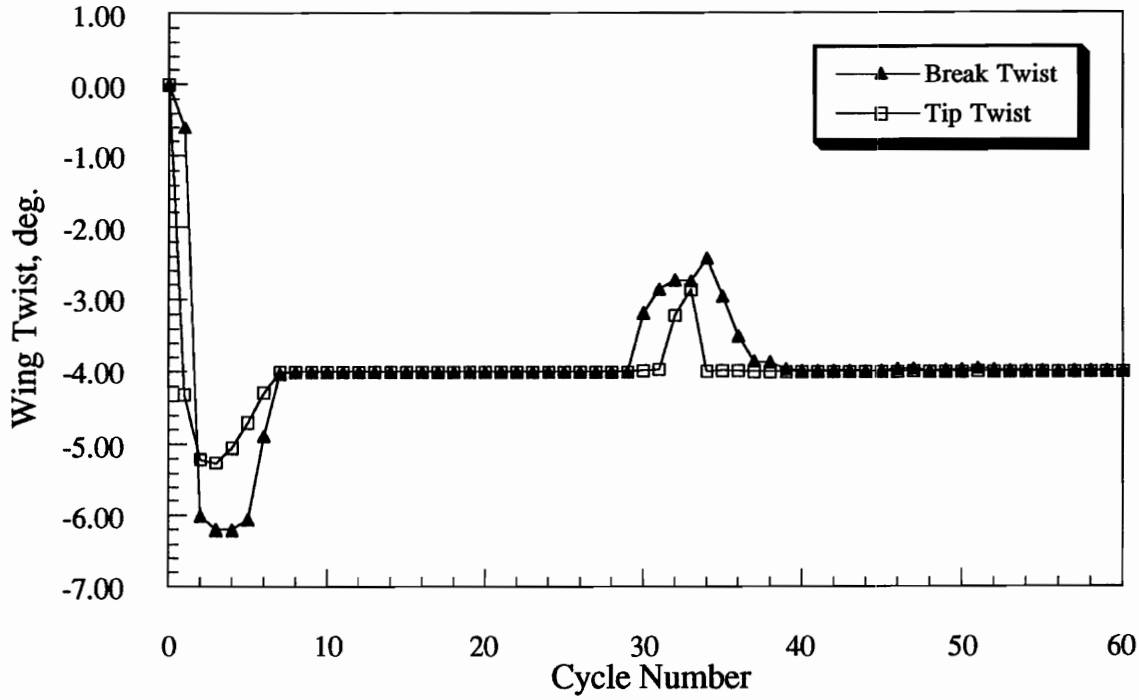

Figure 7.14 Wing Twist Vs Cycle Number

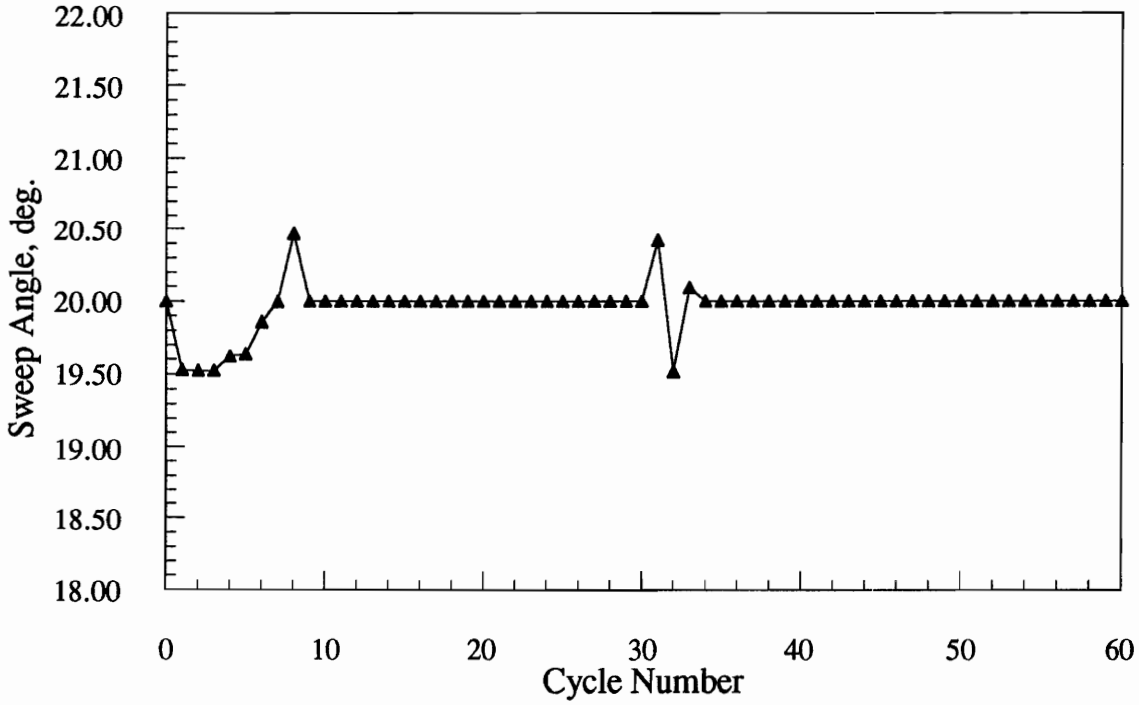

Figure 7.15 Sweep Angle Vs Cycle Number

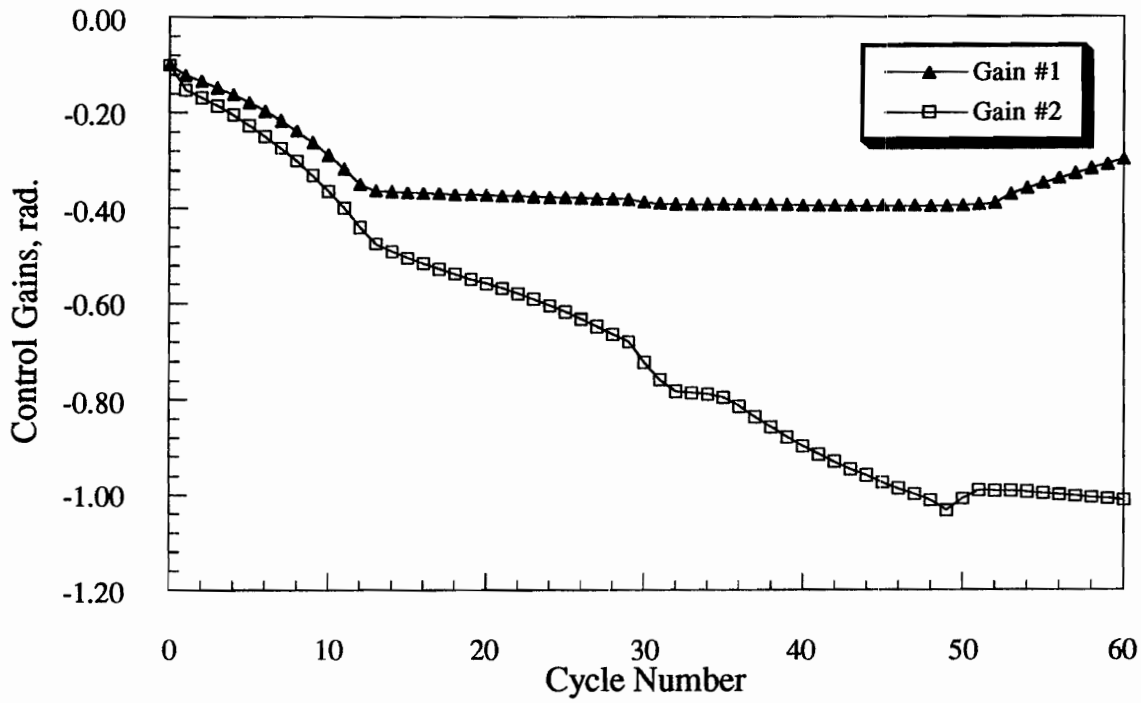

Figure 7.16 Control Gains Vs Cycle Number

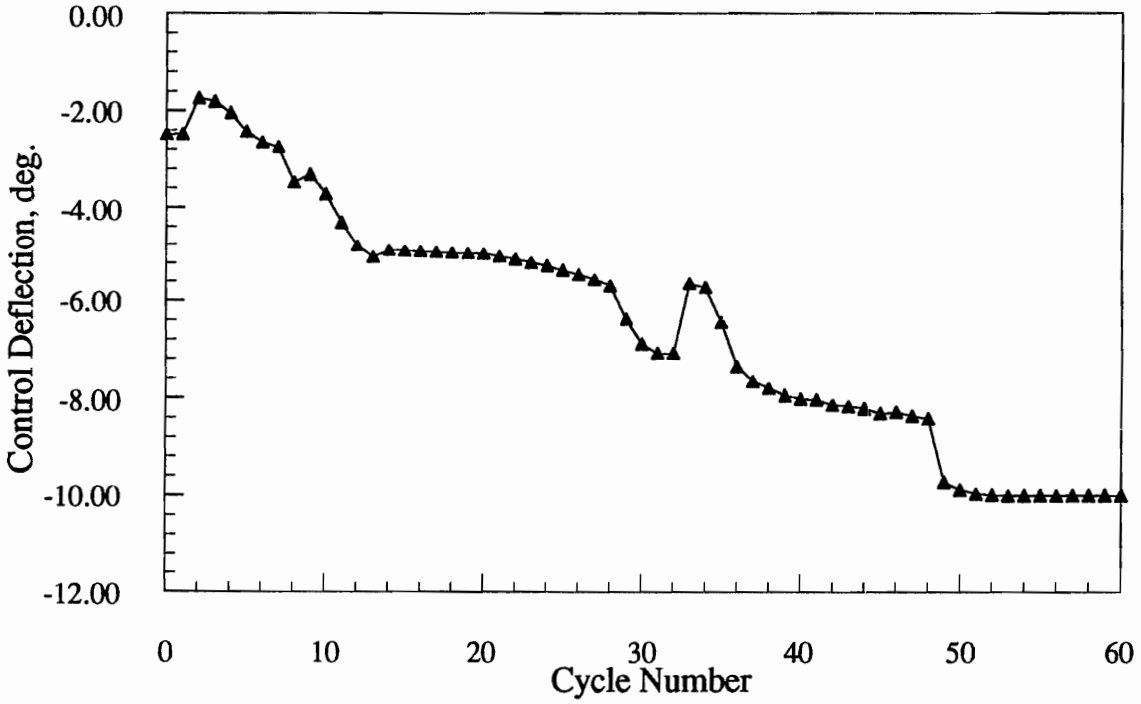

Figure 7.17 Control Deflection Vs Cycle Number

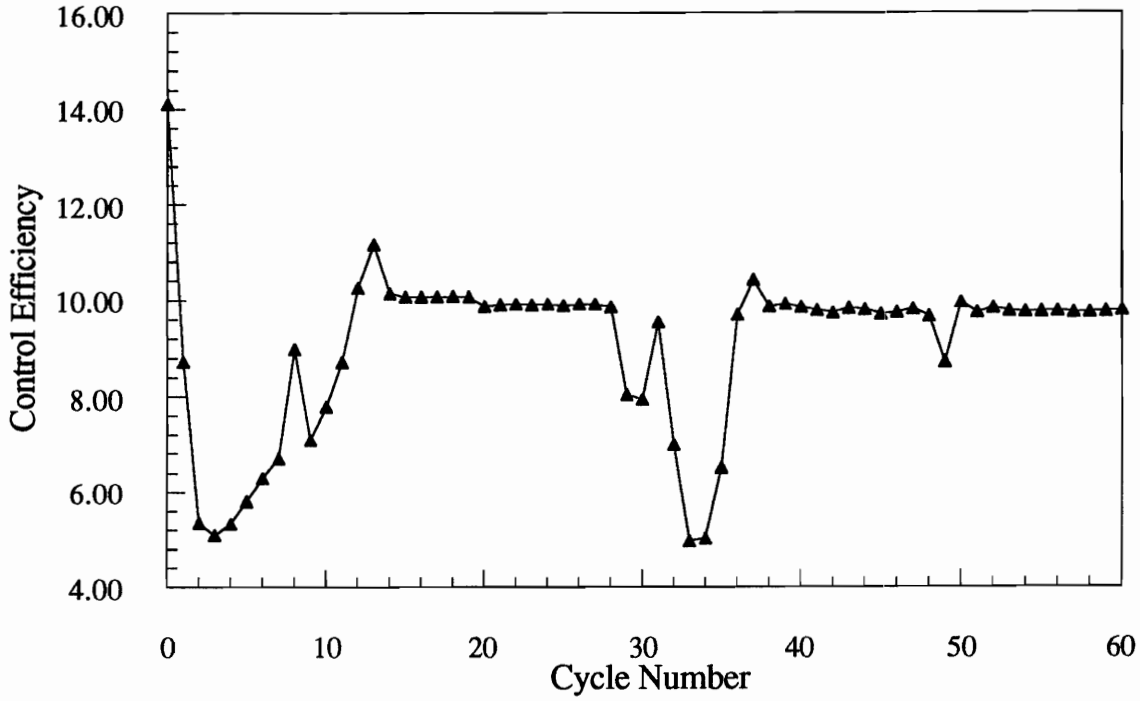

Figure 7.18 Control Efficiency Vs Cycle Number

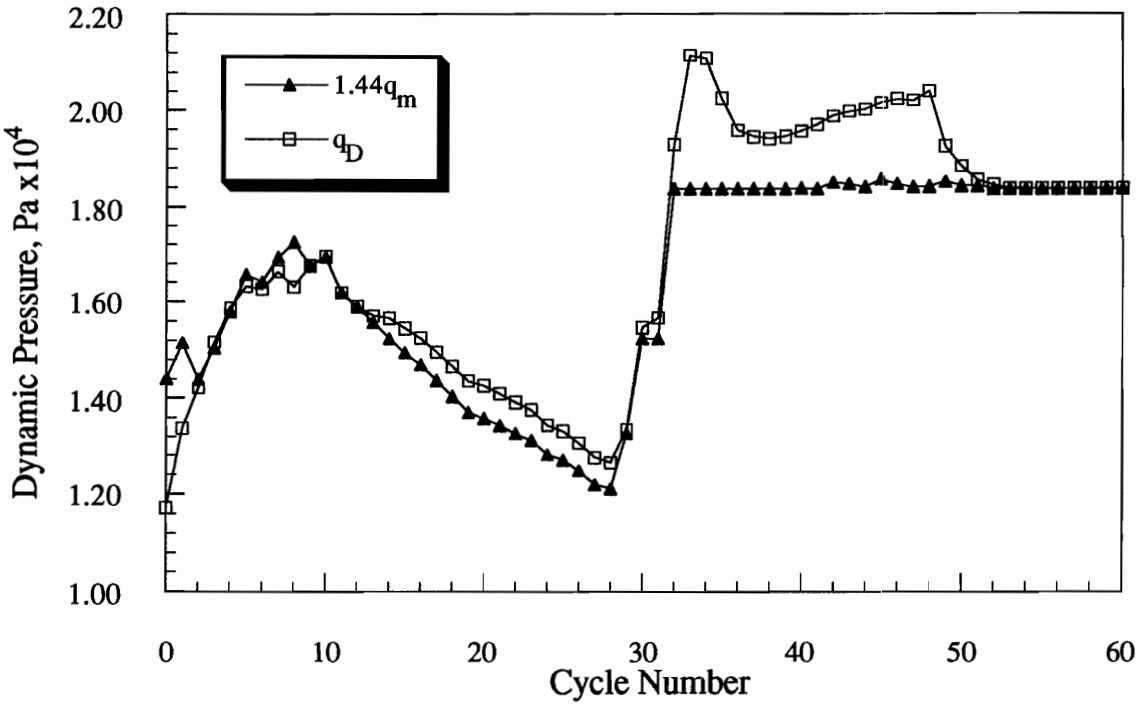

Figure 7.19 Dynamic Pressure Vs Cycle Number

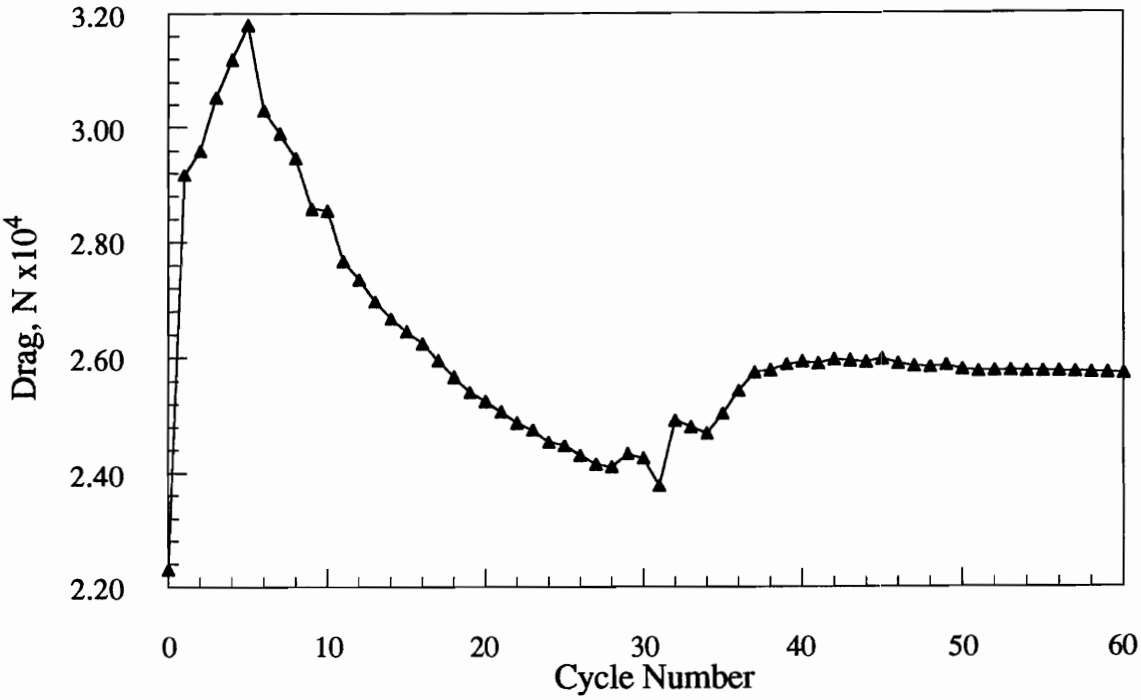

Figure 7.20 Drag Vs Cycle Number

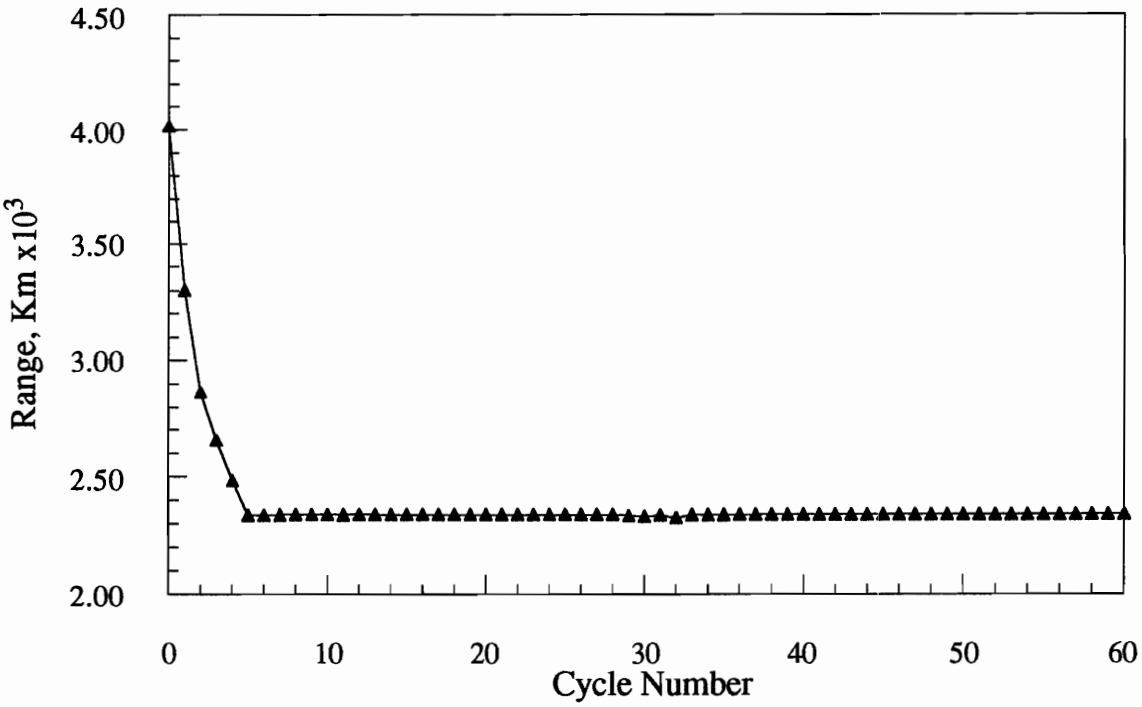

Figure 7.21 Range Vs Cycle Number

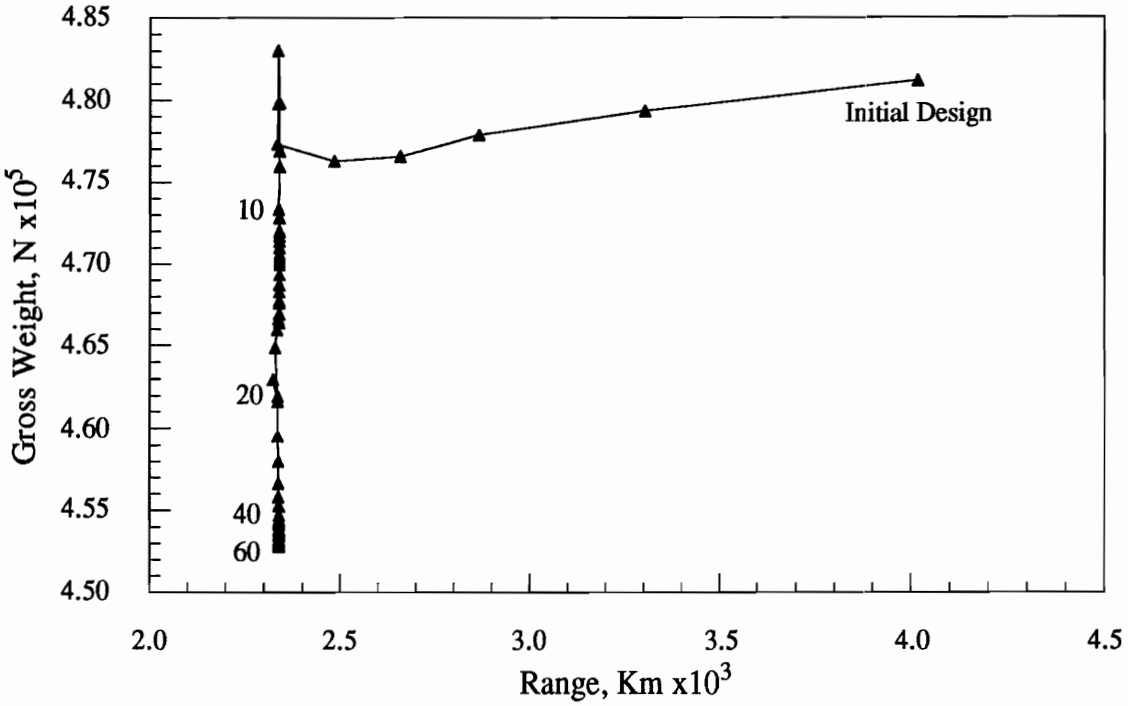

Figure 7.22 Gross Weight Vs Range

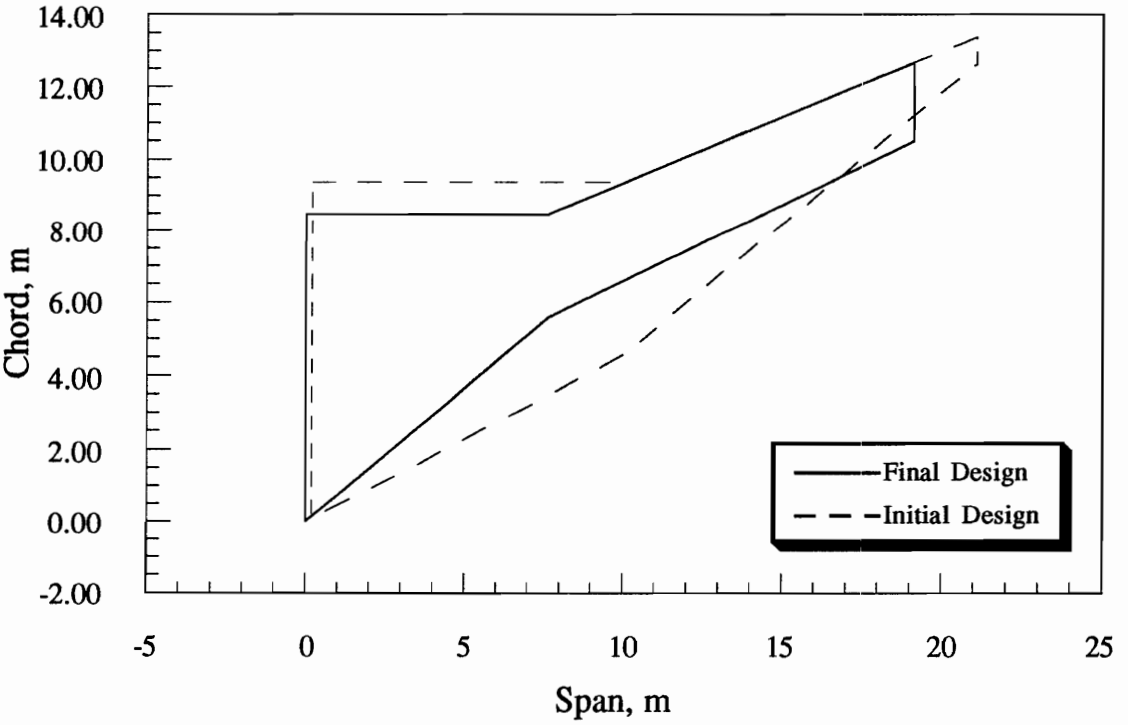

Figure 7.23 Initial and Final Wing Design Configurations

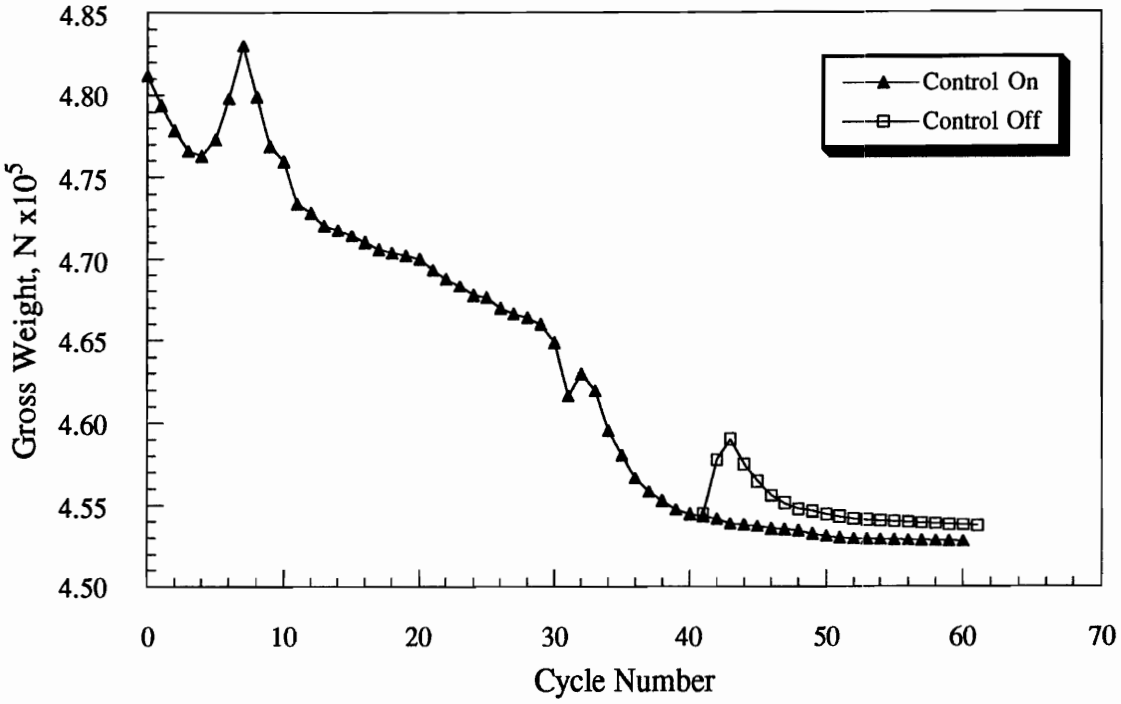

Figure 7.24 Comparison of Gross Weight Convergence History for the Case With and Without Active Control

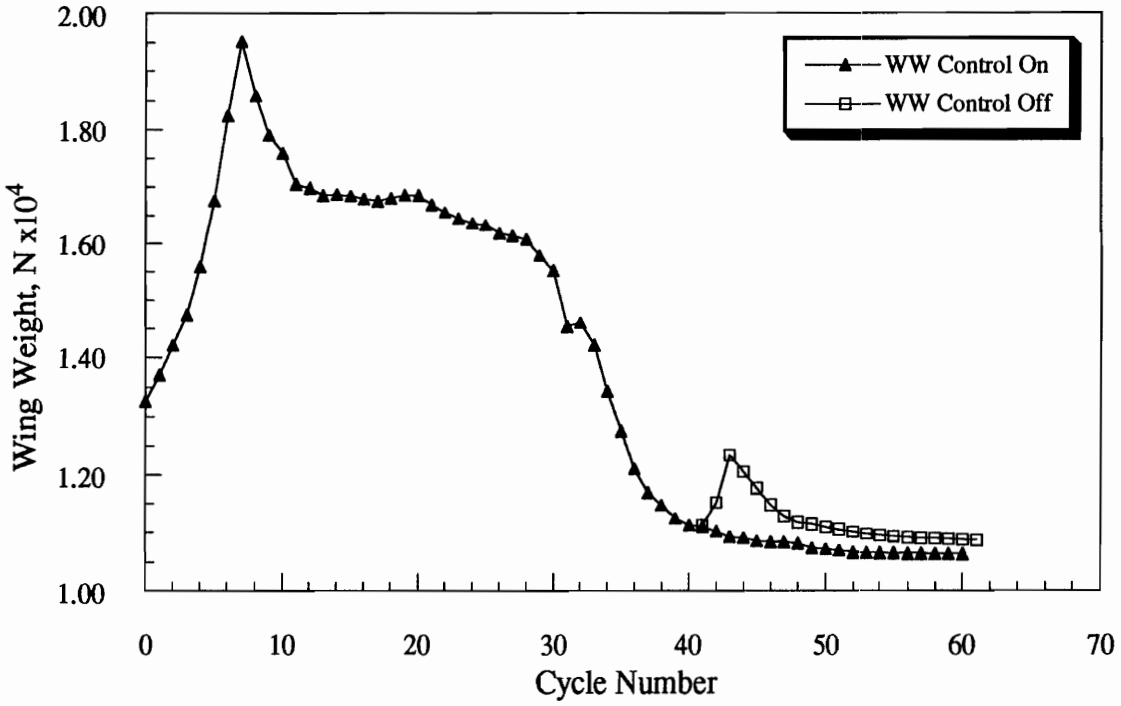

Figure 7.25 Comparison of Wing Weight Convergence History for the Case With and Without Active Control

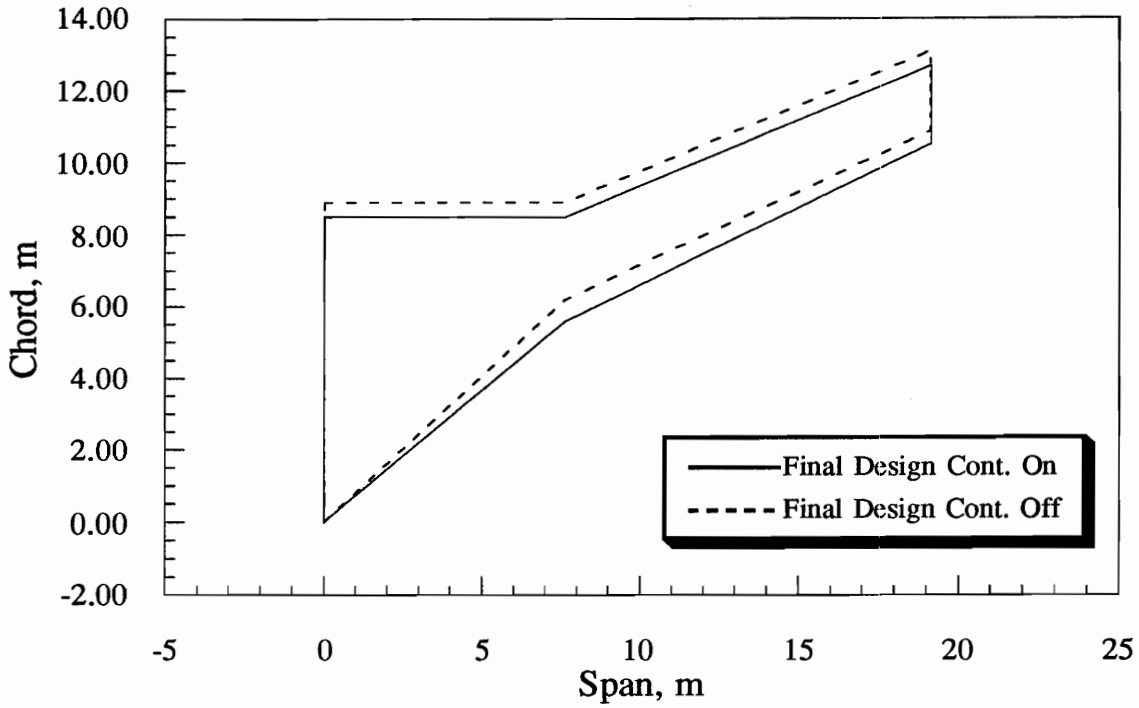

Figure 7.26 Final Wing Designs Comparison

Table 7.1 Initial and Final Wing Design Characteristics

Parameter	Initial	Final Control On	Final Control Off
Gross Weight, N	4.81181×10^5	4.52760×10^5	4.53718×10^5
Wing Structural Weight, N	1.32589×10^4	1.06343×10^4	1.08675×10^4
Total Wing Area, m^2	200.64	145.43	145.09
Total Wing Span, m	41.80	38.29	38.24
Aspect Ratio	8.71	10.08	10.07
Range, Km	4.0159×10^3	2.3383×10^3	2.3383×10^3

Table 7.2 Initial and Final Aerodynamic Design Variables

Design Variable*	Initial	Final Control On	Final Control Off
P_1, m	9.3000	8.4909	8.8967
P_2, m	4.8000	2.9044	2.7015
P_3, m	0.7500	2.1692	2.2233
P_4, m	9.9000	7.6375	7.6320
P_5, m	11.0000	11.5083	11.4867
P_6, $deg.$	20	20	20
P_7, $deg.$	0.0000	-3.9878	-3.8847
P_8, $deg.$	0.0000	-4.0000	-3.9992
* for definition of each design variable refer to Table 4.2			

Table 7.3 Initial and Final Performance and Control Design Variables

Design Variable*	Initial	Final Control On	Final Control Off
P_9, Pa	4000.00	5103.23	5103.23
P_{10}, N	61331.80	40247.57	40552.78
P_{11}, $rad.$	-0.1000	-0.299	1.0000
P_{12}, $rad.$	-0.1000	-1.010	1.0000
* for definition of each design variable refer to Table 4.2			

Table 7.4 Initial and Final Structural Design Variables

Design Variable*	Initial	Final Control On	Final Control Off
P_{13}, m	0.49177×10^{-3}	3.38534×10^{-4}	3.22715×10^{-4}
P_{14}, m	0.57095×10^{-3}	1.51637×10^{-3}	1.88420×10^{-3}
P_{15}, m	0.10421×10^{-3}	1.82699×10^{-5}	1.12600×10^{-5}
P_{16}, m	0.04547×10^{-3}	4.07603×10^{-5}	3.37644×10^{-5}
P_{17}, m	0.16092×10^{-3}	3.20212×10^{-5}	2.09687×10^{-5}
P_{18}, m	0.08739×10^{-3}	2.80482×10^{-5}	2.24237×10^{-5}
P_{19}, m	0.09392×10^{-3}	6.82327×10^{-5}	5.12976×10^{-5}
P_{20}, m	0.04336×10^{-3}	1.85474×10^{-5}	1.19917×10^{-5}
P_{21}, m	1.42899×10^{-3}	1.57621×10^{-3}	1.59514×10^{-3}
P_{22}, m	0.21999×10^{-3}	6.03535×10^{-4}	7.10397×10^{-4}
P_{23}, m	0.35615×10^{-3}	8.01613×10^{-4}	1.13436×10^{-3}
P_{24}, m	0.21598×10^{-3}	1.92981×10^{-4}	2.24116×10^{-4}
P_{25}, m	0.38387×10^{-3}	9.95398×10^{-5}	6.51777×10^{-5}
P_{26}, m	0.51054×10^{-3}	1.66902×10^{-3}	2.02733×10^{-3}
P_{27}, m	0.10099×10^{-3}	1.50521×10^{-5}	8.41545×10^{-6}
P_{28}, m	0.03395×10^{-3}	5.63213×10^{-6}	6.74201×10^{-6}
P_{29}, m	0.14256×10^{-3}	2.49441×10^{-5}	1.99461×10^{-5}
P_{30}, m	0.08521×10^{-3}	1.89122×10^{-5}	1.23812×10^{-5}
P_{31}, m	0.08499×10^{-3}	1.70609×10^{-5}	1.11665×10^{-5}
P_{32}, m	0.03564×10^{-3}	6.74265×10^{-6}	8.23473×10^{-6}
P_{33}, m	1.10613×10^{-3}	1.43474×10^{-3}	1.36666×10^{-3}
P_{34}, m	0.21804×10^{-3}	3.92250×10^{-4}	3.60759×10^{-4}
P_{35}, m	0.35230×10^{-3}	7.33627×10^{-4}	9.51966×10^{-4}
P_{36}, m	0.17892×10^{-3}	7.43211×10^{-5}	7.69412×10^{-5}
P_{37}, m^2	0.75741×10^{-3}	1.08926×10^{-3}	9.50979×10^{-4}
P_{38}, m^2	0.49548×10^{-3}	7.93744×10^{-4}	8.90514×10^{-4}
P_{39}, m^2	0.36758×10^{-3}	1.07828×10^{-4}	7.09976×10^{-5}
P_{40}, m^2	0.19251×10^{-3}	5.71175×10^{-5}	3.81569×10^{-5}
P_{41}, *deg.*	17.00	40.46	42.26
P_{42}, *deg.*	2.70	0.29	0.19
P_{43}, *deg.*	12.57	16.59	19.12
P_{44}, *deg.*	2.76	4.92	5.78
P_{45}, *deg.*	6.99	19.84	27.03
P_{46}, *deg.*	2.84	0.44	0.27
P_{47}, *deg.*	16.41	20.00	20.72
P_{48}, *deg.*	5.00	4.87	0.01

* for definition of each design variable refer to Table 4.2

8. CONCLUDING REMARKS

The aerodynamic-structural-control design of a simplified wing and a forward-swept composite wing were studied. In the first example, the focus was on the structural-control interaction in the multidisciplinary wing design. The wing was modeled as a beam with a control surface near the wing tip. The torsional stiffness was the only design property varying along the span. The aerodynamic model was based on the strip theory, and the control model was based on output feed-back control. The simplicity of the wing allowed the use of simple theoretical models to study the effect of active controls and structural stiffness tailoring in cantilevered-wing divergence suppression. With the structural-control interaction being the main focus, two different approaches were taken for the simplified wing design: (1) a sequential approach, (2) an integrated approach. In each approach the wing was designed for minimum weight subject to divergence and control deflection constraints. The results of this study indicated that while the integrated approach produced a better design than the sequential approach, the difference (in this particular example) was minimal.

In the second example, a forward-swept composite wing was designed for a high subsonic transport aircraft. The structural analysis was based on finite-element method. The aerodynamic calculations were based on vortex-lattice method, and the control calculations were based on output feed-back control. The wing was designed for minimum weight subject to structural, aerodynamic/performance and control constraints. The control deflection and efficiency sensitivities were derived and analyzed. These sensitivities involved second order derivatives compared to the aerodynamic and structural sensitivities which involve first order derivatives, and

hence their calculations are computationally more expensive. Even with the efficient evaluation of these derivatives in the design procedure, the computational time for each approximate optimization cycle increased from approximately 1100 (CPU) sec. (for aerodynamic-structural design) to over 2500 (CPU) sec. (for aerodynamic-structural-control design) on an IBM 3090 mainframe. The completion of 60 approximate optimization cycles took approximately 42 (CPU) hrs.

To suppress the aeroelastic divergence of the forward-swept wing, and to reduce the gross weight of the design aircraft, two separate cases were studied: (1) combined application of aeroelastic tailoring and active controls, (2) aeroelastic tailoring alone. The results of this study indicated that, for this particular example, the aeroelastic tailoring was more effective in suppressing the aeroelastic divergence than active controls. It is possible, however, to see a greater influence of active controls on divergence suppression of an isotropic or untailored composite forward-swept wing designs[29-32]. Furthermore, the potential of using active controls as a tool for suppressing an aeroelastic instability can be realized more in the case of aeroelastic flutter as shown also in Refs. 29-32.

Future work should include the incorporation of unsteady transonic aerodynamic load calculation capability so that designs could be considered at higher and more efficient Mach numbers than the one currently used. Also, the rigid-body mode should be included in the analysis which would permit the calculation of body-freedom flutter as well. Finally, more efficient techniques must be developed to reduce the computational cost further.

REFERENCES

1. Holzbaur, S., "Sweptforward Wings," *Interavia*, Vol. 5, No. 7, 1950, pp. 380–382.
2. Jones, L. S., *U.S. Bombers, B-1—B-70*, Aero Publishers, Los Angeles, CA, 1962.
3. Diederich, F. W. and Budiansky, B., "Divergence of Swept Wings," NACA TN 1680, 1948.
4. Bisplinghoff, R. L., Ashley, H. and Halfman, R. L., *Aeroelasticity*, Addison-Wesley Publishing Company, Inc., Cambridge, MA, 1955.
5. Burns, B. R. A., "Forward Sweep: Pros and Cons," *Interavia*, Vol. 40, No. 1, 1985, pp. 39–41.
6. Krone, N. J., Jr., "Divergence Elimination with Advanced Composites," AIAA Aircraft Systems and Technology Meeting, Los Angeles, CA, August 4-7, 1975, AIAA Paper No. 75-1009.
7. Krone, N. J., Jr., "Forward Swept Wing Design," *Proceedings of AIAA Evolution of Aircraft Wing Design Symposium*, Dayton, Ohio, March 18-19, 1980, pp. 147–149.
8. Krone, N. J., Jr., "Forward Swept Wing Flight Demonstrator," AIAA Aircraft Systems and Technology Meeting, Anaheim, CA, August 4-6, 1980, AIAA Paper No. 80-1882.
9. Weisshaar, T. A., "Aeroelastic Stability and Performance Characteristics of Aircraft with Advanced Composite Sweptforward Wing Structures," AFFDL-TR-78-116, September 1978.

10. Weisshaar, T. A., "Divergence of Forward Swept Composite Wings," *Journal of Aircraft*, Vol. 17, No. 6, June 1980, pp. 442–448.

11. Triplett, W. E., "Aeroelastic Tailoring of Forward Swept Wing and Comparisons with Three Equivalent Aft Swept Wings," *Proceedings of AIAA/ASME/ASCE/AHS 21st Structures, Structural Dynamics and Materials Conference*, Seattle, WA, May 12-14, 1980, Part 2, pp. 754–760.

12. Triplett, W. E., "Aeroelastic Tailoring Studies in Fighter Aircraft Design," *Journal of Aircraft*, Vol. 17, No. 7, July 1980, pp. 508–513.

13. Weisshaar, T. A., "Aeroelastic Tailoring of Forward Swept Composite Wings," *Journal of Aircraft*, Vol. 18, No. 8, August 1981, pp. 669–676.

14. Sherrer, V. C., Hertz, T. J. and Shirk, M. H. "Wind Tunnel Demonstration of Aeroelastic Tailoring Applied to Forward Swept Wings," *Journal of Aircraft*, Vol. 18, No. 11, November 1981, pp. 976–983.

15. Ricketts, R. H. and Doggett, R. V. Jr., "Wind-Tunnel Experiments on Divergence of Forward-Swept Wings," NASA TP-1685, 1980.

16. Bland, S. R., "Illustration of Airfoil Shape Effect on Forward-Swept Wing Divergence," *Journal of Aircraft*, Vol. 17, No. 10, October 1980, pp. 761–763.

17. Landsberger, B. J. and Dugundji, J., "Aeroelastic Behavior of Straight and Forward Swept Graphite/Epoxy Wings," *Proceedings of AIAA/ASME/ASCE/AHS 25th Structures, Structural Dynamics and Materials Conference*, Palm Springs, CA, May 17-18, 1984, Part 2, pp. 589–598.

18. Cole, S. R., "Divergence Study of a High-Aspect Ratio, Forward-Swept Wing," *Journal of Aircraft*, Vol. 25, No. 5, May 1988, pp. 478–480.

19. Norton, W. J., Capt., *Design of an Aeroelastic Composite Wing Wind Tunnel Model*, Master of Science Thesis in Aeronautical Engineering, Air Force

Institute of Technology, Wright-Patterson AFB, Dayton, Ohio, U.S.A., May 1987.

20. Miller, G. D., Wykes, J. H. and Brosnan, M. J., "Rigid-Body Structural Mode Coupling on a Forward Swept Wing Aircraft," *Journal of Aircraft*, Vol. 20, No. 8, August 1983, pp. 696–702.
21. Weisshaar, T. A., Zeiler, T. A., Hertz, T. J. and Shirk, M. H., "Flutter of Forward Swept Wings, Analyses and Tests," AIAA Paper No. 82-0646, May 1982.
22. Weisshaar, T. A. and Zeiler, T. A., "Dynamic Stability of Flexible Forward Swept Wing Aircraft," *Journal of Aircraft*, Vol. 20, No. 12, November 1983, pp. 1014–1020.
23. Chen, G. -S. and Dugundji, J., "Experimental Aeroelastic Behavior of Forward Swept Graphite/Epoxy Wings with Rigid Body Freedoms," *Proceedings of AIAA/ASME/ASCE/AHS 27th Structures, Structural Dynamics and Materials Conference*, San Antonio, TX, May 19-21, 1986, Part 1, pp. 462–471.
24. Lottati, I., "Flutter and Divergence Aeroelastic Characteristics for Composite Forward Swept Cantilevered Wing," *Journal of Aircraft*, Vol. 22, No. 11, November 1985, pp. 1001–1007.
25. Niblett, Li. T., "Aeroelastic Divergence of Trimmed Aircraft," *Journal of Aircraft*, Vol. 23, No. 9, September 1986, pp. 727-728.
26. Librescu, L. and Simovich, J., "General Formulation for the Aeroelastic Divergence of Composite Swept-Forward Wing Structures," *Journal of Aircraft*, Vol. 25, No. 4, April 1988, pp. 364–371.
27. Librescu, L. and Thangjitham, S., "Analytical Studies on Static Aeroelastic Behavior of Forward-Swept Composite Wing Structures," *Journal of Aircraft*, Vol. 28, No. 2, February 1991, pp. 151–157.

28. Shirk, M. H., Hertz, T. J. and Weisshaar, T. A., "Aeroelastic Tailoring-Theory, Practice, and Promise," *Journal of Aircraft*, Vol. 23, No. 1, January 1986, pp. 6–18.

29. Griffin, K. E. and Eastep, F. E., "Active Control of Forward-Swept Wings with Divergence and Flutter Aeroelastic Instabilities," *Proceedings of AIAA/ASME/ ASCE/AHS 22nd Structures, Structural Dynamics and Materials Conference*, Atlanta, GA, April 9-10, 1981, Part 2, pp. 602–610.

30. Chipman, R. R. Zislin, A. M. and Waters, C., "Control of Aeroelastic Divergence," *Journal of Aircraft*, Vol. 20, No. 12, December 1983, pp. 1007–1013.

31. Noll, T. E., Eastep, F. E. and Calico, R. A., "Active Suppression of Aeroelastic Instabilities on a Forward Swept Wing," *Proceedings of AIAA/ASME/ASCE/ AHS 24th Structures, Structural Dynamics and Materials Conference*, Lake Tahoe, NV, May 2-4, 1983, Part 2, pp. 577–588.

32. Noll, T. E., Calico, R. A. and Eastep, F. E., "Control of Forward Swept Wing Aeroelastic Instabilities Using Active Feedback Systems," *Proceedings of AIAA Guidance and Control Conference*, Gatlinburg, TN, August 15-17, 1983, pp. 412–422.

33. Löbert, G., "Passive Divergence Control with Free-Floating Wing Tips," *Proceedings of International Conference, Forward Swept Wing Aircraft*, Bristol, U.K., March 24-26, 1982, pp. III.2.1–III.2.3.

34. Dastin, S., Eidinoff, H. L. and Armen, H. Jr., "Some Engineering Aspects of the X-29 Airplane," *Proceedings of 29th National SAMPE Symposium and Exhibition*, Reno, NV, April 3-5, 1984, Vol. 29 pp. 1438–1449.

35. Raha, J., "Grumman's Forward Swept Wing Feasibility Studies and X-29A Technology Demonstrator," 41st Annual Conference of the Society of Allied Weight Engineers, Inc., San Jose, CA, May 17-19, 1982.

36. Schweiger, J., Schneider, G., Sensburg, O. and Löbert, G., "Design of a Forward Swept Wing Fighter Aircraft," *Proceedings of International Conference, Forward Swept Wing Aircraft*, Bristol, U.K., March 24-26, 1982, pp. I.4.1– I.4.13.

37. Roskam, J., "Forward Swept Wings and Commuter Airplanes," *Proceedings of International Conference, Forward Swept Wing Aircraft*, Bristol, U.K., March 24-26, 1982, pp. I.5.1–I.5.11.

38. Howe, D., "A Comparison Between Forward and Aft Swept Wings on V/STOL combat Aircraft," *Proceedings of International Conference, Forward Swept Wing Aircraft*, Bristol, U.K., March 24-26, 1982, pp. I.8.1–I.8.10.

39. Cook, E. L. ad Abla, M., "Weight Comparison of Divergence-Free Tailored Metal and Composite Forward Swept Wings," *Proceedings of International Conference, Forward Swept Wing Aircraft*, Bristol, U.K., March 24-26, 1982, pp. II.4.1–II.4.9.

40. Redeker, G. and Wichmann, G., "Forward Sweep - A Favorable Concept for a Laminar Flow Wing," *Journal of Aircraft*, Vol. 28, No. 2, February 1991, pp. 97–103.

41. Sobieszczanski-Sobieski, J., "Sensitivity of Complex, Internally Coupled Systems," AIAA Paper No. CP-88-2378, also *AIAA Journal*, Vol. 28, No. 1, pp. 153–160, 1990.

42. Sobieszczanski-Sobieski, J., "Sensitivity Analysis and Multidisciplinary Optimization for Aircraft Design: Recent Advances and Results," *Proceedings of the 16th Congress of the International Council of the Aeronautical Sciences*, Jerusalem, Israel, August 1988, pp. 953–964.

43. Barthelemy, J., F., M. and Bergen, D. B., "Shape Sensitivity Analysis of Wing Static Aeroelastic Characteristics," NASA TP 2808, 1988.

44. Sobieszczanski-Sobieski, J. and Haftka R. T., "Interdisciplinary and Multilevel Optimum Design," *Proceedings of NATO ASI Series*, Vol. F27, Springer-Verlag Berlin Heidelberg, 1987, pp. 655–701.

45. Gilbert, M. G., Schmidt, D. K. and Weisshaar, T. A., "Quadratic Synthesis of Integrated Active Controls for an Aeroelastic Forward-Swept-Wing Aircraft," *Proceedings of AIAA Guidance and Control Conference*, San Diego, CA, August 9-11, 1982, pp. 675–684.

46. Zeiler, T. A., *An Approach to Integrated Aeroservoelastic Tailoring for Stability*, Doctor of Philosophy Dissertation in Aeronautical Engineering, Purdue University, West Lafayette, Indiana, U.S.A., May 1985.

47. Dracopoulos, T. N., *Aeroelastic Control of Composite Lifting Surfaces-Integrated Aeroelastic Control Optimization*, Doctor of Philosophy Dissertation in Aerospace Engineering, The Ohio State University, Columbus, Ohio, U.S.A., May 1988.

48. Livne, E., Schmit, L. and Friedmann, P. P., "Exploratory Design Studies Using an Integrated Multidisciplinary Synthesis Capability for Actively Controlled Composite Wings," *Proceedings of AIAA/ASME/ASCE/AHS/ASC 31st Structures, Structural Dynamics and Materials Conference*, Long Beach, CA, April 2-4, 1990, AIAA Paper No. 90-0953.

49. Livne, E., Schmit, L. and Friedmann, P. P., "Further Design Experimentation with an Integrated Multidisciplinary Synthesis Capability for Actively Controlled Composite Wings," Third Air Force/ NASA Symposium on Recent Advances in Multidisciplinary Analysis and Optimization, San Francisco, CA, September 24-26, 1990.

50. Livne, E., Schmit, L. and Friedmann, P. P., "Towards Integrated Multidisciplinary Synthesis of Actively Controlled Fiber Composite Wings," *Journal of Aircraft*, Vol. 27, No. 12, December 1990, pp. 979–992.

51. Livne, E., Friedmann, P. P. and Schmit, L., "Studies in Integrated Aeroservoelastic Optimization of Actively Controlled Composite Wings," *Proceedings of AIAA/ASME/ASCE/AHS/ASC 32nd Structures, Structural Dynamics and Materials Conference*, Baltimore, MD, April 8-10, 1991, Part 1, pp. 447–461.

52. Guruswamy, G. P., "Integrated Approach for Active Coupling of Structures and Fluids," *AIAA Journal*, Vol. 27, No. 6, June 1989, pp. 788–793.

53. Morris, S. J. and Kroo, I., "Aircraft Design Optimization with Multidisciplinary Performance Criteria", *Proceedings of AIAA/ASME/ASCE/AHS/ASC 30th Structures, Structural Dynamics and Materials Conference*, Mobile, AL, April 1989, Part 2, pp. 909–919.

54. Isogai, K., "Direct Search Method to Aeroelastic Tailoring of a Composite Wing Under Multiple Constraints", *Journal of Aircraft*, Vol. 26, No. 12, December 1989, pp. 1076–1080.

55. Oyibo, G. A., "Generic Approach to Determine Optimum Aeroelastic Characteristics for Composite Forward-Swept-Wing Aircraft," *AIAA Journal*, Vol. 22, No. 1, January 1984, pp. 117–123.

56. Sensburg, O., Schmidinger, G. and Füllhas, K., "Integrated Design of Structures," *Journal of Aircraft*, Vol. 26, No. 3, March 1989, pp. 260-270.

57. Grossman, B., Strauch, G. J., Eppard W. M., Gürdal, Z. and Haftka, R. T., "Combined Aerodynamic-Structural Design of a Sailplane Wing," *Journal of Aircraft*, Vol. 25, No. 9, September 1988, pp. 855–860.

58. Haftka, R. T., Grossman, B., Eppard, W. M., Kao, P.J. and Polen, D. M., "Efficient Optimization of Integrated Aerodynamic-Structural Design," *International Journal for Numerical Methods in Engineering*, Vol. 28, 1989, pp. 593–607.

59. Shuart, M. J., Haftka, R. T. and Campbell, R. L., " Optimization Design of Swept-Forward High-Aspect-Ratio Graphite-Epoxy Wings," Recent Advances in Multidisciplinary Analysis and Optimization, (J-F. M. Barthelemy, editor), NASA CP-3031, 1988, pp. 509-527.

60. Grossman, B., Haftka, R. T., Kao, P.J., Polen, D. M., Rais-Rohani, M., Sobieszczanski-Sobieski, J., "Integrated Aerodynamic-Structural Design of a Transport Wing," *Journal of Aircraft*, Vol. 27, No. 12, December 1990, pp. 1050-1056.

61. Polen, D. M., *Integrated Aerodynamic-Structural Design of a Subsonic, Forward-Swept Transport Wing*, Master of Science Thesis in Aerospace Engineering, Virginia Polytechnic Institute and State University, Blacksburg, Virginia, U.S.A., May 1989.

62. Unger, E. R., Rais-Rohani, M., Hutchison, M. G., Haftka, R. T. and Grossman, B., "Multidisciplinary Design of a Subsonic Transport Wing," Third Air Force/NASA Symposium on Recent Advances in Multidisciplinary Analysis and Optimization, San Francisco, CA, September 24-26, 1990.

63. Kao, P. J., *Efficient Methods for Integrated Structural-Aerodynamic Wing Optimum Design*, Doctor of Philosophy Dissertation in Aerospace Engineering, Virginia Polytechnic Institute and State University, Blacksburg, Virginia, U.S.A., March 1989.

64. Dowell, E. H., Curtiss, H. C., Scanlan, R. H. and Sisto, F., *A Modern Course in Aeroelasticity*, Sijthoff & Noordhoff, The Netherlands, 1978.

65. Fung, Y. C., *An Introduction to the Theory of Aeroelasticity*, Dover Publishings, Inc., New York, NY, 1969.

66. Reddy, J. N., *An Introduction to the Finite Element Method*, McGraw-Hill Book Company, New York, NY, 1984.

67. Haftka, R. T. and Kamat, M. P., *Elements of Structural Optimization*, Martinus Nijhoff Publishers, The Netherlands, 1985.

68. Grandhi, R. V., Thareja, R., and Haftka, R. T., "NEWSUMT-A: A General Purpose Program for Constrained Optimization using Constraint Approximations," *ASME Journal of Mechanisms, Transmissions, and Automation in Design*, Vol. 107, pp. 94–99, 1985.

69. Turriziani, R. V., "Continuation of a Study of the Effects of Advanced Technologies on the Sizing and Fuel Efficiency of a 150 Passenger 1220 N.Mi. Airplane," File: 3-92000/5LTR-007, January 1985.

70. Johnson, W. G. Jr., Hill, A. S. and Eichmann, O., "High Reynolds Number Tests of a NASA SC(3)-0712(B) Airfoil in the Langley 0.3-Meter Transonic Cryogenic Tunnel," NASA TM 86371, June 1985.

71. *Federal Aviation Regulation: FAR-25*

72. Haftka, R. T. and Starnes, J. H. Jr., "WIDOWAC: Wing Design Optimization with Aeroelastic Constraints—Program Manual," NASA TM X-3071, 1974.

73. Unger, E. R.,*Computational Aspects of the Integrated Multi-Disciplinary Design of a Transport Wing*, Master of Science Thesis in Aerospace Engineering, Virginia Polytechnic Institute and State University, Blacksburg, Virginia, U.S.A., May 1990.

74. Davis, W. H. Jr., Aidala, P. V., and Mason, W. H., "A Study to Develop Improved Methods for the Design of Transonic Fighter Wings by the Use of Numerical Optimization," NASA Contractor Report 3995, August 1986.

75. *Janes All the World's Aircraft*, Jane's Information Group Limited, U.K.,1989-90.

VITA

The author was born in Tehran, Iran on March 8, 1960. He completed his elementary and secondary education in Tehran, and received his High School Diploma from Nafisi Institute of Technology (Technicom Nafisi) in June 1977.

In pursuit of higher education he came to the United States in January 1979, and entered Mississippi State University the following year. He received his B.S. in Aerospace Engineering in 1983 followed by M.S. in 1985. In 1984 he joined the Faculty of the Aerospace Engineering Department at Mississippi State University as an Instructor. In Fall of 1987, he was accepted to the PhD program in Aerospace Engineering at Virginia Polytechnic Institute and State University.

Upon graduation, the author intends to rejoin the Faculty of Mississippi State University as an Assistant Professor in the Aerospace Engineering and Engineering Mechanics Department.

Masoud Rais–Rohani